UNIVERSITY OF CALIFORNIA
RIVERSIDE

Controlling Magnetism at the Nanoscale

A Dissertation submitted in partial satisfaction
of the requirements for the degree of

Doctor of Philosophy

in

Physics

by

Jared Jue Wong

December 2012

Dissertation Committee:
Dr. Roland Kawakami, Chairperson
Dr. Harry Tom
Dr. Vivek Aji

The Dissertation of Jared Jue Wong is approved:

_____

_____

_____

Chairperson

University of California, Riverside

Acknowledgments

First and foremost, I would like to express my gratitude to all the people who have guided or helped me during my Ph.D. career and for making it this work possible. First of all, I would like to thank my advisor Prof. Roland K. Kawakami for his guidance as a mentor and patience and understanding. It was an exciting and a privilege opportunity to work in his research group. I thank him for giving me the opportunity to work on a wide variety of projects involved in his research in the nano-magnetism field. I have learned many things and gain much experience under his guidance and without a doubt, will be essential in my future endeavors.

I would also like to thank my committee members, Prof. Harry Tom and Prof. Vivek Aji. I express my thanks for the guidance and discussion I have had with them throughout the years. Prof. Harry Tom has been like a second advisor for me and has giving me great advise over the years, either through collaborative work or through random discussions. Prof. Vivek Aji has helped me over the years and I thank him for the discussions we have had over projects.

I would like to especially thank my lab mates, past and present, for all their help over the years. I thank Richard Chiang, Kyle Pi, Wei-Hua Wang and Yan Li for helping during my beginning years within the research group. They taught me many of the skill I have today and they will forever have my gratitude. I would like to also thank Kathy McCreary, Wei Han and Adrian Swartz. They were part of my generation of student within the group and had spent

countless hours working together. I have really enjoyed the time spent working with them over the years and thank them for all the help and discussion we have had over the years here. I especially thank Adrian for the countless times he has helped me and for the collaborative work we have done together. I would also like to thank Luciana Ramirez, Igor Pinchuk, Steven Tjung and Renjing Zheng, all of whom have worked with my on various projects. I also would like to thank the rest of the research group Hua Wen, Patrick Odenthal, Jen-Ru Chen, George Christensen, Walid Amamou, Andrew Hoff, Alexander Speirs and Desalegne Teweldebrhan.

I would like to thank many of my friends, faculty and staff in the Physics department here at UCR for their support over the years. They have made my time here very enjoyable and an experience I will never forget.

Last, but not least, I would like to thank my parents and family for their love and support of the years. Without them, none of this would be possible and words cannot express the gratitude I have. I thank you from the bottom of my heart and I love all of you.

ABSTRACT OF THE DISSERTATION

Controlling Magnetism at the Nanoscale

by

Jared Jue Wong

Doctor of Philosophy, Graduate Program in Physics
University of California, Riverside, December 2012
Dr. Roland Kawakami, Chairperson

In this thesis, we look at controlling the magnetic properties at the nano-scale in single crystal thin film through structural modifications and external static electric fields (i.e. magnetoelectric effects). First, we study the biquadratic exchange coupling in Fe/MgO/Fe system and find that interface oxidation at the Fe/MgO interface leads an intermediate 90° alignment between the to ferromagnetic layers. Though temperature dependence measurements, we conclude that the ”loose spins” [1] model can account for the phenomena seen. Next, we look at the interlayer exchange coupling in Fe/MgO/Fe and Fe/MgO/Co systems with magnetic Fe nanoclusters embedded in the MgO spacer. We find that by varying the position of the Fe nanoclusters within the MgO barrier, the bilinear coupling (J_1) exhibits strong variations in magnitude and can even switch between antiferromagnetic and ferromagnetic. It is also shown that the coupling between Fe nanoclusters and Co is greatly enhanced when

compared to the coupling between Fe and Co thin films, show an interesting nano-scaling related to coupling between films and nanoclusters.

Next, we investigate the initial growth modes and the role of interfacial electrostatic interactions of EuO epitaxy on MgO(001) by reactive molecular beam epitaxy. Here, we employ an TiO_2 electrostatic template on MgO to produce high quality epitaxial growth of EuO on MgO(001) and find the initial growth sequence is drastically different with the TiO_2 interface than on the bare MgO. The TiO_2 layer allows for substrate assisted oxidation to form EuO, leading to ultrathin ferromagnetic EuO films normally not observed with direct growth of EuO on MgO.

The second half of the thesis focuses on electric field induce changes to magnetic properties in ultrathin Fe films and in the correlated system Fe_3O_4. First, we looked at tuning the perpendicular magnetic anisotropy (PMA) in the MgO/Fe/Ag system on MgO (001) and find that the application of large gate voltages, the magnetic anisotropy can be tuned to prefer a more in-plane or out-of-plane alignment.

Finally, we investigate the electrical gating effects inside the highly correlated system of Fe_3O_4. One of the most intriguing and well-known properties of magnetite is a phase transition at a critical temperature near 120K known as the Verwey Transition, where an abrupt change in the crystallographic and electronic structure are observed and accompanied by changes in electrical, magnetic, thermodynamic and mechanical properties [2]. Here, we demonstrated the electric field control of the Verwey transition and show electric fields stabilizes the charge-ordered insulating state causing the Verwey transition temperature to

increase. By manipulating a correlated phase transition, we realize a large and novel magnetoelectric effect.

Contents

List of Tables

List of Figures

Chapter 1

Introduction

1.1 Abstract

In this section, I first briefly introduce some of the history surrounding magnetism at the nanoscale. Specifically, I'll be talking briefly about interlayer exchange coupling between to magnetic layers across a nonmagnetic spacer. Then I'll be briefly talk about the recent work of manipulating magnetism with external stimuli, such as electric fields. Finally, Ill outline the motivation for the work in this thesis.

1.2 Interlayer Exchange coupling

Interlayer exchange coupling (IEC) is when magnetic films are separated by a non-magnetic spacer layer, the magnetizations of the two layers couple by an exchange interaction through the electrons within the spacer layer. The coupling exhibits a dependence on the spacer thick-

ness and can oscillate in sign as a function of thickness, such as in ferromagnetic (FM) or antiferromagnetic (AF) alignment between the two magnetic layers [3]. IEC is closely related to the well-known Ruderman-Kittel-Kasuya-Yoshida (RKKY) interaction between magnetic impurities through a non-magnetic medium [4–6]. IEC was first observed in magnetic/non-magnetic transition metal multilayer systems and in rare-earth metal multilayer systems [7–9]. After the discovery of IEC, electric measurements were carried out across these multilayers systems, such a Fe/Cr multilayers, and found a larger changes in resistance was observed depending on magnetization alignments. This discovery is known as giant magnetoresistance (GMR) and has since been implemented into technology and application use today [10–13]. There has been much research on IEC over the years, including several review, which has lead to a great understanding of IEC in transition metal and other multilayer systems [3, 12, 14, 15]. In this thesis, we will be taking a look at both bilinear and biquadratic coupling.

1.2.1 Bilinear IEC

In short, bilinear coupling refers to IEC that causes the magnetizations of the magnetic materials to align colinearly, as in parallel (FM coupling) or antiparallel (AF coupling) in zero field. Figure 1.1 show a diagram of this interaction and the dependence of the coupling strength , J_1, as a function of spacer thickness, t [16]. At thin spacer thicknesses, typically 1 nm and below, we see a large positive value for J_1, indicating a large FM coupling between the two magnetic layers. As the thickness is increased, J_1 switches signs to a negative value showing that the layers are AF aligned. As the thickness is increased, Figure 1.1 shows

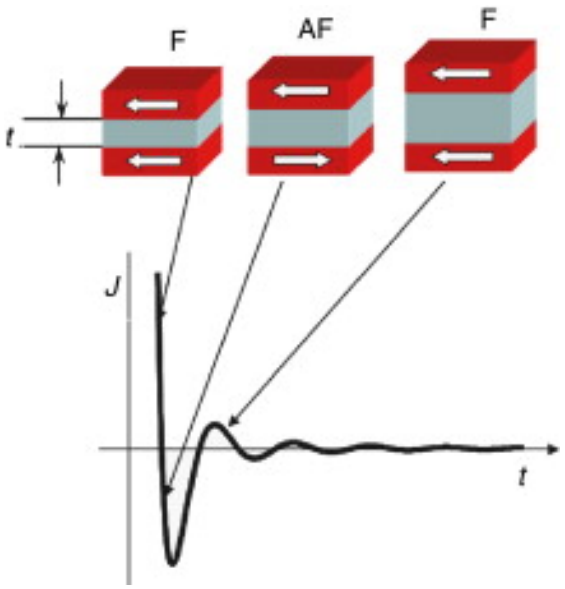

Figure 1.1: A schematic of the magnetization alignments for the oscillatory interlayer exchange coupling between two ferromagnetic layers mediated by a non-magnetic spacer layer from Ref [16]. The graph shows a schematic for the coupling strength, J, dependence on the non-magnetic spacer thickness, t.

that J_1 oscillates between FM and AF alignments with decreasing overall strength. The exact oscillation period depends on the spanning vector across the Fermi surface of the metal spacer layer and the amplitude is a property of the nesting features encountered at the Fermi surface [3, 16, 17].

First consider a single interface between a magnetic and nonmagnetic layer, it sets up an oscillatory polarization in the non-magnetic spacer and is essentially a single-particle effect. As electrons are incoming to the interface, they scatter and an interference between incoming and scattered electron waves gives rise to a standing wave with oscillatory probability densities for each electron. Now, with a magnetic material at the interface, the spin-up and spin-down electrons will scatter differently, thus filling states below the Fermi energy gives an oscillatory spin density. Since different waves are characterized by vectors for all

the states and each of these states then contribute to the oscillations with different periods. However, only the oscillations at the fermi energy don't cancel out, leaving an oscillation, which characterized by the Fermi surface. Bringing in the second magnetic layer creating a second FM/NM interface, this interface couples with the spin density that was set-up by the first interface. Now, due to the spin density oscillating as a function of the spacer-layer thickness, the coupling oscillates as well [3, 16, 17].

There are different ways of determining the bilinear coupling between two FM layers. In studies within this thesis, we use an minor hysteresis loop analysis for determining J_1. Figure 1.2 show schematic of how J_1 is determined from the minor hysteresis loop analysis. There are two magnetic layers that are coupling together across a spacer. One layer is the "hard" layer, having a large coercive field (H_C) and another layer has a much smaller H_C, which is the free layer. When a large magnetic field is applied, both layers are saturated which are indicated by the arrows in figure Figure 1.2. The blue arrows denote the magnetization of a "hard" magnetic layer and the red arrows are the magnetization of a "free" magnetic layer. As the applied H field swept from negative saturation to positive saturation, we see to distinct jump in the major hysteresis loop (Fig. 1.2 - black curve) corresponding to the magnetic switch of each layer. For the minor loop analysis, the applied H field swept from the negative saturation to just switching the "free" layer and back, as shown by the red curve.

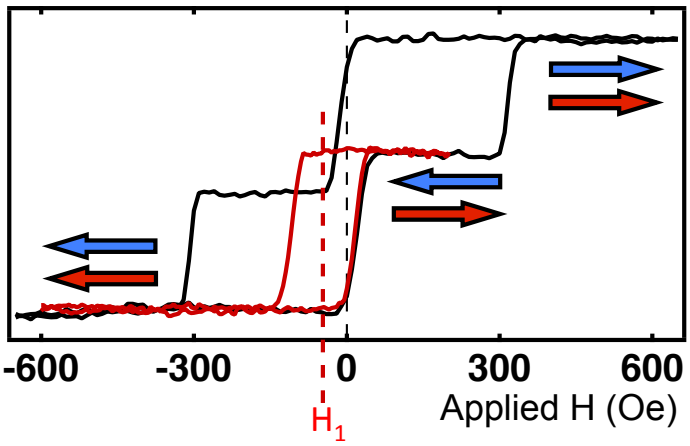

Figure 1.2: A schematic of the magnetization alignments between to couple layers. The Blue arrow indicated the magnetization of a "hard" magnetic layer and the red arrow is the magnetization of a "free" magnetic layer. The red curve is the minor hysteresis loop and H_1 denotes the minor loop shift.

The global area energy density equation with the easy magnetic axis parallel with the applied field is given by

$$E(\theta, H) = (-HMt + J_1)\cos(\theta) + J_2\cos^2(\theta) + Kt\cos^2(\theta)\sin^2(\theta) \tag{1.1}$$

where H is the applied magnetic field, M is the saturation magnetization, t is the "free" layer thickness, J_1 is the bilinear coupling constant, J_2 is the biquadratic coupling constant, K is the anisotropy constant and θ is the angle between the magnetization and applied field for the "free" layer. Because J_1 enters equation 1.1 in the same coefficient as H, the effect of J_1 is to shift the minor hysteresis loop by $H_1 = J_1/Mt$. Thus, by measuring the H_1, as shown in figure 1.2, combine with the known magnetization (emu/cc) and free layer thickness, one

can determine the strength and sign of J_1 (erg/cm^2),

$$J_1 = H_1 M_F t_F \tag{1.2}$$

with negative H_1 values denoting AF coupling and positive values denote FM coupling.

One of the usefulness of IEC is that multilayer can be design into an AF system, which are both of fundamental and practical importance. This systems are presently used in spintronic devices for pinning of ferromagnetic layers, thus producing an hard magnetic layer used for magnetoresistance devices and high density storage disks [18].

1.2.2 Biquadradic IEC

The biquadratic coupling which is almost always present in addition to the bilinear coupling. The biquadratic coupling is believed to arise from extrinsic effects [19], like interface roughness, and the comparison between theory and experiment is much more ambiguous. A recent review [20] describes what is known. Particular forms of biquadratic coupling are associated with antiferromagnetism in the spacer layer, Cr and Mn being two examples. These effects are described elsewhere in this volume [21]. and will not be considered here.

A variety of possible mechanisms for such coupling have been proposed, including the presence of paramagnetic loose spins in the spacer layer [1], and interfacial roughness, causing fluctuations in the sign of indirect exchange coupling [22]. If in some areas the coupling constant is positive (ferromagnetic) and in other areas it is negative (antiferromagnetic), then

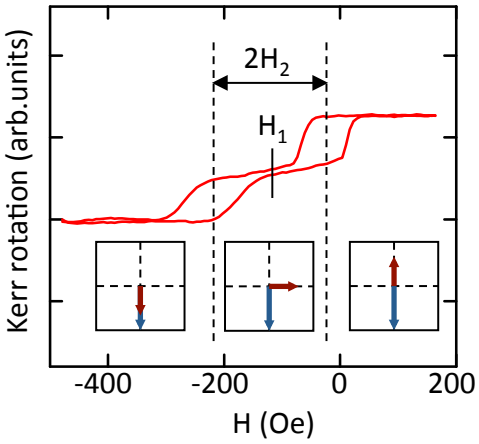

Figure 1.3: Illustration of the shifting (H_1) and splitting ($2H_2$) of a minor hysteresis loop. The red arrow represent the magnetization of the free layer and the blue arrow is the magnetization of the hard layer.

there will be a competition between these two effects. If the inhomogeneities are on a short enough lateral length scale for the intralayer exchange stiffness to be effective, the layers are then unable to break into ferromagnetically and antiferromagnetically coupled domains. It is then possible for an orthogonal configuration of the layer moments to be the state of lowest energy. The layers are compelled to maintain a uniform magnetization throughout their extent, and as a result the mixed-sign coupling causes the moments in adjacent layers to be frustrated. The resultant arrangement for the moments is neither parallel nor antiparallel, but to lie at 90° to each other [23]. More details about biquadratic coupling will be discussed in the later chapters and ref. [24].

Lastly, I will mention quickly on how we determine the biquadratic coupling strength in this thesis. Look back at equation 1.1, we see there is a higher energy term J_2, which is the biquadratic coupling constant. Figure 1.3 show a representative minor hysteresis loop, similar to the one before, except there are two noticeable switches. H_1 shows a negative

overall shift in the minor loop due to AF bilinear coupling and H_2 shows the splitting from the biquadratic coupling. First, both layer are saturated in the negative field direction. As the field is increased to positive applied fields, the magnetization of the free layer switched twice with the first corresponding to the intermediate 90° alignment between the hard (blue arrow) and free (red arrow) layers. As the field is increased, the free layer switches again to a AF alignment with the hard layer. The total splitting in the hysteresis loop is measured as shown in figure 1.3 yielding $2H_2$. The biquadratic coupling can be determined from

$$J_2 \approx H_2 M_F t_F \tag{1.3}$$

The full derivation of this equation is shown in a later chapter and in ref. [24].

1.3 Manipulation of Magnetism - External influences

A frontier of research that has been gaining momentum over the years is research in multifunctional materials in nanoscale systems. Multifunctional systems are made from various combinations of materials like ferromagnetic, ferroelectric, elemental materials, rare-earths, transition metals, oxides, and/or semiconductors making for systems with complicated structures and very interesting properties. What is interesting is that by combining some of these materials, systems can be made that exhibit both ferromagnetic properties and ferroelectric properties (high k-dielectric, piezoelectric and hysteretic electric polarization). With the combination of ferroelectric/ferromagnetic properties, magnetic properties can be controlled

with magnetic and/or electric fields and electrical properties can be controlled with electrical and/or magnetic fields. The single-phase material Cr_2O_3, an AF oxide, is one of the well known materials that shows a magnetoelectric (ME) effect. In general, ME effect can be thought of as the coupling between magnetic and electric fields inside a material. The first observation of the ME effect [25, 26] triggered a lot of excitement because of the obvious potential correlating magnetic and electric properties together inside a material for technical applications and recently has had a resurgence with the introduction of composite multilayer systems. This opens up a whole new avenue of research scientifically and technologically that could lead to the next generation of data storage and processing with lower energy consumption, higher speed, and higher ultimate density. A great review can be found in ref. [27]. The ME effect is the phenomenon of inducing magnetic (electric) polarization by applying an external electric (magnetic) field can be expressed in the following form,

$$P_i = \sum \alpha_{ij} H_j + \sum \beta_{ijk} H_j H_k + ... \tag{1.4}$$

$$M_i = \sum \alpha_{ij} E_j + \sum \beta_{ijk} E_j E_k + ... \tag{1.5}$$

where P is the electric polarization, M the magnetization, E and H the electric and magnetic field, and α and β are the linear and nonlinear ME susceptibilities (coefficients). A table for the linear ME coefficient of different systems is presented in table 8.1.

Recently, a big push has been to explore ways to utilize the ME effect for voltage-driven spintronic devices [28]. In order to achieve this, many areas have been studied and sug-

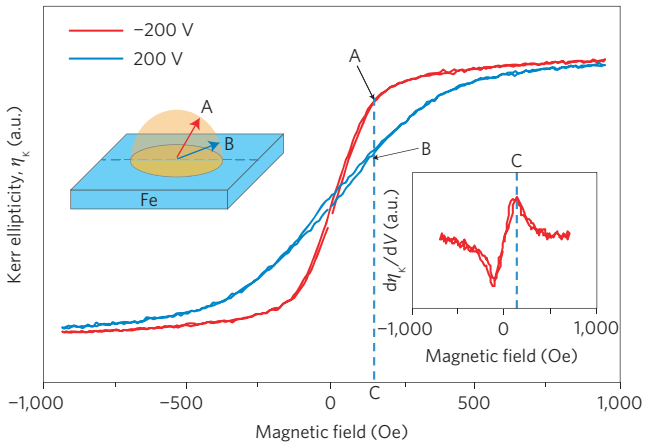

Figure 1.4: MOKE ellipticity for Fe for different applied voltages as a function of H field adapted from Ref. [28]. The thickness of the Fe film was 0.48 nm. A significant change in the hysteresis curve indicated a large change in perpendicular anisotropy following application of the bias voltage. The right inset shows the voltage modulation response of the Kerr ellipticity, $d\nu_K/dV$. The left inset illustrates the magnetization direction at points A and B in the hysteresis curves.

gested, including; voltage control of magnetic anisotropy [28, 29], magnetoelectric switching of magnetic exchange bias in FM/AF systems and anisotropy [30–33], multiferroic properties and hybrid system with FM/piezoelectric materials [34, 35], voltage control of ferromagnetism in ferromagnetic semiconductors [36, 37] and finally, looking at magentoelectric effects at various interfaces [38, 39]. In the work by T. Maruyama *et. al.* [28], They showed that the anisotropy of a ultrathin Fe layer in an MgO/Fe/Au system can be tuned heavily through an application of an external static electric field. The application of negative voltage produced an anisotropy preferring an out-of-plane magnetization, while a positive voltage cause the anisotropy to lay more in-plane (Fig. 1.4). X. He *et. al.* [32] explored the tuning of exchange bias in (Pt/Co)/Cr_2O_3 system and showed reversible, isothermal switching of

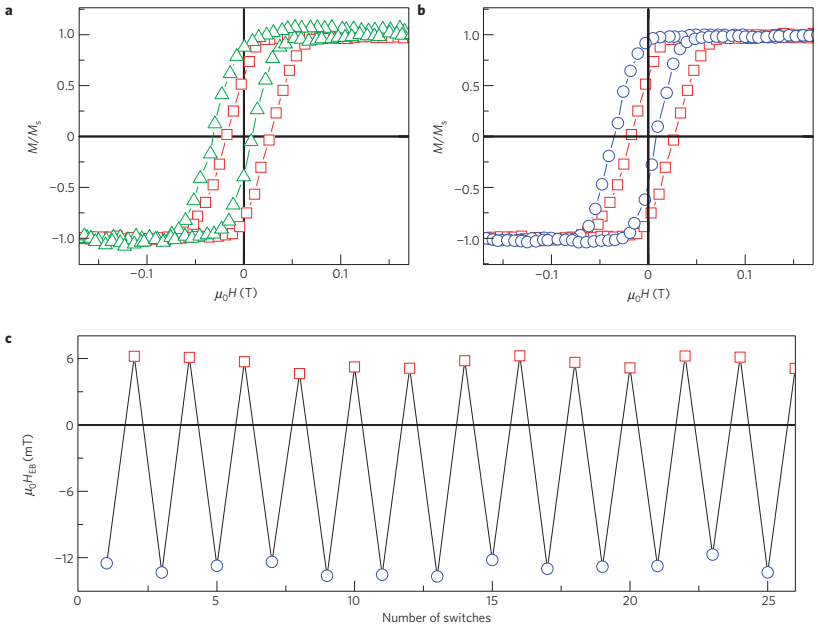

Figure 1.5: Taken from Ref. [32]. a) Exchange-biased hysteresis loops of Cr_2O_3 (0001)/Pd 0.5 nm/(Co 0.6 nm/Pd 1.0 nm)$_3$ at T=RT taken after an magnetoelectric annealing of $E = 0.1\text{kV mm}^{-1} and \mu_\circ H = 77.8\text{mT}$. Red squares show the virgin curve with a positive exchange-bias field of H_{EB} = +6mT. Isothermal-field exposure in $E = -2.6\text{kV mm}^{-1} and \mu_\circ H = +154\text{mT}$ gives rise to a loop with a negative exchange-bias H_{EB} = -13mT (green triangles). b) Shows the effect (blue curve) when exposed to $E = +2.6\text{kV mm}^{-1} and \mu_\circ H = -154\text{mT}$, giving rise to the same H_{EB} = -13mT. c) shows the repeatability of switch H_{EB} using $E = \pm 2.6\text{kV mm}^{-1} and \mu_\circ H = -154\text{mT}$, where $-H_{EB}$ is produced from positive E and H_{EB} is produced from negative E.

the exchange-bias between positive and negative values by reversing the electric field while maintaining a small set magnetic field.

1.4 Conclusion

We can see that there are many ways of controlling magnetism and tuning its properties. In first part of this thesis, we look at controlling the magnetic properties at the nano-scale in single crystal thin film through structural modifications inside interlayer exchange cou-

pling systems involving MgO. MgO is used as the non-magnetic space and is insulating, thus having exchange coupling is odd in itself. We first explore the interfacial modifications and see how it effects the IEC across MgO, giving us some insight on the origins of this phenomena. Next, we look at systematically modifying the MgO barrier itself with embedded Fe nanoclusters. After the IEC studies, we investigate the initial growth modes and the role of interfacial electrostatic interactions of EuO epitaxy on MgO(001) by reactive molecular beam epitaxy. The TiO_2 layer allows for substrate assisted oxidation to form EuO, leading to ultrathin ferromagnetic EuO films normally not observed with direct growth of EuO on MgO.

The second half of the thesis focuses on electric field induce changes to magnetic properties in ultrathin Fe films and in the correlated system Fe_3O_4. First, we looked at tuning the perpendicular magnetic anisotropy (PMA) in the MgO/Fe/Ag system on MgO (001) and explore the tuning of anisotropy with large gate voltage. Finally, we investigate the electrical gating effects inside the highly correlated system of Fe_3O_4. One of the most intriguing and well-known properties of magnetite is a phase transition at a critical temperature near 120K known as the Verwey Transition, where an abrupt change in the crystallographic and electronic structure are observed and accompanied by changes in electrical, magnetic, thermodynamic and mechanical properties [2]. Here, we demonstrated the electric field control of the Verwey transition and show electric fields stabilizes the charge-ordered insulating state causing the Verwey transition temperature to increase. Additionally, we show that by manipulating a correlated phase transition, we realize a large and novel magnetoelectric effect.

References

[1] J. Slonczewski, Journal of applied physics **73**, 5957 (1993).

[2] F. Walz, J. Phys.: Condens. Matter **14**, R285 (2002).

[3] M. Stiles, J. Magn. Magn. Mater. **200**, 322 (1999).

[4] M. A. Ruderman and C. Kittel, Phys. Rev. **96**, 99 (1954).

[5] T. Kasuya, Prog. Theor. Phys. **16**, 4558 (1956).

[6] K. Yosida, Phys. Rev. **106**, 893 (1957).

[7] P. Grünberg, R. Schreiber, Y. Pang, M. B. Brodsky, and H. Sowers, Phys. Rev. Lett. **57**, 2442 (1986).

[8] C. F. Majkrzak, J. W. Cable, J. Kwo, M. Hong, D. B. McWhan, Y. Yafet, J. V. Waszczak, and C. Vettier, Phys. Rev. Lett. **56**, 2700 (1986).

[9] M. B. Salamon, S. Sinha, J. J. Rhyne, J. E. Cunningham, R. W. Erwin, J. Borchers, and C. P. Flynn, Phys. Rev. Lett. **56**, 259 (1986).

[10] M. N. Baibich, J. M. Broto, A. Fert, F. N. Van Dau, F. Petroff, P. Etienne, G. Creuzet, A. Friederich, and J. Chazelas, Phys. Rev. Lett. **61**, 2472 (1988).

[11] G. Binasch, P. Grünberg, F. Saurenbach, and W. Zinn, Phys. Rev. B **39**, 4828 (1989).

[12] A. Fert, P. Grünberg, A. Barthelemy, F. Petroff, and W. Zinn, J. Magn. Magn. Mater. **140**, 1 (1995).

[13] S. S. P. Parkin, N. More, and K. P. Roche, Phys. Rev. Lett. **64**, 2304 (1990).

[14] B. A. Jones, IBM Journal of Research and Development **42**, 25 (1998).

[15] B Heinrich, Springer Tracts in Modern Physics **227**, 185 (2007).

[16] H. Zabel, Superlattices and Microstructures **46**, 541 (2009).

[17] P. Bruno, Phys. Rev. B **49**, 13231 (1994).

[18] E. Fullerton, D. Margulies, M. Schabes, M. Carey, B. Gurney, A. Moser, M. Best, G. Zeltzer, K. Rubin, H. Rosen, et al., Applied Physics Letters **77**, 3806 (2000).

[19] J. Slonczewski, J. Magn. Magn. Mater. **150**, 13 (1995).

[20] S. Demokritov, Journal of Physics D: Applied Physics **31**, 925 (1998).

[21] D. Pierce, J. Unguris, R. Celotta, and M. Stiles, J. Magn. Magn. Mater. **200**, 290 (1999).

[22] J. C. Slonczewski, Phys. Rev. Lett. **67**, 3172 (1991).

[23] C. Marrows and B. Hickey, Physical Review B **59**, 463 (1999).

[24] Y. F. Chiang, J. J. I. Wong, X. Tan, Y. Li, K. Pi, W. H. Wang, H. W. K. Tom, and R. K. Kawakami, Phys. Rev. B **79**, 184410.

[25] I. Dzyaloshinskii, Sov. Phys. JETP **10**, 628 (1960).

[26] D. N. Astrov, Sov. Phys. JETP **11**, 708 (1960).

[27] M. Fiebig, J. Phys. D: Appl. Phys. **38**, R123 (2005).

[28] T. Maruyama, Y. Shiota, T. Nozaki, K. Ohta, N. Toda, M. Mizuguchi, A. Tulapurkar, T. Shinjo, M. Shiraishi, S. Mizukami, et al., Nature Nanotechnology **4**, 158 (2009).

[29] M. Weisheit, S. FŁhler, A. Marty, Y. Souche, C. Poinsignon, and D. Givord, Science **315**, 349 (2007).

[30] P. Borisov, A. Hochstrat, X. Chen, W. Kleemann, and C. Binek, Phys. Rev. Lett. **94**, 117203 (2005).

[31] X. Chen, A. Hochstrat, P. Borisov, and W. Kleemann, Applied physics letters **89**, 202508 (2006).

[32] X. He, Y. Wang, N. Wu, A. N. Caruso, E. Vescovo, K. D. Belashchenko, P. A. Dowben, and C. Binek, Nature Mater **9**, 579 (2010).

[33] Y. Chu, L. Martin, M. Holcomb, M. Gajek, S. Han, Q. He, N. Balke, C. Yang, D. Lee, W. Hu, et al., Nature materials **7**, 478 (2008).

[34] W. Eerenstein, N. Mathur, and J. Scott, Nature **442**, 759 (2006).

[35] V. Novosad, Y. Otani, A. Ohsawa, S. Kim, K. Fukamichi, J. Koike, K. Maruyama, O. Kitakami, and Y. Shimada, Journal of Applied Physics **87**, 6400 (2000).

[36] D. Chiba, M. Yamanouchi, F. Matsukura, and H. Ohno, Science **301**, 943 (2003).

[37] I. Stolichnov, S. Riester, H. Trodahl, N. Setter, A. Rushforth, K. Edmonds, R. Campion, C. Foxon, B. Gallagher, and T. Jungwirth, Nature materials **7**, 464 (2008).

[38] C.-G. Duan, S. S. Jaswal, and E. Y. Tsymbal, Phys. Rev. Lett. **97**, 047201 (2006).

[39] J. Rondinelli, M. Stengel, and N. Spaldin, Nature nanotechnology **3**, 46 (2007).

Chapter 2

Experimental Techniques

2.1 Introduction

One of the key elements with making, studying and understanding these materials at the nanoscale is having high materials quality and a precise control over the materials stoichiometry. Therefore, we utilize molecular beam epitaxy (MBE) to atomically control and engineer the materials in study. Being able to precisely control the composition, quality, and structure of our materials, we are able to explore phenomena at the nanoscale that normally would not be present. It not only important to grow high quality materials, but it is equally important to full characterize the properties of the material that we are studying. Typically, we use reflection high energy electron diffraction (RHEED) to characterize the growth sequence and structural quality of the material during the MBE growth. Magneto-optic Kerr effect (MOKE) is used to investigate the magnetic properties and we also use various elec-

trical measurements (2-probe IV, 4-probe and Van Der Pauw) to determine the electronic properties.

2.2 Molecular Beam Epitaxy

In order to grow high-quality, single-crystal materials, we use Molecular beam epitaxy (MBE). MBE is a materials synthesis technique that allows for excellent control over atomic scale growth. This is done within a ultra high vacuum (UHV) system with typical base pressures of 1×10^{-10} torr. The most important aspect of MBE is the slow deposition rate, typically $\sim$1-2 Å/minute, allowing for thin films to grow epitaxially. An analogy used by us is that it can be thought of as spray painting a material onto a substrate, atom by atom and therefore used to create high quality crystalline films that are easily controlled. Epitaxy is concerned with achieving the deposition of highly-ordered crystalline layers relative to a crystalline substrate. Therefore, crystal structure considerations of the materials being grown need to taken into consideration for epitaxial growth. A table of materials is show in table 2.1. In Chapter 5 will talk about this and that other properties, like ion-sizes, play an very important role in epitaxial growth. Because of the slow deposition rate, UHV is required in order to achieve the same low impurity levels as other deposition methods such as sputtering or electron beam (e-beam) deposition. Figure 2.1 shows a picture of our MBE chamber.

In solid-source MBE, elemental materials such as Co, Fe, or Eu, in ultra-pure form, are heated in separate thermal effusion cells until the elements begin to slowly sublime. The term

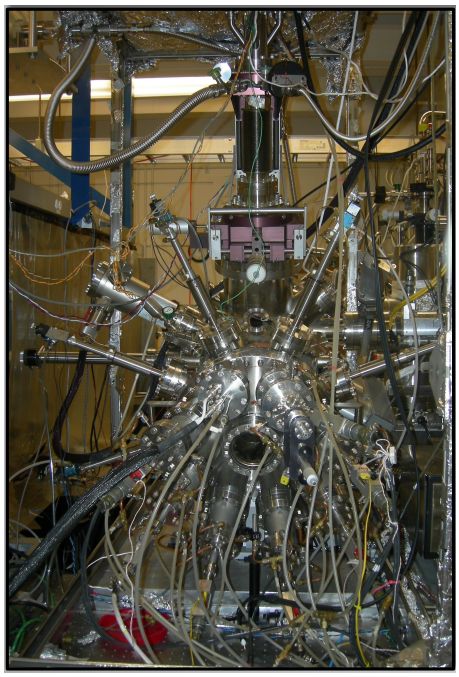

Figure 2.1: Picture of the MBE chamber in the Kawakami Group's Lab. Elemental sources include Fe, Co, Ti, MgO, Eu, Al, Pd, and Cr.

"beam" means that evaporated atoms do not interact with each other or vacuum chamber gases until they reach the wafer, due to the long mean free paths of the atoms. During typical operation during a growth, reflection high energy electron diffraction (RHEED) is often used for monitoring the growth of the crystal layers. More about this in the next section. Shutters are used to block the flux of a material exiting from an evaporation cell, allowing for precise control of the thickness of each layer even down to a single layer of atoms. Such control has allowed the development of structures where the electrons can be confined in space, giving quantum wells or even quantum dots. Such layers are now a critical part of many modern semiconductor devices, including semiconductor lasers and light-emitting diodes.[ref] MBE can also be used for the deposition of some types of organic semiconductors. In this case,

molecules, rather than atoms, are evaporated and deposited onto the wafer. Other variations include gas-source MBE, which resembles chemical vapor deposition.

Table 2.1: Example elements, Lattice constants, and Structures

Element	**Lattice constants(Å)**	**Structure**
Fe	a = 2.86	Body-Centered Cubic (BCC)
Co	a = 2.507, b = 2.507, c = 4.0695	hexagonal close-packed (HCP)
Ni	a = 3.520	Face-Centered Cubic (FCC)
Mg	a = 3.2094, b = 3.2094, c = 5.2108	hexagonal close-packed (HCP)
Pd	a = 3.890	Face-Centered Cubic (FCC)
Cr	a = 2.91	Body-Centered Cubic (BCC)
Eu	a = 4.610	Body-Centered Cubic (BCC)
Al	a = 4.050	Face-Centered Cubic (BCC)
MgO	a = 4.212	Halite (cubic), Rock-salt
EuO	a = 5.14	Halite (cubic), Rock-salt
Cr_2O_3	a = 4.958, b = 4.958, c = 13.594	C.P. Corundum
Fe_3O_4	a = 8.397	Inverse spinal
$BaTiO_3$	a = 3.992, c = 4.036	Perovskite

A typical MBE system usually is comprised of three separate, but connected chambers. First is the main MBE chamber, where the growths take place. The Second chamber is the buffer chamber and the last is the load-lock chamber. The load lock is the chamber that samples are loaded into at atmospheric pressure ($\sim$ 700 torr) and then pumped down to UHV. The load lock is considered "dirty" in the sense that the residual gases and water vapor remains in the chamber (stuck on the chamber walls, etc.) even when pumped below 1×10^{-6} torr. Samples are then transferred into the buffer chamber once the load lock is pumped down. The buffer chamber is a UHV chamber that acts as a buffer zone between the load-lock and the main chamber. By having this buffer chamber, the main growth chamber is never

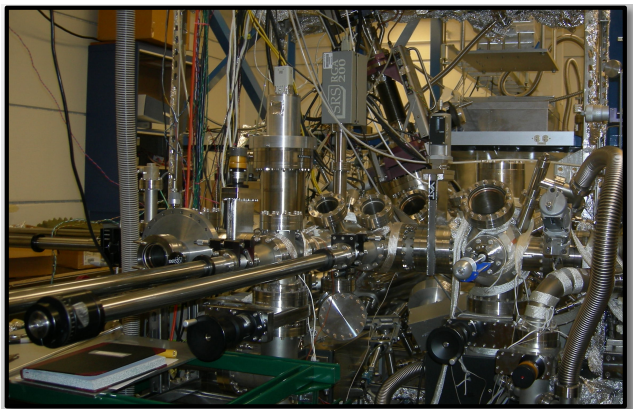

Figure 2.2: Picture of the UHV buffer chamber with LEED, Auger and RGA measurement capabilities.

opened directly to the load-lock and never "see" it. In the buffer chamber, typical pressure of operations for us is $\sim 1 \times 10^{-9}$ torr. Figure 2.2 show a picture of the buffer chamber used in the research group. The buffer chamber pressure is well in the UHV range (typically below $< 1 \times 10^{-8}$) and for our system, we have other measurement capabilities such as low energy electron diffraction (LEED), Auger spectroscopy, and residual gas analysis (RGA). Once the samples are in the buffer chamber and the load lock is closed off, the sample are then finally loaded into the main MBE growth chamber.

Our main MBE growth chamber consist of many different components; the growth evaporators, gas sources (such as pure O_2), mechanical shutters to block the material flux, substrate mount capable of manipulating the sample position (in X, Y, Z, θ directions), substrate heating and cooling, a linear motion wedge shutter, RHEED and a cryo panel. All things are used in various ways to control the growth. Before getting into the details of some of the growths, Let me briefly explain RHEED.

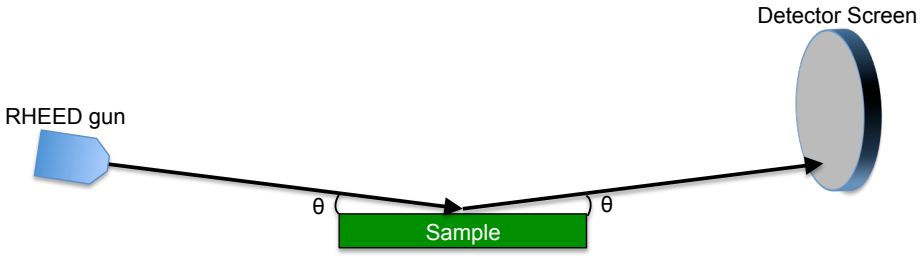

Figure 2.3: Schematic of RHEED measurement setup in a MBE chamber showing the RHEED gun (left), sample (center) and detector (right). The arrows represent the path of the electrons and the small glancing angle is denoted by θ.

2.3 Reflection high-energy electron diffraction (RHEED)

RHEED is a technique used to characterize the surface of crystalline materials and gather information only from the surface layer of the sample, distinguishing RHEED from other materials characterization methods such as Transmission electron microscopy. A great source of information and details on RHEED was can be found in Ref. [40].

A RHEED system requires an electron source or RHEED gun, photoluminescent detector screen and a sample with a clean highly ordered surface. The electron gun generates a beam of electrons which strike the sample at a very small angle relative to the sample surface. Incident electrons diffract from atoms at the surface of the sample, and a small fraction of the diffracted electrons interfere constructively at specific angles and form regular patterns on the detector. The electrons interfere according to the position of atoms on the sample surface, so the diffraction pattern at the detector is a function of the sample surface [40]. Figure 2.3 show a simple schematic of the RHEED system within an MBE chamber. In the RHEED setup, only the top few layers of atoms contribute to the RHEED pattern due to the glancing angle of incident electrons, which prevents them from escaping the bulk of the sample and

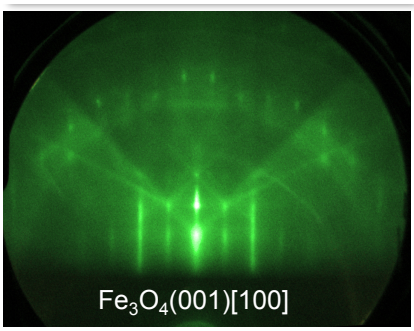

Figure 2.4: An example RHEED pattern for Fe_3O_4 in the [100] crystal direction.

reaching the detector [40]. Figure 2.4 shows a typical RHEED pattern of magnetite thin films grown on MgO(001) single crystal substrates.

Once the electrons scatter from the sample surface, The diffracted electrons interfere constructively at specific angles according to the crystal structure, spacing of the atoms, and the energy of the incident electrons. Any constructive interference at the detector surface shows up as bright spots (RHEED spots) or streaks (RHEED streaks) due to the photoluminescent screen and can be capture with a CCD camera (Fig. 2.4). Where and how many RHEED spots/streaks arises is shown in Fig. 2.5 [41]. In the figure 2.5 top, the surface of the sample is shown in reciprocal space. This reciprocal lattice builds a surface with an array of atoms. Assuming only elastic scattering of the electrons, the scattered wave vector k_{ij} lies on the surface of the sphere of constant energy, the Ewald sphere. The side view of this is shown in figure 2.5 bottom panel. In reciprocal space, the two-dimensional array of the surface atoms turns into the reciprocal rods and where ever the rod intersect the Ewald sphere, at that point is the condition for constructive interference creating the RHEED spots on the detection screen in real space. The RHEED spots created on the screen will follow the Laue

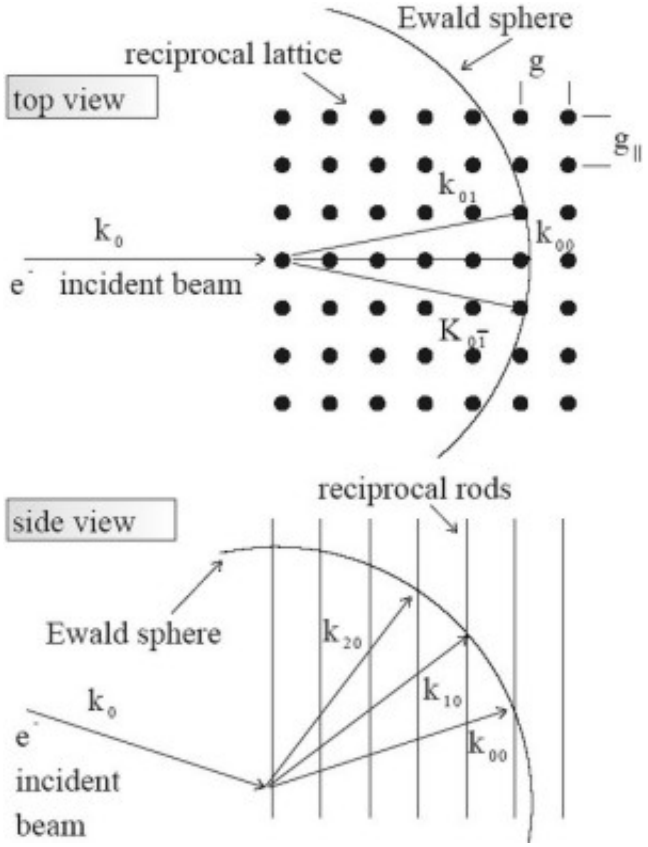

Figure 2.5: Adapted from Ref. [41]. Show the top view of the scattering for RHEED in reciprocal space.

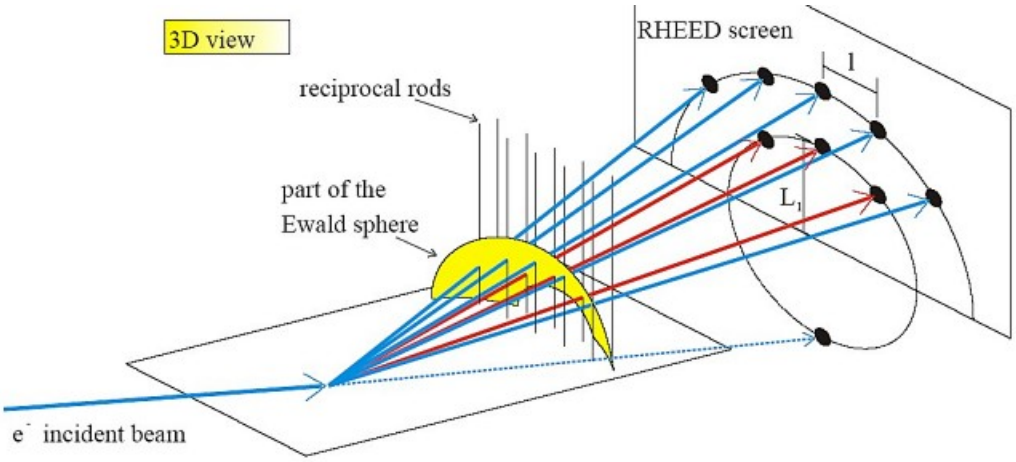

Figure 2.6: Adapted from Ref. [41]. Shows the directions of the elastically scattered electrons in real space.

circles which are numbered starting from zero [40, 41]. Figure 2.6 shows the spots for the Laue circle no. 0 (red arrows) and for Laue circle no. 1 is in cyan. Once the image is taken, it can be used to characterize the crystallography of the sample surface through analysis of the diffraction patterns.

In practice, the Ewald sphere actually has some thickness not infinitely thin as modeled theoretically. The reciprocal rods have a finite thickness also, so when the rods intersect the Ewald sphere, constructive interference happens over the whole cross section. The broadening of the cross section lead to the formation of RHEED streaks (as seen in fig. 2.4) in the RHEED pattern. Therefore, the width and length of the RHEED streaks give us an insight of the quality of the material. Streaky, thin, sharp patterns indicate atomically flat surfaces with long, coherent periodicity in the structure. Broader streaks indicate smaller coherence length in the crystal structure.

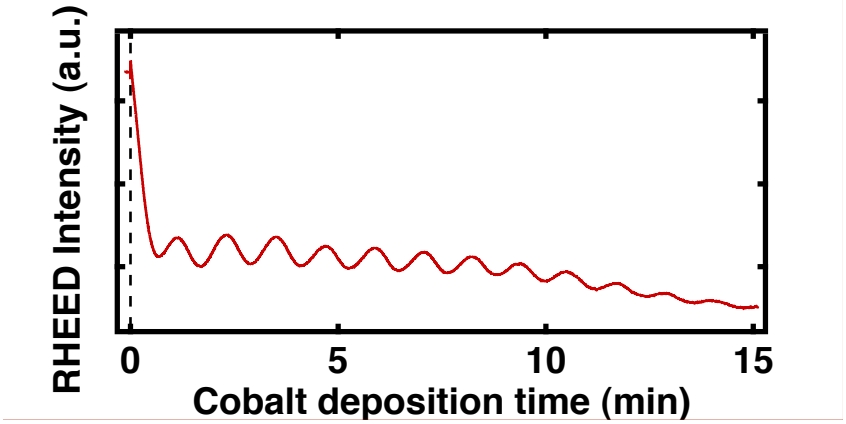

Figure 2.7: RHEED intensity oscillations for the growth of bcc Co on Fe/MgO(001). The dash line indicated when the Co shutter was open and 12 oscillations are seen, indicating that 12 ML of bcc Co grew in $\sim$15 minutes.

Another common measurement used is RHEED oscillation measurements. Here, a RHEED streak intensity is monitored throughout the growth. The intensities will fluctuate in a periodic manner as a result of the relative surface coverage of the growing thin film. Since the intensity of the RHEED streak or spot depends on the atomic order of the surface, the peaks will have a maximum intensity when the surface has maximum order. Likewise, the intensity will be the lowest at the minimum order. Therefore during the growth, intensity maximums will occur after each complete monolayer of material is grown and a minimum will occur when only half a monolayer of material is deposited. RHEED oscillations can give a very precise rate and more importantly, only happens for very pristine, high quality, single crystal epitaxial growth. A sample RHEED oscillation curve is shown in figure 2.7.

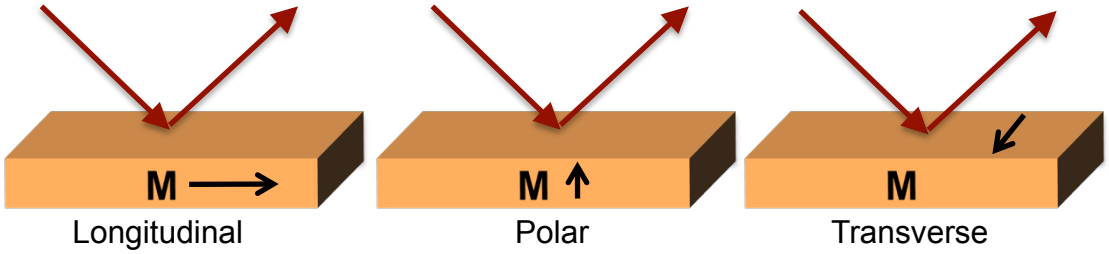

Figure 2.8: Here are the there different geometries for MOKE. The left is longitudinal MOKE, center is polar MOKE and right is transverse MOKE.

2.4 Magneto-optic Kerr Effect Measurement

The Magneto-optic Kerr Effect (MOKE) is a magneto-optics effects and it describe the change in polarization of an incident light beam after it is reflected off a magnetized surface. The change in polarization is proportional to the magnitude and direction of the magnetization and is used to characterize the magnetic properties of a magnetic material. Figure 2.8 shows the three different MOKE setups relating the plane of incidence and the magnetization.

In the longitudinal MOKE, the magnetization is parallel to both the surface and the plane of incidence. Typically, longitudinal MOKE is set up at an angle from the surface normal and show in figure 2.9. Linearly polarized light incident on the surface becomes elliptically polarized after reflecting off the surface of the magnetic material. The change in polarization directly proportional to the component of magnetization that is parallel to the reflection surface and parallel to the plane of incidence. When the magnetization is perpendicular to the surface plane and parallel to the plane of incidence, this effect is called the polar MOKE (Figure 2.8, center). To simplify the analysis, near normal incidence is usually employed

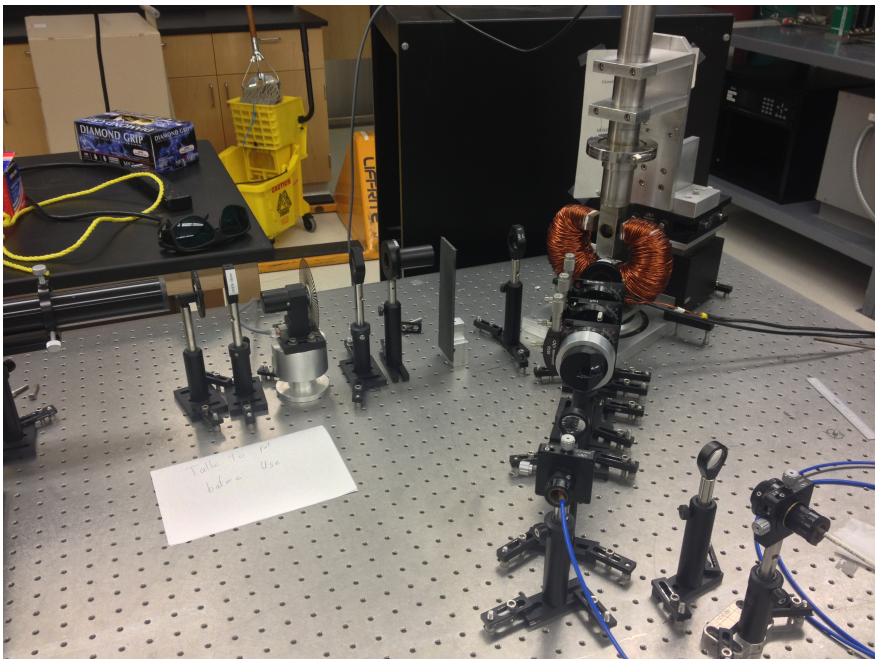

Figure 2.9: Longitudinal MOKE setup used within the research group.

when doing experiments in the polar geometry. Finally, if the magnetization is parallel to the surface of the magnetic material but perpendicular to the incident plane, this is transverse MOKE (Figure 2.8, right).

2.5 MgO Substrate Preparation and Growths

2.5.1 Annealing and e-beam deposition of MgO

MgO(001) substrate is the choice substrate for many of these studies for many reason. One reason is the ease of preparation of the MgO substrate and another is due to having a small lattice mismatch it has with many materials and is a great template for growing different materials. The MgO substrates are first rinsed in DI water and blown dry with nitrogen

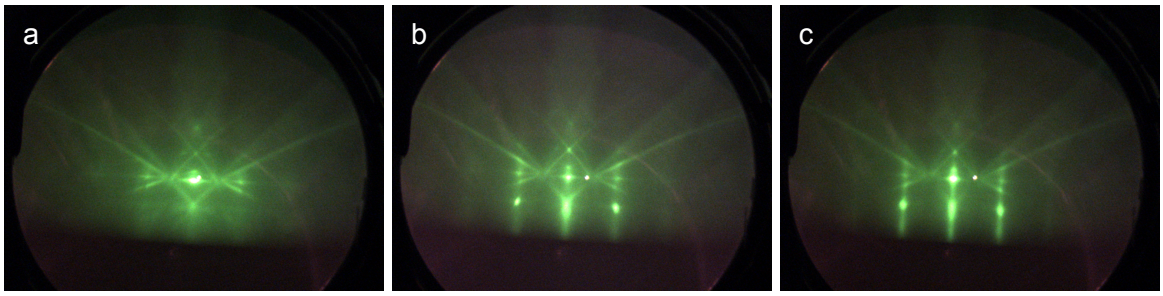

Figure 2.10: Preparation of MgO(001) substrates. (a) RHEED pattern in [100] direction of MgO(001) substrate before annealing, (b) after annealing at 600°C for 45 minutes and (c) after the growth of the 10 nm MgO buffer layer grown at 350°C.

gas. The substrate is then loaded into the molecular beam epitaxy (MBE) ultra high vacuum (UHV) growth system with a base pressure of 1×10^{-10} torr. The MgO substrate is annealed in UHV at 600°C for 45 minutes, while being monitored through in-situ reflection high-energy electron diffraction (RHEED). Once the annealing is complete, the substrate is then cooled to 350°C and a 10 nm MgO buffer layer is grown through electron beam (e-beam) deposition. Atomic force microscopy (AFM) of the MgO (10 nm)/MgO(001) shows that the RMS roughness decrease when compared to the annealed MgO substrate alone [ref] and sharpening of the RHEED pattern during the growth indicates the improvement of the atomic flatness and crystalline quality of the surface.

2.6 Reactive MBE

Lately molecular beam epitaxy has been used to deposit oxide materials for advanced electronic, magnetic and optical applications. One way to deposit oxide materials is through reactive MBE (rMBE), where a elemental material, such as Mg is evaporated inside an re-

active gas (i.e. oxygen) environment causing the material to react before the material hits the substrate. In the case of Mg, it will oxidize into MgO and MgO will deposit onto the substrate. In this section, I will use the growth of MgO through reactive MBE to give an example of this style of growth and a small introduction to the distillation technique.

2.6.1 Mg Distillation and MgO Homoepitaxy

At UHV pressures, Mg evaporates at reasonably low temperatures (< 500°C). Using a low temperature design effusion cell, I have followed the procedure for investigating distillation as developed for Eu. Fig. 2.11 demonstrates the processes for determining feasibility and the temperature above which the material while maintain distillaiton. Fig. 2.11 a) shows a 4 nm e-beam MgO buffer layer on MTI substrate. The substrate has been treated by deionized (DI) water rinse followed by 600 °C anneal in UHV. The MgO buffer layer is deposited at 350 °C. The sample is then heated to 500 °C for distillation testing. At 500 °C, the Mg cell is opened under UHV condition (no molecular oxygen leak). If the MgO RHEED pattern remains precisely unaltered, except for some possibility of a slight decrease in intensity, then Mg is under distillation condition. Fig. 2.11 b) displays the MgO buffer layer exposed to the Mg flux rate of what is supposed to be 4 Å/min as calibrated by the quartz crystal monitor. The RHEED pattern remains unaltered indicating that Mg has zero sticking probability to MgO at above 500 °C. The sample is then cooled to 300 °C and this temperature is maintained for $\sim$10 min. Again the RHEED pattern is unaltered, indicating distillation. The sample is then subsequently cooled to 200 °C and then 150 °C, which both indicate distillation, despite

being below the temperature of evaporation according to the thermal cell. At 55 °C (Fig. 2.11 f)), we see that the RHEED pattern is altered by increased Mg sticking probability and resulting Mg overlayer. The Mg cell is then closed and the sample is heated to 150 °C, where the Mg overlayer RHEED pattern begins to undergo changes possibly due to re-evaporation or atomic diffusion and smoothing associated with annealing process. Heating to 300 °C, as shown in Fig. 2.11 h) returns the sample to it's original RHEED pattern of the MgO buffer layer, demonstrating full re-evaporation of the deposited Mg layer of approximate thickness ≤ 8 nm. This is a remarkable result. We can then understand the excellent quality of e-beam MgO homoepitaxy in the following way. In the e-beam source, electrons bombard the source crystalline MgO target and dissociate Mg and O which normally leads to MgO with oxygen vacancies. However, deposition at elevated temperatures allows for surface diffusion of any Mg atoms, as well as distillation of excess Mg, leading to stoichiometric films.

2.6.2 MgO Homoepitaxy by rMBE

While e-beam MgO homoepitaxy provides excellent single crystal MgO surfaces for growth studies, the e-beam style of deposition is limited by growth rate and total thickness. The higher the rate of e-beam deposition (higher the power), the more oxygen vacancies are introduced. Also, e-beam rates in our MBE chamber, generally never exceed 3 Å/min because the source will run out of material very quickly. For this same reason, thick films above 10 nm are not really realistic. For instance, while doing growth studies that involve 10 nm buffer layers, running out of MgO is the main reason for chamber vents, on the order of

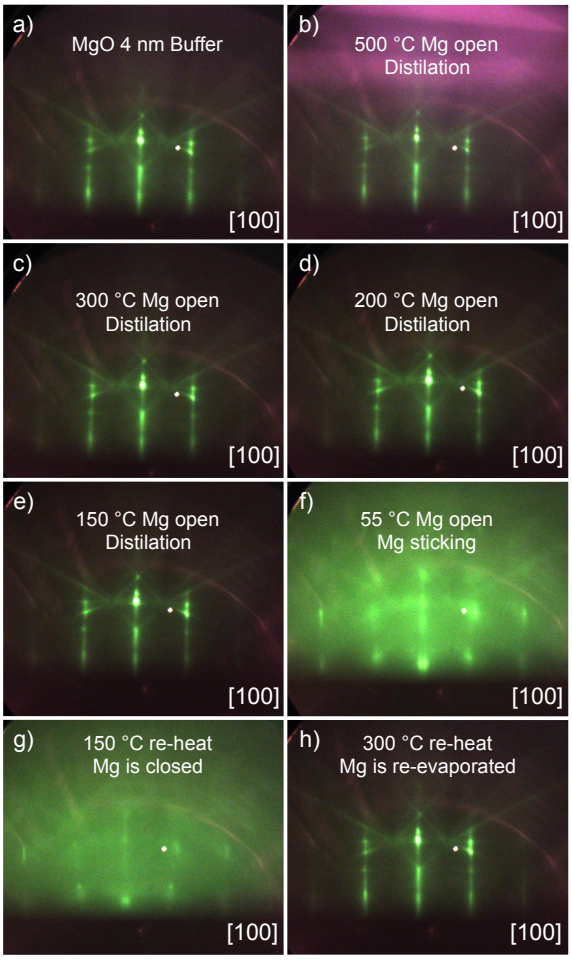

Figure 2.11: Evolution of Mg distillation. a) MgO (4 nm) e-beam buffer layer grown at 350 °C on MgO(001). b) same 4 nm MgO buffer layer exposed to a Mg flux at 500 °C. c) - d) The substrate temperature is the decreased sequentially with stops at 300 °C (c), 200 °C (d), 150 °C (e), and 55 °C (f). The sticking probability of Mg increases below 150 °C allowing for the growth of a metallic Mg overlayer. After 20 minutes of deposition at 55 °C, the Mg shutter is closed. g) The sample is then re-heated to 150 °C and the Mg overlayer pattern begins to change. h) The original MgO e-beam buffer layer pattern returns after post annealing the Mg/MgO system to 300 °C. This can be understood as re-evaporation of the Mg overlayer.

every 2 months. For each vent, it takes 1.5 - 2 weeks to get the chamber back up and fully running with clean material leading to a down time of 20%, which is not good for research. On the other hand, thermal evaporation sources of the high temperature variety, need refilling approximately every 2 vents ($\sim$4 – 6 months depending on usage). The low temperature

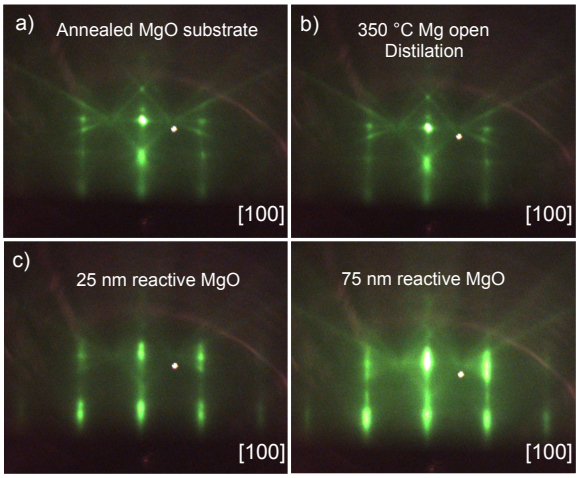

Figure 2.12: Homoepitaxy of reactively grown MgO on MgO(001). a) Annealed MgO(001) substrate. b) MgO substrate maintained at 350 °C and with incident Mg flux in distillation mode. c) 25 nm reactive growth of MgO through oxidation of elemental Mg flux. d) Final RHEED pattern of 75 nm rMBE MgO homoepitaxial film on MgO(001).

effusion cells require filling at most once per year. Therefore, having thermal sources is desirable if thicker MgO films are neeeded. With the discovery of Mg distillation, it then became feasible to grow thick ($>$ 100 nm) films, with only a moderate decrease in quality from the e-beam MgO growths.

Fig. 2.12 shows the RHEED patterns for rMBE homoepitaxy of MgO on MgO(001) substrate. The substrate is first DI rinsed and the subsequently UHV annealed at 600 °C for 1 hour (Fig. 2.12 a)). The sample is then cooled to RT to take a Mg deposition rate, which was determined to be 4.1 Å/min. The sample is then heated to 350 °C and the temperature is allowed to stabilize. Next, the Mg shutter is opened and the incident Mg flux, in distillation condiction, re-evaporates off the substrate surface leaving the RHEED pattern unaltered (Fig. 2.12 b)). The growth commences with the introduction of an oxygen partial pressure. Growth in the distillation regime for MgO differs, and is in fact simpler, from that of EuO growth. As

MgO is the thermodynamically stable oxide, there is no need to worry about other oxidation states, and therefore no need to worry about limiting the oxygen content supplied during the growth. Therefore, we can simply overpressure with oxygen such that the flux of oxygen exceeds the Mg flux supplied to the substrate. For the reactive growth shown in Fig. 2.12 c) and d), $P_{O_2} \sim 1 \times 10^{-7}$ Torr. After 75 nm of growth. To terminate the growth, since there is no concern for over-oxidation of the MgO overlayer, the Mg shutter is first closed. (This is opposite of EuO growth termination). The total chamber pressure increases from 1.0×10^{-7} to 1.6×10^{-7} Torr, indicating that at 4.1 Å/min of Mg, about $\sim 5 \times 10^{-8}$ Torr molecular oxygen partial pressure is needed to fully oxidize the incoming Mg flux. The final homoepitaxial MgO film of 75 nm is shown in figure 2.12 d). The RHEED indicates some islanding, and that the e-beam MgO produces higher quality crystalline surfaces (compare with fig. **??** d) and 2.11 a)), but that the growth by rMBE is really quite good.

References

[40] A. Ichimiya and P. Cohen, *Reflection high-energy electron diffraction* (Cambridge University Press, 2004).

[41] J. Klein, “Epitaktische Heterostrukturen aus dotierten Manganaten”, PhD thesis (Universität zu Köln, 2001).

Chapter 3

Induced Biquadratic coupling in Co/Fe/MgO/Fe

3.1 Background

The high values of room-temperature tunneling magnetoresistance (TMR) in Fe/MgO/Fe(001) and related MgO based magnetic tunnel junctions $\sim$400% have attracted considerable interest from both the scientific and technological communities [42–45]. The theoretical prediction of TMR values exceeding several thousand percent in ideal structures provides motivation to further improve the synthesis and characterization of MgO-based heterostructures [42, 46]. A central issue is the role of nonidealities such as interface oxidation, magnetic impurities, and oxygen vacancies in determining the magnetic and magnetotransport properties [47–54]. The interlayer exchange coupling IEC across MgO spacers is a fascinating phenomenon both

bilinear and biquadratic and provides a means of investigating the relationship between the spin-dependent properties and the nonideal aspects of the system [1, 17, 22, 50, 55–59]

In this chapter, we show that the biquadratic coupling in Co/Fe/MgO/Fe(001) is correlated with the interfacial oxidation and originates from indirect exchange interactions with magnetic impurities in the MgO spacer (i.e., the loose spin model[1]). Using molecular-beam epitaxy (MBE) synthesis and magneto-optic Kerr effect (MOKE) measurements across wedged samples, we systematically investigate the role of interfacial oxidation on the IEC across MgO. First, we find that the biquadratic coupling strength increases with the oxygen pressure during MgO growth. To isolate the interface vs bulk effect, we systematically vary the oxidation of the lower Fe/MgO interface while maintaining the oxygen content of the MgO film. In this manner, the biquadratic coupling is found to be correlated with the interfacial oxidation. Furthermore, the temperature dependence of the biquadratic coupling exhibits a strong increase at low temperatures and the loose spin model is able to quantitatively account for this behavior.

3.2 Experimental Procedures

Samples consisting of Ag(10 nm)/Co(50 nm)/Fe(5 nm)/MgO(wedge)/Fe(15 nm)/MgO(001) are grown on doubleside- polished MgO(001) substrates. Following a 30 min anneal of the MgO substrate at 600 °C, the bottom Fe layer (”free layer”) is grown at room temperature and subsequently annealed at 450 °C to generate an atomically flat surface. The reflection

high energy electron-diffraction (RHEED) pattern of the Fe film [Fig. 3.1a] has a weak 2×2 reconstruction which indicates the presence of carbon. to account for the higher den-

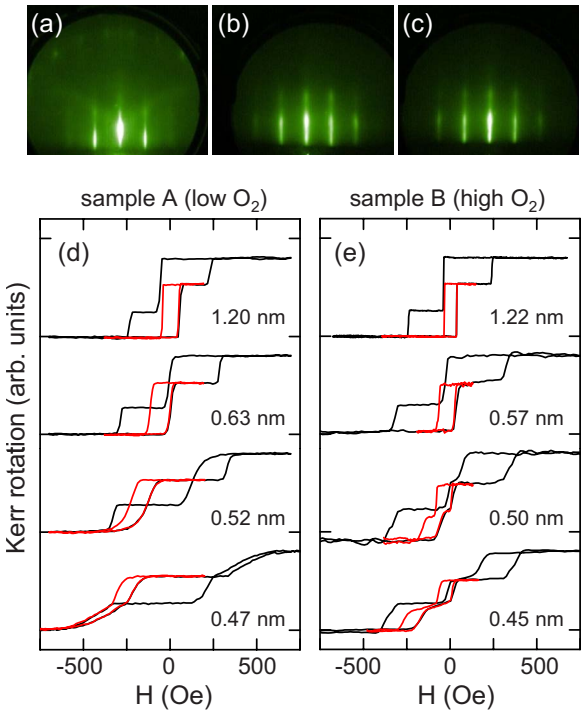

Figure 3.1: (a-c) RHEED patterns of the bottom Fe layer after annealing, MgO barrier layer grown at 2×10^{-8} torr, and MgO barrier layer grown at 2×10^{-7} torr, respectively, (d) Representative major (black) and minor (red) hysteresis loops for sample A at various t_{MgO}, (e) Representative major (black) and minor (red) hysteresis loops for sample B at various t_{MgO}.

sity of Mg in MgO. This rate In comparing samples with and without a MgO buffer layer to suppress carbon contamination, we find that there is no noticeable difference in the IEC, consistent with other studies[60]. Unless otherwise noted, the MgO layer is initiated by a 1 monolayer (ML) Mg template to reduce the oxidation of the bottom Fe interface[61]. Then oxygen gas (chamber pressure 2×10^{-8} torr) is introduced into the ultrahigh vacuum chamber and elemental Mg is deposited at room temperature at a rate of $\sim$0.06 nm/min to form

MgO. The MgO growth rate is determined by measuring the deposition rate of elemental Mg by a quartz deposition monitor and multiplying by 0.80 has been compared against RHEED oscillations on a calibration sample, and the rates agree to within 10%. Figures 3.1b and 3.1c show RHEED patterns for the MgO layers grown at chamber pressures of 2×10^{-8} and2×10^{-7} torr, respectively. Auger-electron spectroscopy on these films exhibits O/Mg peak ratios of 4.1 and 5.5, respectively. The RHEED patterns indicate that the MgO lattice is capable of maintaining flat single-crystalline structure while incorporating different amounts oxygen deficiency. Finally, the Co/Fe bilayer (hard layer") is deposited at room temperature and the entire structure is capped by Ag.

The effect of oxygen content on the IEC is investigated by comparing two wedged samples to MgO layers grown at different chamber pressures: 2×10^{-8} torr (sample A, "low O2") and 5×10^{-7} torr (sample B, "high O_2"). The IEC is expressed as

$$E = -J_1 \cos(\theta_F - \theta_H) + J_2 \cos^2(\theta_F - \theta_H) \tag{3.1}$$

where E is the energy per unit area, J_1 is the bilinear coupling coefficient, J_2 is the biquadratic coupling coefficient, and θ_F (θ_H) is the in-plane angle of the free (hard) layer magnetization. The magnetizations are in-plane due to magnetic shape anisotropy. The values of J_1 and J_2 are obtained as a function of MgO thickness (t_{MgO}) by measuring hysteresis loops via longitudinal MOKE with magnetic field (H) along the [100] in-plane direction of Fe. Figures 3.1d and 3.1e show representative hysteresis loops for samples A and B at various

t_{MgO}. For both samples, at large t_{MgO} the loops exhibit abrupt jumps at ∼30 Oe and ∼250 Oe, which correspond to the independent magnetization reversals of the free layer (bottom Fe) and hard layer (Co/Fe bilayer), respectively. The much higher coercivity of the hard layer enables the determination of both J_1 and J_2 (within the macrospin approximation [20]) by measuring minor hysteresis loops (red curves) in which the hard layer is not switched. The minor loops start at negative saturation so that the hard layer is always oriented along the negative direction (θ_H = 180°), and the energy per unit area of the free layer is therefore given by

$$E(\theta_F, H) = -(HM_F t_F - J_1)\cos(\theta_F) + J_2\cos^2(\theta_F) + K_F t_F \cos^2(\theta_F)\sin^2(\theta_F) \qquad (3.2)$$

where M_F is the magnetization, t_F is the thickness, and K_F is the cubic anisotropy of the free layer. The anisotropy, K_F, is determined by measuring the saturation field of a 15 nm Fe/MgO(001) sample with the field applied along the in- plane hard axis of the Fe (i.e. the [110] axis). At room temperature, K_F is 5.0×10^5 erg/cm^3 and increases to 6.9×10^5 erg/cm^3 at 5 K. Figure 3.2a illustrates the shifting (H_1) and splitting ($2H_2$) of the minor loop for sample B at t_{MgO} = 0.45 nm. The shifting and splitting of the minor loop yields values for J_1 and J_2 based on the energy minimization of equation (3.2). Through a change of variables to $h = H - H_1$ with $H_1 = J_1/M_F t_F$, the energy reduces to:

$$E(\theta_F, h) = -hM_F t_F \cos(\theta_F) + J_2\cos^2(\theta_F) + K_F t_F \cos^2(\theta_F)\sin^2(\theta_F) \qquad (3.3)$$

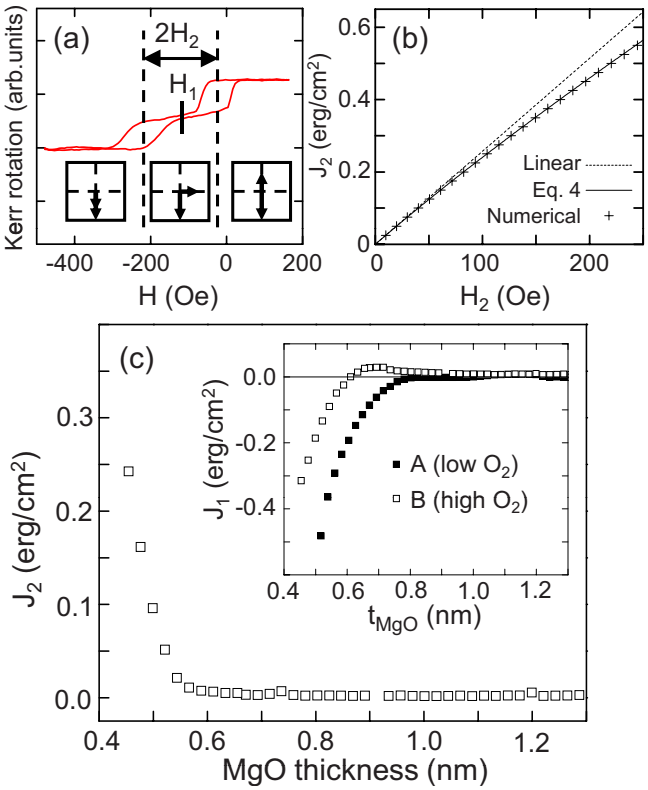

Figure 3.2: (a) Illustration of the shifting (H_1) and splitting ($2H_2$) of a minor hysteresis loop. The pictured loop is from sample B at t_{MgO} = 0.45 nm, (b) J_2 as a function of H_2 comparing Eq. (3.9) with numerical minimization of Eq. (3.3) and with $J_2 \approx H_2 M_F t_F$. We assume M_F = 1714 emu/cm^3 for Fe. (c) Biquadratic coupling coefficient J_2 as a function of t_{MgO} for sample B. Inset: Bilinear coupling coefficient J_1 as a function of t_{MgO} for samples A and B.

which implies that J_1 shifts the minor loop to be centered at H = H_1. In Figure 3.2a, the negative value of H_1 indicates antiferromagnetic (AF) coupling ($J_1 < 0$).

For biquadratic coupling ($J_2 > 0$), the minor loop splits due to 90° magnetization switchings of the free layer that occur when the global energy minimum changes from a saturated state ($\theta_F = 0°$ or 180°) to an intermediate state ($\theta_F \sim 90°$), or vice versa. For positive h, one local minimum is at positive saturation:

$$E_{sat} = -hM_F t_F + J_2 \tag{3.4}$$

Another local minimum is for the intermediate state near 90°, where we define a small angle δ by $\theta = 90° + \delta$ to yield

$$E_{int} = hM_F t_F \delta + J_2 \delta^2 + K_F t_F \delta^2 + O(\delta^3) \tag{3.5}$$

The condition for $|\delta| \ll 1$ is equivalent to $J_2 \ll K_F t_F$. Keeping up to the second order in δ, the value of E_{int} is minimized setting $dE_{int}/d\delta = 0$ and the corresponding energy is given by

$$E_{int} \approx -(hM_F t_F)^2/4(J_2 + K_F t_F) \tag{3.6}$$

The switching field H_2 is defined as the value h where the global energy minimum switches between E_{sat} and E_{int}. Thus, H_2 is given by $E_{sat} = E_{int}$ and by setting equation (3.4) equal to (3.6) gives,

$$-H_2 M_F t_F + J_2 \approx -(H_2 M_F t_F)^2/4(J_2 + K_F t_F) \tag{3.7}$$

and solving for H_2 yields

$$H_2 \approx \frac{2\left(J_2 + K_F t_F - \sqrt{K_F t_F (J_2 + K_F t_F)}\right)}{M_F t_F} \tag{3.8}$$

A similar expression for H_2 is obtained for the case of negative h, except that there is an overall negative sign. Therefore, the total splitting of the minor loop is given by $2H_2$. Solving

for J_2 yields the useful expression

$$J_2 \approx \frac{-K_F t_F + H_2 M_F t_F + \sqrt{K_F t_F (K_F t_F + 2 H_2 M_F t_F)}}{2} \tag{3.9}$$

In the limit of $J_2 \ll K_F t_F$, this reduces to the simple relation $J_2 \approx H_2 M_F t_F$. Figure 3.2b compares equation (3.9) with numerical minimization of equation (3.3) and with $J_2 \approx H_2 M_F t_F$, and we find that equation (3.9) is very accurate, while the linear relation is valid for lower values of H_2 (for $H_2 < 100$ Oe, the error is less than 10%). The improved accuracy of equation (3.9) compared to the simple relation $J_2 \approx H_2 M_F t_F$ is because the former keeps the higher order δ^2 terms in the calculations while the latter assumes $\delta = 0$.

Apart from the biquadratic coupling, we verify that the split loop does not originate from in-plane uniaxial magnetic anisotropy by measuring minor loops with the sample rotated in-plane by 90° and minor loops with equivalent splittings are observed; an uniaxial anisotropy would exhibit split loops only along one of these axes [62]. Another possible explanation of the split loop is the stabilization of the 90 alignment by a combination of four-fold anisotropy and AF coupling [63], which occurs in models that go beyond the macrospin approximation [64, 65]. Subsequent data will show that this effect does not contribute significantly to our results.

3.3 Results and Discussion

Looking at the representative minor loop for sample A at t_{MgO} = 1.20 nm (Fig. 3.1d), a square minor loop centered at the origin indicates the absence of J_1 and J_2 (below measurement sensitivity of ~0.005 erg/cm^2). With decreasing t_{MgO}, the minor loop shifts toward the negative field direction which corresponds to an increasing AF coupling strength. Interestingly, the minor loop does not split into two sub-loops at any t_{MgO} so that biquadratic coupling is not observed in this sample. At t_{MgO} = 0.47 nm, the AF coupling is so strong that the hard layer no longer remains at $\theta_H = 180^\circ$ during the minor loop sweep so that equation (3.2) is no longer valid and J_1 and J_2 are not easily determined. Turning to sample B (Fig. 3.1e), at t_{MgO} = 1.22 nm a square minor loop centered at the origin indicates the absence of interlayer coupling within the measurement sensitivity. At t_{MgO} = 0.57 nm, the minor loop is centered on a negative field direction which indicates AF coupling. At t_{MgO} = 0.50 nm, the minor loop begins to split which indicates the presence of biquadratic coupling ($J_2 > 0$), and at 0.45 nm the magnitudes of J_1 and J_2 have increased further.

The detailed dependence of J_1 and J_2 on t_{MgO} is obtained by scanning the MOKE measurement along the MgO wedge (Fig. 3.2c). On sample A, biquadratic coupling is not observed for any t_{MgO}. On sample B (open squares), the biquadratic coupling has a value of 0.24 erg/cm^2 at 0.45 nm, decreases monotonically with increasing t_{MgO}, and becomes undetectable beyond t_{MgO} ~0.6 nm. The presence of J_2 in sample B and the absence of J_2 in sample A implies that the oxygen content is an important factor for generating the bi-

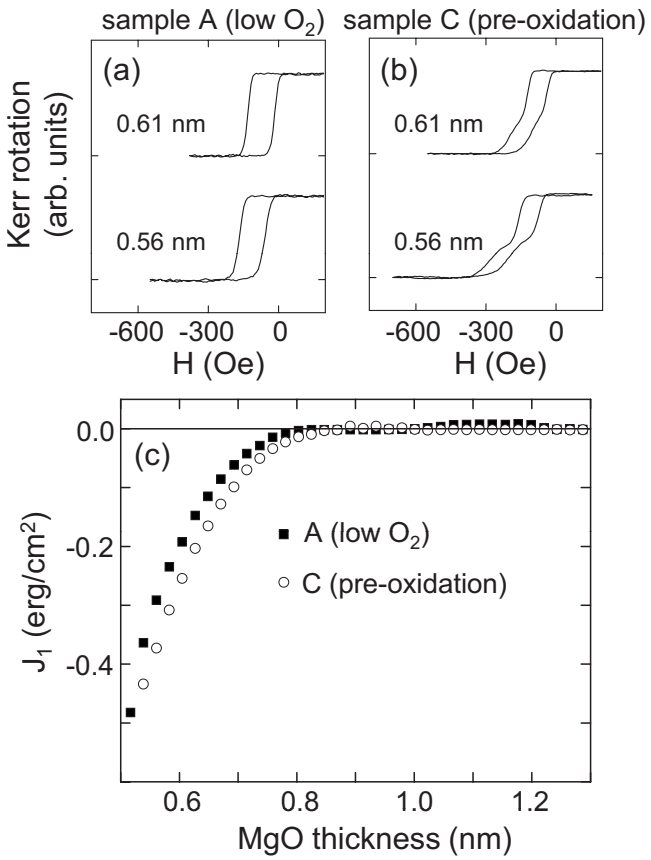

Figure 3.3: (a) Minor hysteresis loops from sample A at various t_{MgO}, (b) Minor hysteresis loops from sample C at corresponding t_{MgO}. (c) A comparison of bilinear coupling for samples A and C as a function of t_{MgO}.

quadratic coupling. In terms of J_1, both samples exhibit AF coupling whose strength decays with increasing t_{MgO} (inset of Fig. 3.2c), and sample B experiences a crossover to weak ferromagnetic coupling at t_{MgO} = 0.60 nm. This behavior is consistent with previous experimental and theoretical studies [50, 55, 56]. The stronger AF coupling in sample A may either be due to having more oxygen vacancies (cf. impurity state model [50]) or a decrease in the barrier height (cf. spin-dependent tunneling model [17, 55, 57]), but further studies are needed to determine the physical origin of J_1.

To gain insight into the origin of the biquadratic coupling, we systematically vary the bottom Fe/MgO interface to separate the interface vs. bulk effect with regard to the role of oxygen content. In a first approach, we grow a sample that combines a higher level of Fe/MgO interface oxidation with low oxygen content for the MgO film (sample C, pre- oxidized). This is accomplished by exposing the sample to 2×10^{-6} torr oxygen pressure for $\sim$2 minutes after the 1 ML Mg template is deposited. Then the oxygen pressure is reduced to 2×10^{-8} torr and the Mg is deposited to form an MgO film with oxygen content similar to sample A. Figures 3.3a and 3.3b show representative minor loops from samples A and C, respectively, for various t_{MgO}. While the minor loops from sample A do not exhibit any splittings, the minor loops from sample C show noticeable splittings at corresponding thicknesses. Although the split loops are not perfectly symmetric, it clearly indicates biquadratic coupling. This provides strong evidence that the biquadratic coupling is correlated to interfacial oxidation (which is present to some degree in all Fe/MgO interfaces [47]). In comparing the bilinear coupling in samples A and C (Fig. 3.2c), the values of J_1 are very similar for the

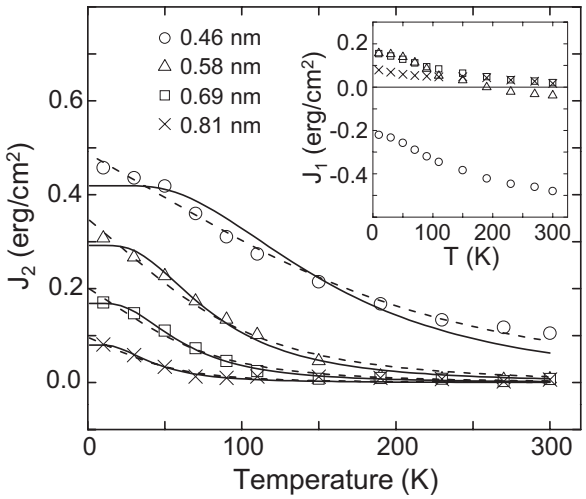

Figure 3.4: Temperature dependence of biquadratic coupling on a step-wedge sample at t_{MgO} = 0.46 nm, 0.58 nm, 0.69 nm, and 0.81 nm. Solid lines are curve fits based on the loose spin model with loose spins located at the interfaces (U_1 and U_2 are fitting parameters and c = 2). Dashed lines are curve fits based on the loose spin model with loose spins uniformly distributed throughout the spacer (c and $U_1 = U_2$ are fitting parameters). Inset: Temperature dependence of bilinear coupling for t_{MgO} = 0.46 nm, 0.58 nm, 0.69 nm, and 0.81 nm.

two samples. This data argues against pinholes as the origin of J_2 (Ref. [55]) because pinholes should promote ferromagnetic coupling in J_1, but the enhancement of J_2 in sample C is not accompanied by a shift in J_1 toward ferromagnetic coupling. The data also argues against the major contribution to the split loops originating from four-fold anisotropy + AF coupling because the increase in the splitting of the loops should be accompanied by an increase in the AF coupling [64, 65], but this is not observed.

To investigate the origin of the biquadratic coupling, we measure the temperature dependence of IEC on a MgO step- wedge sample with the MgO grown at 4×10^{-7} torr (sample D). Figure 3.4 shows the temperature dependence of J_1 and J_2 for t_{MgO} = 0.46 nm, 0.58 nm, 0.69 nm, and 0.81 nm. J_2 is calculated from equation (3.9) with K_F values measured as a function of temperature. J_2 increases dramatically at low temperatures, while J_1 shifts

toward ferromagnetic coupling. This behavior (including a sign change in J_1 for t_{MgO} = 0.58 nm) is not explained by existing models of the bilinear coupling [17, 50, 57], so further study is necessary. We note that this behavior is also present on samples where the MgO layer is grown by e-beam deposition and samples employing a MgO buffer layer to suppress carbon contamination. This behavior argues against any major contribution from the fold-fold anisotropy + AF effect because the splitting of the loops increases while the AF coupling decreases, which is opposite of the predicted behavior for this mechanism [64, 65]. In addition, substantial splitting is observed at low temperatures even in the absence of AF coupling. Therefore, it is clear that the observed changes in the splitting are due to the biquadratic coupling. The strong temperature dependence of J_2 is consistent with biquadratic coupling mediated by magnetic impurities in the spacer (loose spin model) [1]. Because J_2 is correlated to interfacial oxidation, we first perform the fitting for interfacial loose spins (c = 2, $U_1 \neq U_2$), where c is the fractional concentration of loose spins and U_1 and U_2 are the exchange couplings between a loose spin and the ferromagnetic layers [1]. The solid lines in Figure 3.4 are the best fit with values of $|U_1|/k_B$ = 27.4 K, 16.5 K, 10.9 K, and 6.34 K and $|U_2|/k_B$ = 299.3 K, 155.1 K, 117.6 K, and 83.8 K, for t_{MgO} = 0.46 nm, 0.58 nm, 0.69 nm, and 0.81 nm, respectively. In another approach, if the loose spins are uniformly distributed throughout the spacer, then one assumes that $U_1 = U_2$ and c is treated as a fitting parameter [1]. The dashed curves are the best fit with values of $|U_1|/k_B = |U_2|/k_B$ = 344.8 K, 166.2 K, 125.1 K, and 89.8 K and c = 0.025, 0.03, 0.023, and 0.016 for t_{MgO} = 0.46 nm, 0.58 nm, 0.69 nm, and 0.81 nm, respectively. Both fitting approaches are able to account for the

strong temperature dependence, but neither approach is clearly better. The data exhibits hints of plateaus at the lowest temperatures, which is a characteristic of interfacial loose spins and the first approach produces somewhat better fits for t_{MgO} = 0.58 nm and 0.69 nm. On the other hand, the second approach has a better fit for t_{MgO} = 0.46 nm. A possible scenario is that the magnetic impurities segregate away from the interface during MgO growth. Most importantly, regardless of the exact spatial distribution of the loose spins, this model is able to quantitatively account for the strong temperature dependence of J_2. On the other hand, other possible sources of biquadratic coupling such as the interfacial step mechanism [22] and the magnetic dipole mechanism [66] cannot explain the temperature dependence even qualitatively. Thus, the experimental evidence strongly supports the loose spin mechanism as the origin of the biquadratic coupling across MgO.

3.4 Conclusion

In summary, by varying the oxygen pressure during the MgO growth and using minor hysteresis loop analysis, we demonstrate that the IEC depends on the oxygen content within the Co/Fe/MgO/Fe system. Samples with MgO grown at low oxygen pressure exhibit only bilinear coupling, while samples with MgO grown at high oxygen pressure exhibit both bilinear and biquadratic coupling. Further investigation reveals that the presence of biquadratic coupling is due to the oxidation of the lower MgO/Fe interface. Finally, the strong temperature

dependence of the biquadratic coupling and quantitative analysis of the data provides strong evidence for the loose spin mechanism as the source of the biquadratic coupling.

References

[1] J. Slonczewski, Journal of applied physics **73**, 5957 (1993).

[17] P. Bruno, Phys. Rev. B **49**, 13231 (1994).

[20] S. Demokritov, Journal of Physics D: Applied Physics **31**, 925 (1998).

[22] J. C. Slonczewski, Phys. Rev. Lett. **67**, 3172 (1991).

[42] W. H. Butler, X.-G. Zhang, T. C. Schulthess, and J. M. MacLaren, Phys. Rev. B **63**, 054416 (2001).

[43] S. Parkin, C. Kaiser, A. Panchula, P. Rice, B. Hughes, M. Samant, and S. Yang, Nature materials **3**, 862 (2004).

[44] S. Yuasa, T. Nagahama, A. Fukushima, Y. Suzuki, and K. Ando, Nature materials **3**, 868 (2004).

[45] S. Yuasa, A. Fukushima, H. Kubota, Y. Suzuki, and K. Ando, Applied Physics Letters **89**, 042505 (2006).

[46] X.-G. Zhang and W. H. Butler, Phys. Rev. B **70**, 172407 (2004).

[47] H. L. Meyerheim, R. Popescu, N. Jedrecy, M. Vedpathak, M. Sauvage-Simkin, R. Pinchaux, B. Heinrich, and J. Kirschner, Phys. Rev. B **65**, 144433 (2002).

[48] X.-G. Zhang, W. H. Butler, and A. Bandyopadhyay, Phys. Rev. B **68**, 092402 (2003).

[49] C. Tusche, H. L. Meyerheim, N. Jedrecy, G. Renaud, A. Ernst, J. Henk, P. Bruno, and J. Kirschner, Phys. Rev. Lett. **95**, 176101 (2005).

[50] M. Y. Zhuravlev, E. Y. Tsymbal, and A. V. Vedyayev, Phys. Rev. Lett. **94**, 026806 (2005).

[51] B. D. Yu and J.-S. Kim, Phys. Rev. B **73**, 125408 (2006).

[52] P. G. Mather, J. C. Read, and R. A. Buhrman, Phys. Rev. B **73**, 205412 (2006).

[53] J. Velev, K. Belashchenko, S. Jaswal, and E. Tsymbal, Applied physics letters **90**, 072502 (2007).

[54] C. Tusche, H. L. Meyerheim, N. Jedrecy, G. Renaud, and J. Kirschner, Phys. Rev. B **74**, 195422 (2006).

[55] J. Faure-Vincent, C. Tiusan, C. Bellouard, E. Popova, M. Hehn, F. Montaigne, and A. Schuhl, Phys. Rev. Lett. **89**, 107206 (2002).

[56] T. Katayama, S. Yuasa, J. Velev, M. Zhuravlev, S. Jaswal, and E. Tsymbal, Evgeny Tsymbal Publications, 3 (2006).

[57] J. C. Slonczewski, Phys. Rev. B **39**, 6995 (1989).

[58] E. Snoeck, P. Baules, G. BenAssayag, C. Tiusan, F. Greullet, M. Hehn, and A. Schuhl, Journal of Physics: Condensed Matter **20**, 055219 (2008).

[59] B. Heinrich, Z. Celinski, J. F. Cochran, A. S. Arrott, K. Myrtle, and S. T. Purcell, Phys. Rev. B **47**, 5077 (1993).

[60] C. Tiusan, M. Sicot, J. Faure-Vincent, M. Hehn, C. Bellouard, F. Montaigne, S. Andrieu, and A. Schuhl, Journal of Physics: Condensed Matter **18**, 941 (2006).

[61] Y. Lu, C. Deranlot, A. Vaurès, F. Petroff, J. George, Y. Zheng, and D. Demailles, Applied Physics Letters **91**, 222504 (2007).

[62] W. Weber, C. H. Back, A. Bischof, C. Würsch, and R. Allenspach, Phys. Rev. Lett. **76**, 1940 (1996).

[63] C. Bellouard, J. Faure-Vincent, C. Tiusan, F. Montaigne, M. Hehn, V. Leiner, H. Fritzsche, and M. Gierlings, Phys. Rev. B **78**, 134429 (2008).

[64] W. Folkerts and S. Purcell, J. Magn. Magn. Mater. **111**, 306 (1992).

[65] J. Cochran, J. Magn. Magn. Mater. **147**, 101 (1995).

[66] S. Demokritov, E. Tsymbal, P. Grünberg, W. Zinn, and I. K. Schuller, Phys. Rev. B **49**, 720 (1994).

Chapter 4

Tailoring Interlayer Exchange Coupling of Ferromagnetic Films across MgO with Fe nanoclusters

4.1 Background

The scaling of magnetic materials down to nanoclusters has led to interesting magnetic and spin-dependent properties.[67–75] One of the most fascinating magnetic properties is the interlayer exchange coupling (IEC) across MgO, which originates from spin-dependent tunneling between the ferromagnetic layers.[24, 55, 56, 76, 77] An interesting issue is the effect of nanoscaling on the behavior of IEC across MgO. Recently, theoretical studies have explored some aspects of this issue and predict that the IEC can be strongly affected by the

type and position of impurities in the MgO.[50, 78] Experimentally, however, the role of nanoclusters or other impurities on the IEC across MgO remains an open question. In this chapter, we utilize the magneto-optic Kerr effect (MOKE) to examine the IEC in Fe/MgO/Fe and Fe/MgO/Co systems with magnetic Fe nanoclusters (NC) embedded in the MgO spacer. Samples are grown by molecular-beam epitaxy (MBE) and utilize wedged MgO films to independently vary the lm thickness and the position of the Fe NC. By varying the position of the Fe NC within the MgO spacer, the bilinear coupling (J_1) exhibits strong variations in magnitude and can even switch between antiferromagnetic and ferromagnetic. We find that the main features of the data are explained by a model that assumes only pairwise coupling. Surprisingly, the IEC between Fe NC and a FM lm exhibits a strong dependence on the lm material (Co vs Fe): the Fe NC-Co layer coupling is 160% stronger than the Fe NC-Fe layer coupling. When compared to the analogous thin-lm systems at comparable spacing, the coupling in Fe/MgO/Co is only 20% stronger than the coupling in Fe/MgO/Fe, showing there is an enhanced material dependence of the IEC due to nanoscaling effects.

4.2 Experimental Procedures

4.2.1 Sample Growth

All samples are grown on double-side-polished MgO(001) substrates using MBE in ultrahigh vacuum (UHV) with a base pressure of $\sim 1 \times 10^{-10}$ torr. The MgO material is deposited by electron-beam evaporation at a rate of ∼0.2 nm/min. The other materials (Co,

Fe, and Ag) are deposited from thermal effusion cells at a rate of ∼0.15 nm/min. Deposition rates are determined by a quartz deposition monitor and are verified through reflection high-energy electron diffraction (RHEED) intensity oscillations. Substrates are prepared by a pre-rinse in DI water and then annealed at 600 °C in UHV until a clear RHEED pattern is achieved (∼45 min.). The substrate is subsequently cooled to 350 °C followed by the deposition of a 10 nm MgO buffer layer which produces sharp streaky RHEED patterns [44, 56] as shown in Fig.4.1(C)[taken at room temperature (RT)]. Besides improving the surface quality, the buffer layer also helps eliminate any contamination that may arise from impurities in the substrate.[60]

Two types of samples are investigated in this study [Figs. 4.1(A) and 4.1(B)]. Both have a free magnetic layer with low coercivity (∼30 Oe), a hard magnetic layer with high coercively (∼350 Oe), and an MgO spacer layer which may have embedded magnetic NC. For the Fe/MgO/Fe samples [Fig. 4.1(A)], the free layer consists of a 15 nm Fe layer grown on top of the MgO buffer layer at RT and annealed at 450 °C for 15 minutes, leading to a sharp RHEED pattern [Fig. 4.1(D)]. For the Fe/MgO/Co samples [Fig. 4.1(B)], an additional 4 monolayers (ML) of Co is deposited at RT on top of the Fe to complete the free layer. Typical Co deposition on Fe exhibits RHEED oscillations and a sharp RHEED pattern [Figs. 4.1(E) and 4.1(F)], confirming the epitaxial growth with bcc structure.[45, 79, 80]

The MgO spacer is deposited at RT and wedged films of various geometries are used to vary the MgO thickness and/or the position of embedded magnetic NC within the MgO. The magnetic NC consist of 1/4 ML of Fe deposited at RT. It is well known that Fe grows

as nanoclusters on top of MgO.[54, 81–83] After completing the MgO spacer, a hard layer consisting of Co(50 nm)/Fe(5nm) and a capping layer consisting of MgO(10 nm)/Ag(10 nm) are deposited at RT.

4.2.2 MOKE Measurements

Magnetic characterization of the sample is done by *ex situ* longitudinal MOKE measurement with the applied magnetic field along the [100] in-plane direction of the Fe. The laser beam is incident through the MgO substrate to measure both the free and hard layer magnetizations. A typical hysteresis loop [Fig. 4.1(G), dashed curve] exhibits a switching of the free layer ($\sim$30 Oe) followed by a switching of the hard layer ($\sim$350 Oe). Minor hysteresis loops [Fig. 4.1(G), solid curve] are measured to determine J_1 according to $J_1 = H_1 M_{free} t_{free}$, where H_1 is center position of the minor loop, M_{free} is the magnetization of the free layer (Black Arrow), and t_{free} is the free layer thickness.[24, 55, 56] A negative H_1 indicates antiferromagnetic (AF) coupling ($J_1 < 0$) and a positive H_1 indicates FM coupling ($J_1 > 0$). For some cases of low MgO thickness, the AF coupling becomes so strong that the hard layer does not remain pinned and this method cannot be used to determine J_1.[24]

4.3 Results

4.3.1 Interlayer exchange coupling without nano clusters

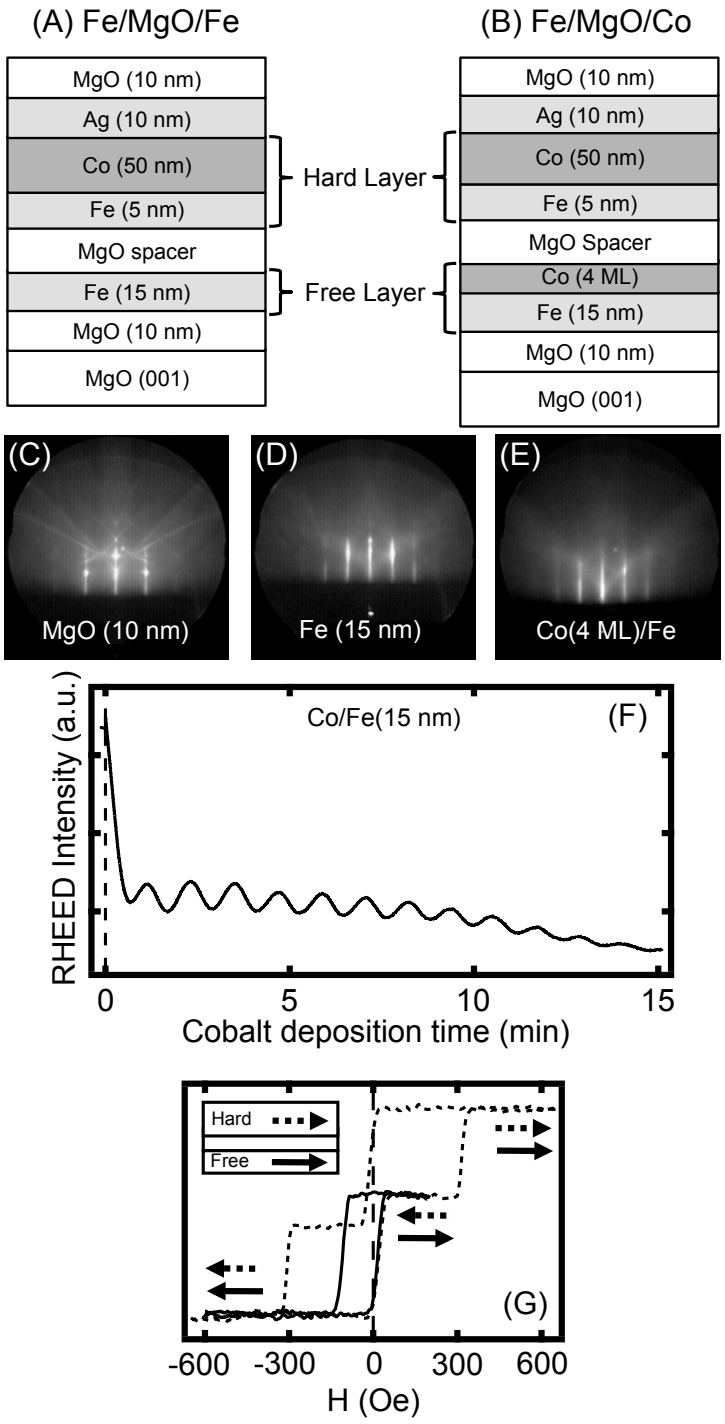

Figure 4.1: Interlayer Exchange Coupling Sample structures and Characterization. (A) Complete layer structure for the Fe/MgO/Fe system. (B) Complete layer structure for the Fe/MgO/Co system. (C)-(E) RHEED patterns for the MgO buffer layer, Fe (15 nm) free layer after annealing, and Co(4 ML) / Fe(15 nm), respectively. (F) Typical RHEED intensity oscillations for Co growth on Fe (15 nm). (G) Representative major hysteresis loop (dashed line) and the corresponding minor hysteresis loop (solid line) for Fe/MgO/Fe with MgO thickness=0.67 nm.

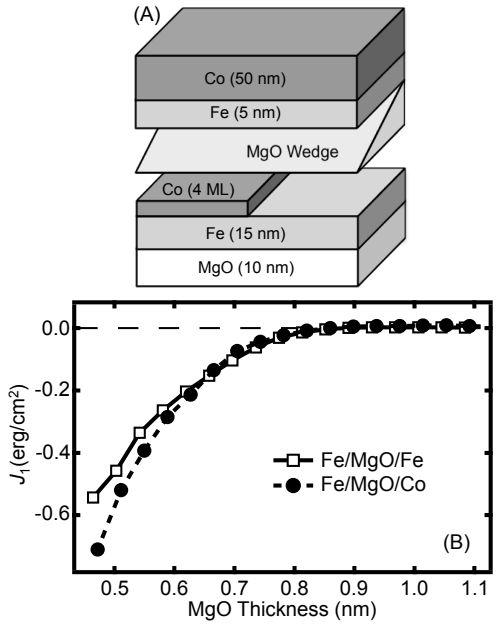

Figure 4.2: Interlayer exchange coupling without nano clusters. (A) Geometry of Sample A, with Fe/MgO/Co (left side) and Fe/MgO/Fe (right side) grown on the same sample and with a wedged MgO spacer, (B) Bilinear coupling J_1 as a function of MgO thickness for Fe/MgO/Fe (white squares) and Fe/MgO/Co (black circles).

We first investigate J_1 as a function of MgO thickness in both the Fe/MgO/Fe and Fe/MgO/Co systems by using the MgO wedge structure shown in Fig. 4.2(A). To avoid sample-to-sample variations, the Fe/MgO/Fe and Fe/MgO/Co systems are grown on the same sample by depositing the 4 ML Co layer on half of the sample. This sample, denoted as sample A, allows us to directly compare couplings found in Fe/MgO/Fe and Fe/MgO/Co and investigates any material dependence in IEC.

Figure 4.2(B) shows the detailed dependence of J_1 on MgO thickness for Fe/MgO/Fe (white squares) and Fe/MgO/Co (black circles) obtained by scanning MOKE along the MgO wedge. At high MgO thicknesses ($>$0.85 nm), both systems show very little to no coupling (below our measurement resolution of $\sim$0.005 erg/cm^2). As the MgO thickness decreases be-

low ∼0.85 nm, the coupling is AF and increases in strength with decreasing MgO thickness. The curves for Fe/MgO/Fe and Fe/MgO/Co are similar for MgO thickness down to ∼0.65 nm. Below MgO thickness of 0.65 nm, the curves deviate from each other with maximum measured 22 $J_1 = -0.54$ erg/cm^2 for Fe/MgO/Fe and $J_1 = -0.70$ erg/cm^2 for Fe/MgO/Co at MgO thickness of 0.47 nm (∼30% difference).

In the region of MgO thickness below 0.47 nm (∼2.1 ML) the coupling cannot be determined through minor loop analysis due to strong AF coupling. Qualitatively, in this low MgO thickness region, the coupling for Fe/MgO/Co changes very drastically to FM coupling at an MgO thickness of ∼0.43 nm. For Fe/MgO/Fe, the coupling is strongly AF down to MgO thickness of ∼0.31 nm and the coupling transitions to FM coupling at an MgO thickness of ∼0.27 nm.

4.3.2 Effect of Fe nanoclusters on the interlayer exchange coupling

We explore the effect of embedding Fe NC within the MgO spacer in both the Fe/MgO/Fe and Fe/MgO/Co systems. To systematically study the dependence of J_1 on both NC position and MgO thickness, we use the MgO double-wedge spacer shown in Fig. 4.3. The two MgO wedges are grown along perpendicular directions and have the Fe NC sandwiched in between. By scanning along the double wedge from B to D, we can obtain J_1 as a function of MgO thickness while keeping the NC at the same relative position (i.e., in the middle of the spacer). By scanning from A to C, we are able to determine J_1 as a function of NC position while keeping the total MgO thickness fixed.[84, 85] At point A the NC is located at the hard

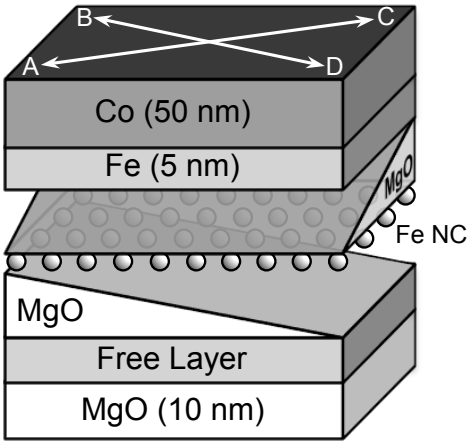

Figure 4.3: Schematic for the double-wedge MgO spacer used for Sample B and Sample C. Moving from point A to point C, the total MgO thickness is constant while the position of the Fe nanoclusters (NC) changes. Moving from point B to point D, the total MgO thickness changes.

layer/MgO interface, and at point C the NC is located at the free layer/MgO interface. For this study, we focus primarily on the line scans parallel to AC to systematically measure J_1 versus NC position at various total thicknesses of MgO.

First, we examine the coupling in the Fe/MgO/Fe system with NC, which we denote as sample B. The line cuts of J_1 versus NC position are shown in Fig. 4.4(A) at MgO thickness of 1.04 nm (blue or black circles), 0.85 nm (green or gray diamonds), 0.75 nm (orange or gray triangles), 0.70 nm (red or gray circles), and 0.66 nm (black squares). The dashed lines are guides to the eye. For Figs. 4.4(A) and 4.4(B), the NC position is relative to the center of the MgO spacer, with negative numbers for NC location near the free layer and positive numbers for NC location near the hard layer [Fig. 4.4(C)]. An interesting feature is the W-shape in most of the J_1 versus NC position line cuts, which are fairly symmetric about the zero NC position (center of MgO spacer). The W-shape curves show that the coupling can

be tuned in strength by changing the location of the NC within the MgO spacer. Looking at an MgO thickness of 0.70 nm and starting from the most negative position, we see J_1 has a similar value found in the Fe/MgO/Fe of sample A.

This is expected since the NC have merged with the free layer, resulting in a pure Fe/MgO/Fe system. As the NC move away from the free layer interface towards the center of the MgO spacer, we see that the AF coupling becomes stronger, reaching a value of $J_1 = -0.13$ erg/cm^2 at a NC position of -0.28 nm. When the NC approaches the zero position in the MgO spacer (middle), the AF coupling decreases in strength, reaching a minimum $J_1 = -0.005$ erg/cm^2. Now, as the NC moves towards the hard layer interface, J_1 increases in AF strength ($J_1 = -0.10$ erg/cm^2 at NC position $+0.25$ nm) before decreasing to a value similar in sample A at the positive end point. For MgO thickness $=0.75$ nm, the same trend is observed but the J_1 switches from AF to FM as the NC moves to the middle of the MgO spacer showing that the sign of J_1 can even be switched by NC position. The tailoring of J_1 can be further seen in a contour plot of J_1 as a function of Fe NC position (x axis) and MgO thickness (y axis) [Fig. 4.4(B)]. The magnitude of J_1 is fairly symmetric about the central Fe NC position (vertical dashed lineblack). This can be seen by the symmetric contour lines for negative J_1 values (blue region or below zero contour), which is expected due to the symmetric W-shape trend seen in the line cuts. At higher MgO thickness (>0.85 nm), there is a slight positional asymmetry with the ferromagnetic peak off center. This might be due a growth-induced asymmetry caused by vertical diffusion.

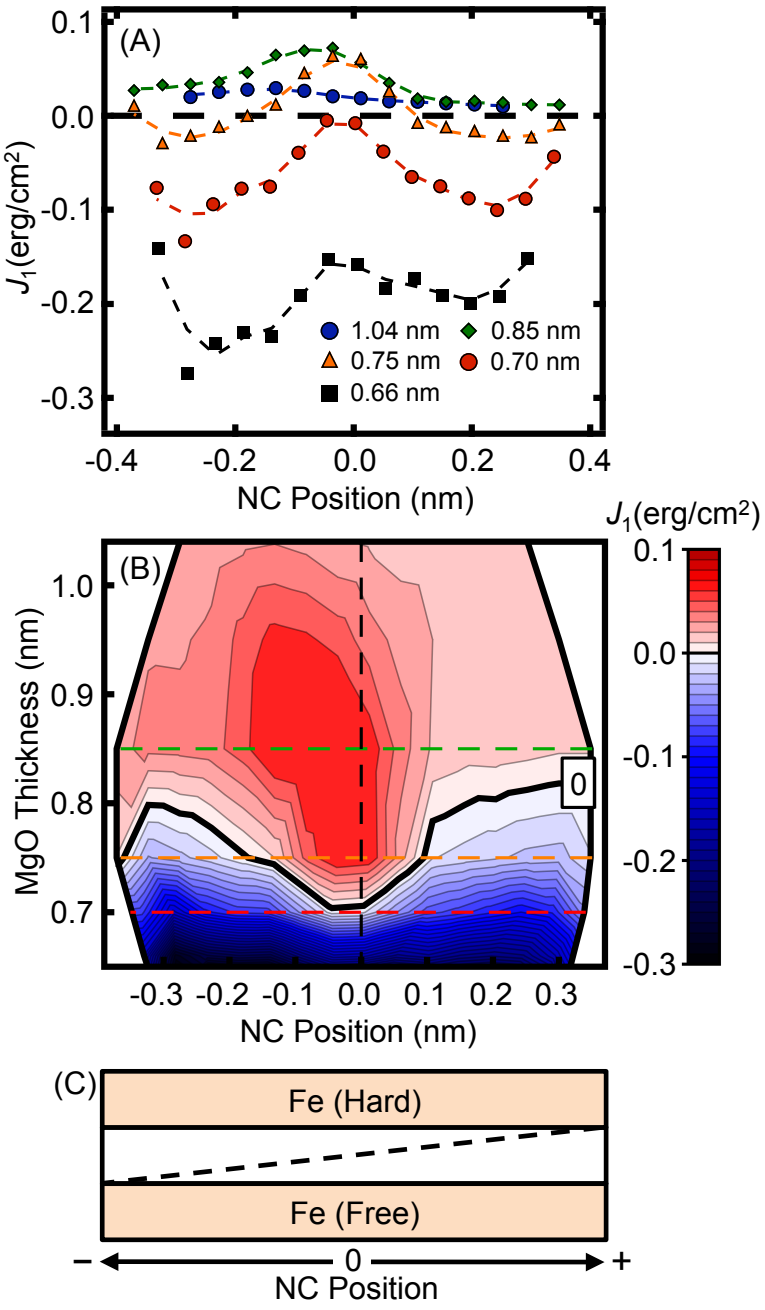

Figure 4.4: Bilinear coupling in Sample B: Fe/MgO/Fe with Fe NC. (A) J_1 as a function of the NC position at MgO thicknesses of 1.04 nm (blue circles), 0.85 nm (green diamonds), 0.75 nm (orange triangles), 0.70 nm (red circles), and 0.66 nm (black squares), (B) Contour/color plot of J_1 with red for FM regions, blue for AF regions, and thick black line for the J_1 = 0 erg/cm^2 contour. Green, orange and red dashed lines correspond to line cuts at MgO thickness of 0.85 nm, 0.75 nm and 0.70 nm, respectively, (C) The NC position value index for Sample B.

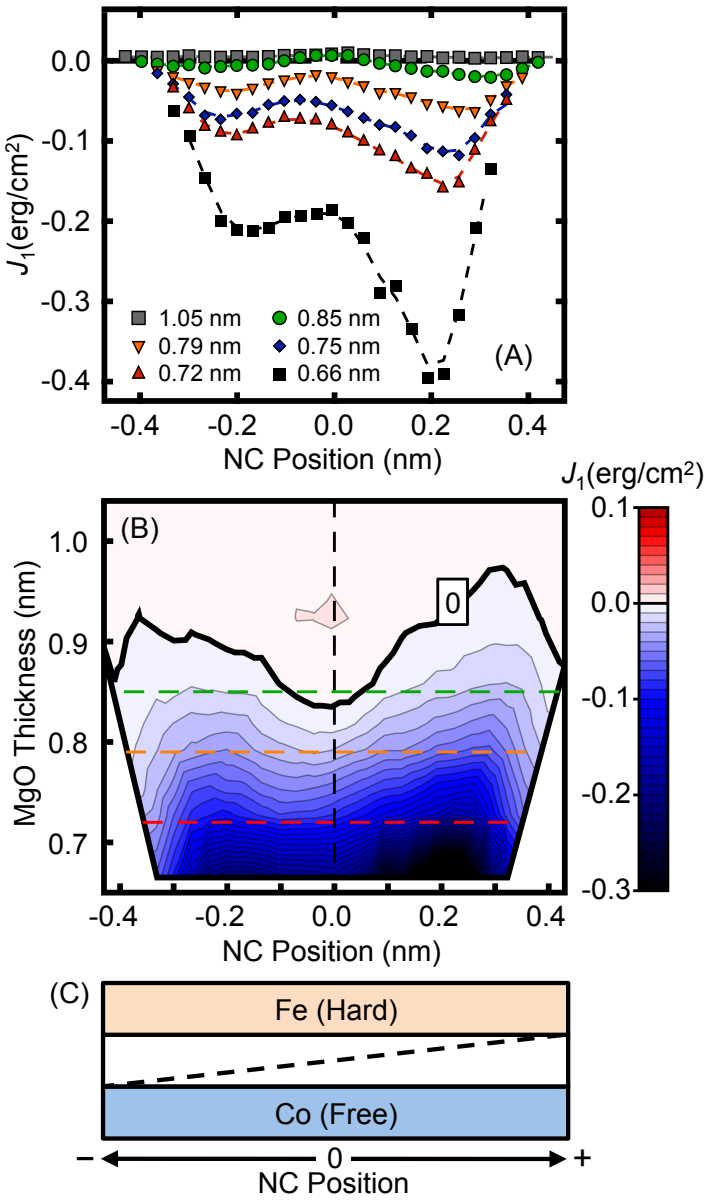

Figure 4.5: Bilinear coupling in Sample C: Fe/MgO/Co with Fe NC. (A) J_1 as a function of the NC position at MgO thicknesses of 1.05 nm (grey squares), 0.85 nm (green circles), 0.79 nm (orange triangles), 0.75 nm (blue diamonds), 0.72 nm (red triangles), and 0.66 nm (black squares). (B) Contour/color plot of J_1 with red for FM regions, blue for AF regions, and thick black line for the J_1 = 0 erg/cm^2 contour. Green, orange, and red dashed lines correspond to line cuts at MgO thickness of 0.85 nm, 0.79 nm and 0.72 nm, respectively, (C) The NC position value index for Sample C.

Next, we examine the coupling in the Fe/MgO/Co system with Fe NC embedded in the MgO spacer (denoted as sample C). Figures 4.5(A) and 4.5(B) are the representative line cuts and contour plot, respectively, for sample C and Fig. 4.5(C) is the NC position index. In Fig. 4.5(A), we again see the W-shape trend in J_1 with respect to NC position, but there is a strong asymmetry in the AF coupling strength. Examining the line cut at MgO thickness of 0.72 nm (red or dark gray triangles)and starting from the negative end point where the NC are at the MgO/Co interface, we find $J_1 = -0.03$ erg/cm^2. As the NC move vertically toward the zero NC position, we find a maximum AF coupling of $J_1 = -0.10$ erg/cm^2 at a Fe NC position of -0.20 nm. As the NC continue to move, the coupling reaches a minimum AF coupling of $J_1 = -0.07$ erg/cm^2 at a Fe NC position of -0.08 nm. With the NC continuing to move towards the hard layer, J_1 reaches another AF maximum of -0.16 erg/cm^2 at a Fe NC position of $+0.22$ nm. Once the NC merge with the Fe at hard layer (positive end point), the AF coupling decreases to $J_1 = -0.05$ erg/cm^2. The asymmetry in AF coupling is very prominent for MgO thickness of 0.66 nm (black squares) where $J_1 = -0.40$ erg/cm^2 at NC position of $+0.19$ nm and $J_1 = -0.21$ erg/cm^2 at NC position of -0.20 nm. Figure 4.5(B) is the resulting J_1 contour plot for sample C. At high MgO thickness, we do not observe a prominent ferromagnetic peak, as was observed for sample B [Fig. 4.4(B)]. Further, the asymmetry in the AF coupling can be clearly seen from differences in J_1 (color intensity) and the asymmetry in shape of the contour lines about the zero position line (vertical dashed line).

4.4 Analysis and Discussion

4.4.1 Model for coupling for FM/MgO/FM with NC

To gain an insight into the origin of the features seen in samples B and C, we develop a model for the coupling based on additional experimental observations. First, we establish that the magnetic property of the Fe NC is the most important as opposed to the electronic property for the effects seen in the coupling. This is supported by measurements of samples with nonmagnetic NC Ag and Al, where it is found that the W-shape feature in the line cuts of J_1 vs NC position are lost. Thus, we assume the simplest magnetic coupling, which is just pairwise bilinear coupling among the magnetic elements: the coupling between the free and hard layer $J_{Hard\text{-}Free}$, the coupling between the free layer and NC $J_{Free\text{-}NC}$, and the coupling between the hard layer and NC $J_{Hard\text{-}NC}$ as shown in Fig. 4.6A. Second, coupling in samples with Fe NC showed little temperature dependence and no presence of biquadratic coupling.[1] Therefore, we ignore the effect of thermal fluctuations and assume that the system is at a minimum energy. Based on these assumptions, the total bilinear coupling between the hard and free layers is (see Appendix)

$$J_1(t_1,t_2) = J_{Hard\text{-}Free}(t) + \frac{|J_{Free\text{-}NC}(t_1) + J_{Hard\text{-}NC}(t_2)| - |J_{Free\text{-}NC}(t_1) - J_{Hard\text{-}NC}(t_2)|}{2} \quad (4.1)$$

where t is the total MgO spacer thickness, t_1 (t_2) is the MgO thickness between the free (hard) layer and NC $t = t_1 + t_2$. The first term represents the direct coupling, while the second term represents the effect of coupling to the Fe NC.

To see if this model has the same qualitative features as the data, namely, the symmetric W-shape for Fe/MgO/Fe and the asymmetric W-shape for Fe/MgO/Co, we assume a functional form for the NC-FM layer coupling that is similar to $J_{Hard\text{-}Free}$. Figure 4.6B shows the assumed form of the coupling, $j(t)$, as a function of thickness, which is based on a double exponential fit of the Fe/MgO/Fe data in sample A and the fact that the coupling is ferromagnetic at low thickness. Including a strength scaling factor, A, we have

$$J_{Free\text{-}NC}(t_1) = A_{Free\text{-}NC} j(t_1) \tag{4.2}$$

$$J_{Hard\text{-}NC}(t_1) = A_{Hard\text{-}NC} j(t_1) \tag{4.3}$$

In Fig. 4.6C, J_1 is plotted as a function of NC position with t= 0.7 nm and coupling strengths for FM layer to NC are set to be equal for the free and hard layer ($A_{Hard\text{-}NC} = A_{Free\text{-}NC} = 0.08$). Comparing the simulation [Fig. 4.6(C)] to the line cut at MgO thickness of 0.7 nm in sample B [Fig. 4.6(D)], the model qualitatively reproduces the characteristic W-shape trends observed for the sample B line cut. The model provides an intuitive explanation for the shift toward ferromagnetic coupling when the magnetic NC is near the center of the MgO spacer. Because both the free and hard layers couple antiferromagnetically to the NC,

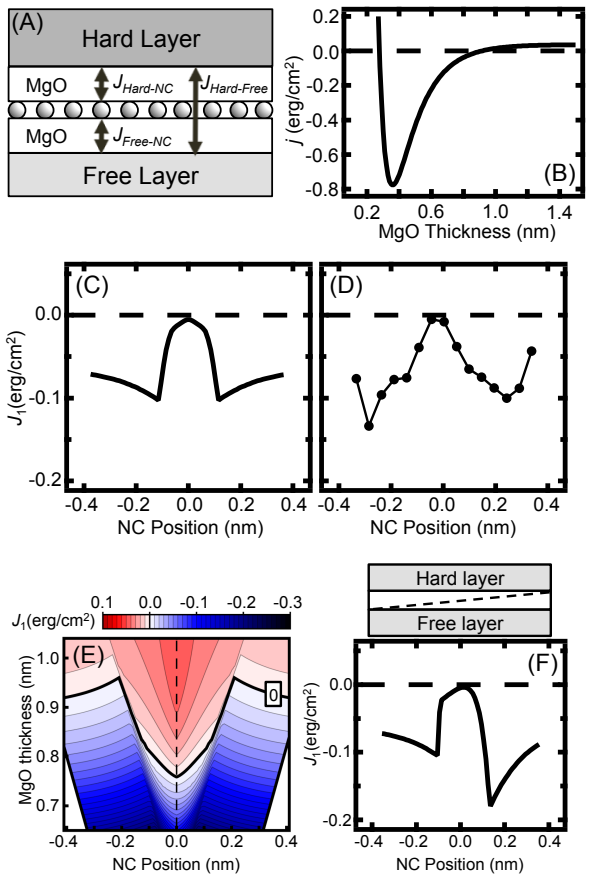

Figure 4.6: (A) Schematic of the pair-wise coupling model, (B) Plot of the $j(t)$ function used in the simulation. (C) Simulated line cut for MgO thickness of 0.70 nm, (D) line cut data for Sample B at t = 0.70 nm. (E) Simulated J_1 contour plot, (F) Simulated line cut for $A_{Free\text{-}NC} = 0.28$ and $A_{Hard\text{-}NC} = 0.08$.

the cumulative effect is that the magnetizations of the two layers want to be parallel to each other. To further test the model, we calculate a J_1 contour plot using Eqs. (4.1)-(4.3) [Fig 4.6(E)] and compare to the J_1 contour plot of sample B [Fig. 4.4(B)], showing again that the pairwise coupling model can capture the features seen in our samples.

Next, we try to produce the asymmetry in the line cuts that were seen in sample C [Fig. 4.5A]. Figure 4.6(F) shows a simulated line cut for highly asymmetric coupling strength using t= 0.7 nm, $A_{Hard\text{-}NC} = 0.08$, and $A_{Free\text{-}NC} = 0.28$. This shows a strong asymmetry in the line cut that is similar to the data of sample C. Because the AF coupling is stronger at the positive NC position in both the data and simulation, it implies that the coupling between the Fe NC and Co free layer is much stronger than the coupling between the Fe NC and Fe hard layer. Therefore, by assuming a reasonable functional form for $J_{Free\text{-}NC}$ and $J_{Hard\text{-}NC}$ Eqs.4.2 and 4.3, the model defined by Eq.4.1 is able to capture the main features of the experimental data.

4.4.2 Coupling to Fe nanoclusters

We now turn our attention to using Eq.4.1 to quantitatively determine the values for $J_{Free\text{-}NC}$ and $J_{Hard\text{-}NC}$. To do this, we no longer assume the functional forms of Eqs.4.2 and 4.3. The only assumption we make is that when the NC is very close to a FM layer, its coupling will be very strongly ferromagnetic so their magnetizations will be aligned. For the case when the NC is very close to the hard layer, then Eq.4.1 reduces to

$$J_1 \approx J_{Hard\text{-}Free} + J_{Free\text{-}NC} \tag{4.4}$$

For the case when the NC is very close to the free layer, then Eq. 4.1 reduces to

$$J_1 \approx J_{Hard\text{-}Free} + J_{Hard\text{-}NC} \tag{4.5}$$

In either case, the total coupling is the sum of the coupling between the hard and free layer $J_{Hard\text{-}Free}$ and the coupling between the NC and the distant FM layer.

In order to isolate the coupling between the NC and the FM layer, it is therefore necessary to determine the value of $J_{Hard\text{-}Free}$. Fortunately, this is possible for the case when the Fe NC is near a Fe layer. When the Fe NC is located directly at the Fe layer, the NC merges with the Fe layer and the NC ceases to exist as a separate entity. In this limit, the total coupling is just given by $J_{Hard\text{-}Free}$. Thus, the value of J_1 at the end point of the line cut is $J_{Hard\text{-}Free}$, and the variation in J_1 away from the end point is equal to the coupling between the NC and the distant FM layer.

For sample C, this applies to the case when the NC is close to the Fe hard layer, yielding values for the coupling between the NC and Co layer.

Figure 4.7 shows a line cut at total MgO thickness of t= 0.66 nm. The value of J_1 at a standardized distance of 0.1 nm between the NC and Fe layer yields a value of $J_{\text{Co-NC}}$=−0.26 erg/cm^2 as illustrated in the figure. This procedure is repeated for each line cut in Fig. 4.5A

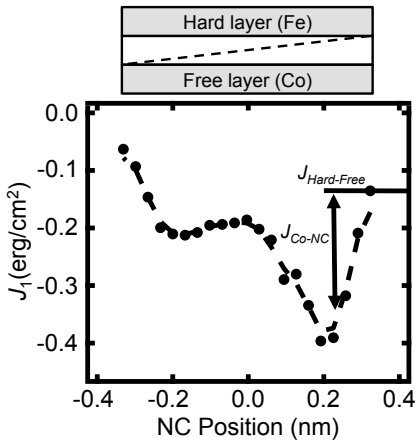

Figure 4.7: The method for determining the values of $J_{Hard\text{-}Free}$ (horizontal line) and $J_{FM\text{-}NC}$ (vertical line), the coupling between the Fe NC and FM layer in line cut data for Sample C at $t = 0.66$ nm. The dashed line is a guide for the eye.

to obtain the values of $J_{\text{Co-NC}}$ as a function of MgO spacing and the results are plotted in Fig. 4.8A solid circles.

For sample B, this procedure is performed for each Fe layer, yielding two data sets for the coupling between the NC and Fe layer $J_{\text{Fe-NC}}$ as a function of distance. Figure 4.8A shows the results for the $\text{Fe}_{\text{hard-NC}}$ coupling open circles and the $\text{Fe}_{\text{free-NC}}$ coupling open squares. For comparison with layer-to-layer coupling, in Fig. 4.8B we plot the coupling in Fe/MgO/Fe and Fe/MgO/Co without NC over the matching MgO thickness range.

Comparing Figs. 4.8A and 4.8B, we see that the $J_{\text{Co-NC}}$ is always more AF than $J_{\text{Fe-NC}}$, unlike the trend seen for $J_{\text{Fe-Co}}$ and $J_{\text{Fe-Fe}}$. For the coupling of two thin films Fig. 4.8B, we see that $J_{\text{Fe-Fe}}$ is slightly more AF than $J_{\text{Co-Fe}}$ for MgO thicknesses above 0.65 nm, while the AF coupling of $J_{\text{Co-Fe}}$ is clearly stronger than $J_{\text{Fe-Fe}}$ for MgO thickness below 0.65 nm. At MgO thickness of $\sim$0.56 nm, $-J_{\text{Co-Fe}} \approx 0.37$ erg/cm^2 and $-J_{\text{Fe-Fe}} \approx 0.31$ erg/cm^2, which has a difference of 0.06 erg/cm^2, or $\sim$20%. For the coupling between thin film to NC Fig.

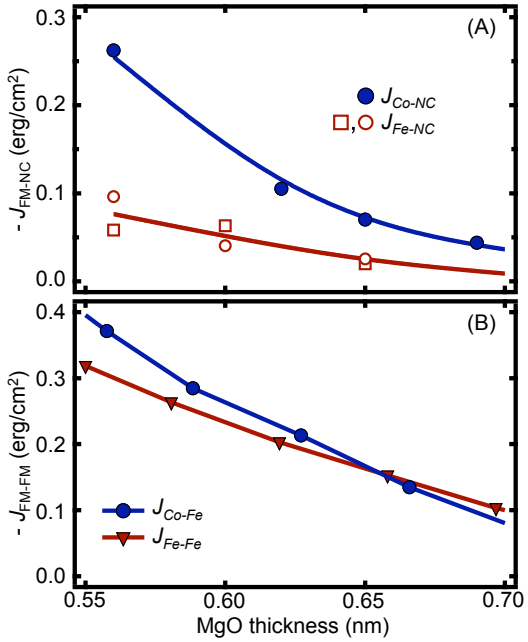

Figure 4.8: (A) $-J_{FM\text{-}NC}$ as a function of MgO thickness. Blue circles are for Co/MgO/NC, open red circles are for Fe(hard)/MgO/NC, and open red squares are for Fe(free)/MgO/NC. (B) Coupling observed in Fe/MgO/Co (blue circles) and Fe/MgO/Fe (red triangles) in Sample A.

4.8A, $J_{\text{Co-NC}}$ always has stronger AF coupling than $J_{\text{Fe-NC}}$ and at MgO thickness of 0.56 nm, $-J_{\text{Co-NC}}$= 0.26 erg/cm^2 and $-J_{\text{Fe-NC}}$= 0.10 erg/cm^2, which has a difference of 0.16 erg/cm^2, or $\sim$160%. This is much larger than the difference between $J_{\text{Co-Fe}}$ and $J_{\text{Fe-Fe}}$, both in terms of percentage difference and in absolute magnitude.

Qualitatively, the magnitude of coupling and coupling differences should scale with the area of the FM/MgO interface, which is smaller for a layer of NC than a continuous film. Although the magnitude of the coupling does decrease in the NC systems, the decrease is not nearly as much as one would expect based on the reduced area of the 1/4 ML Fe NC. Interestingly, we find that the difference in the coupling between Fe/MgO/Fe and Fe/MgO/Co

systems is amplified when the Fe is reduced from a thin film to a NC layer. Further studies will be needed to understand the microscopic origin of this nanoscaling effect.

4.5 Conclusion

We measured the interlayer exchange coupling across the Fe/MgO/Fe and Fe/MgO/Co systems with and without embedded Fe nanoclusters. First, we find that changing the material composition of the free layer from Fe to Co/Fe enhances the coupling across MgO. Next, by embedding Fe NC at different positions within the MgO spacer in both Fe/MgO/Fe and Fe/MgO/Co systems, we can tailor the strength and sign of J_1. Through developing a pairwise coupling model, we show that the observed effects are due to the magnetic coupling between the FM layers and NC. Lastly, we compare differences in coupling observed in the thin-film/NC systems (Co/MgO/NC and Fe/MgO/NC) to the analogous thin-film systems (Fe/MgO/Co and Fe/MgO/Fe) and find that the coupling difference is greater in the NC systems, providing evidence for enhanced material dependence in J_1 due to nanoscaling effects.

References

[1] J. Slonczewski, Journal of applied physics **73**, 5957 (1993).

[24] Y. F. Chiang, J. J. I. Wong, X. Tan, Y. Li, K. Pi, W. H. Wang, H. W. K. Tom, and R. K. Kawakami, Phys. Rev. B **79**, 184410.

[44] S. Yuasa, T. Nagahama, A. Fukushima, Y. Suzuki, and K. Ando, Nature materials **3**, 868 (2004).

[45] S. Yuasa, A. Fukushima, H. Kubota, Y. Suzuki, and K. Ando, Applied Physics Letters **89**, 042505 (2006).

[50] M. Y. Zhuravlev, E. Y. Tsymbal, and A. V. Vedyayev, Phys. Rev. Lett. **94**, 026806 (2005).

[54] C. Tusche, H. L. Meyerheim, N. Jedrecy, G. Renaud, and J. Kirschner, Phys. Rev. B **74**, 195422 (2006).

[55] J. Faure-Vincent, C. Tiusan, C. Bellouard, E. Popova, M. Hehn, F. Montaigne, and A. Schuhl, Phys. Rev. Lett. **89**, 107206 (2002).

[56] T. Katayama, S. Yuasa, J. Velev, M. Zhuravlev, S. Jaswal, and E. Tsymbal, Evgeny Tsymbal Publications, 3 (2006).

[60] C. Tiusan, M. Sicot, J. Faure-Vincent, M. Hehn, C. Bellouard, F. Montaigne, S. Andrieu, and A. Schuhl, Journal of Physics: Condensed Matter **18**, 941 (2006).

[67] A. Milner, A. Gerber, B. Groisman, M. Karpovsky, and A. Gladkikh, Phys. Rev. Lett. **76**, 475 (1996).

[68] A. Tomou, L. Panagiotopoulos, D. Gournis, and B. Kooi, J. Appl. Phys. **102**, 023910 (2007).

[69] S. Mitani, S. Takahashi, K. Takanashi, K. Yakushiji, S. Maekawa, and H. Fujimori, Phys. Rev. Lett. **81**, 2799 (1998).

[70] C Binns, M. J. Maher, Q. A. Pankhurst, D. Kechrakos, and K. N. Trohidou, Phys. Rev. B **66**, 184413 (2002).

[71] Z. Mao, Z. He, D. Chen, W. Y. Cheung, and S. P. Wong, Solid State Communications **142**, 329 (2007).

[72] S. Takahashi and S. Maekawa, Phys. Rev. Lett. **80**, 1758 (1998).

[73] H. Yang, S.-H. Yang, and S. S. P. Parkin, Nano Lett. **8**, 340 (2008).

[74] Y. Wang, X. F. Han, and X.-G. Zhang, Appl. Phys. Lett. **93**, 172501 (2008).

[75] H. Sukegawa, S. Nakamura, A. Hirohata, N. Tezuka, and K. Inomata, Phys. Rev. Lett. **94**, 068304 (2005).

[76] E Popova, N Keller, F Gendron, C Tiusan, A Schuhl, and N. A. Lesnik, Appl. Phys. Lett. **91**, 112504 (2007).

[77] H.-C. Wu, S. K. Arora, O. N. Mryasov, and I. V. Shvets, Appl. Phys. Lett. **92**, 182502 (2008).

[78] M. Y. Zhuravlev, J. Velev, A. V. Vedyayev, and E. Y. Tsymbal, J. Magn. Magn. Mater. **300**, e277 (2006).

[79] H. Li and B. P. Tonner, Phys. Rev. B **40**, 10241 (1989).

[80] S. Yuasa, T. Katayama, T. Nagahama, A. Fukushima, H. Kubota, Y. Suzuki, and K. Ando, Appl. Phys. Lett. **87**, 222508 (2005).

[81] M. Klaua, D. Ullmann, J. Barthel, W. Wulfhekel, J. Krischner, R. Urban, T. L. Monchesky, A Enders, J. F. Cochran, and B. Heinrich, Phys. Rev. B **64**, 134411 (2001).

[82] W. Wulfhekel, M. Klaua, D. Ullmann, F. Zavaliche, J. Krischner, R. Urban, T. L. Monchesky, and B. Heinrich, Appl. Phys. Lett. **78**, 509 (2001).

[83] G. Fahsold, A Pucci, and K.-H. Rieder, Phys. Rev. B **61**, 8475 (2000).

[84] R. K. Kawakami, E. Rotenberg, H. J. Choi, E. J. Escorcia-Aparicio, M. O. Bowen, J. H. Wolfe, E. Arenholz, Z. D. Zhang, N. V. Smith, and Z. Q. Qiu, Nature **398**, 132 (1999).

[85] R. K. Kawakami, E. Rotenberg, E. J. Escorcia-Aparicio, H. J. Choi, T. R. Cummins, J. G. Tobin, N. V. Smith, and Z. Q. Qiu, Phys. Rev. Lett. **80**, 1754 (1998).

Chapter 5

TiO_2 as an Electrostatic Template for Epitaxial Growth of EuO on MgO(001)

5.1 Background

The spin filter effect,[86] possible use as a magnetic gate dielectric, [87, 88] and a large magneto-optic response,[89] makes stoichiometric EuO, a ferromagnetic insulator, promising for spin-based applications.[90] Also of great interest are doped and nonstoichiometric EuO due to their demonstration of a metal-insulator transition,[91] colossal magnetoresistance,[92] half metallic behavior,[93] and the anomalous Hall effect.[94] The recent resurgence of interest in EuO is largely due to the advances in synthesis of high quality EuO films by reactive molecular beam epitaxy (MBE).[88, 95–97] More specifically, the stoichiometric growths have been reliably achieved only within an adsorption-controlled growth

regime.[95, 96] Two separate conditions determine this regime. First, the substrate is maintained at an elevated temperature, which allows for Eu re-evaporation (distillation) from the substrate. Second, a carefully maintained oxygen partial pressure determines the growth rate and chemical composition (Eu_xO_y).

MgO is an important oxide for spintronics due to its $\Delta 1$ band spin filtering in magnetic tunnel junctions[43–45] and its effective use as a tunnel barrier for spin injection into semiconductors and graphene.[98–101] Also, MgO has long served as a popular commercially available substrate for the deposition of a wide variety of materials such as transition metals, perovskites, and spinels.[44, 102, 103] Several authors have reported successful deposition of EuO on MgO[97, 104] and cube-on-cube growth with a magnetization of 7 Bohr magnetons per Eu atom despite the large lattice mismatch of $\sim$22% (($a_{EuO} - a_{MgO}$) / a_{MgO} = (0.514 nm$-$0.421 nm) / 0.421 nm = 22.1%).[88] However, while single crystal deposition on MgO(001) is possible, the initial stages of the growth have yet to be fully investigated and require further exploration.[97, 105]

Here, I present the results of high quality EuO epitaxy on MgO by the introduction of a TiO_2 interfacial layer. Conceptual electrostatic arguments are introduced to explain why TiO_2 alleviates many of the problems associated with rock salt heteroepitaxy. Time evolution of the growths are compared and the TiO_2 surface is shown to produce single crystal EuO in the monolayer regime by inducing a 45° in plane rotation, which decreases the lattice mismatch, and by serving as an electrostatic template for which like-ion repulsion is alleviated. On the other hand, direct epitaxy of EuO on MgO is shown to be of reasonable quality only after

2 nm. Interestingly, ultrathin EuO can be produced without the introduction of oxygen partial pressure through substrate-supplied oxidation to yield films in the monolayer regime. Such ultrathin films are ferromagnetic with bulk Curie temperatures.

5.2 Experimental Procedures

In this study, 10 mm x 10 mm x 0.5 mm double-side polished MgO(001) substrates are first rinsed in DI water, then loaded into a MBE system with a base pressure $\sim 1 \times 10^{-10}$ torr. The crystal surface quality of the sample is monitored throughout the annealing and subsequent layer growths with *in situ* reflection high energy electron diffraction (RHEED). The substrate is annealed for 60 minutes at 600°C as measured by a thermocouple located near the sample. The substrate is then cooled to 350°C for the deposition of a 10 nm MgO buffer layer grown by e-beam evaporation at a typical rate of $\sim$1 Å/min.[106] The MgO buffer layer smoothes the substrates surface, indicated in the RHEED pattern as sharpened streaks and Kikuchi lines (Fig 5.2(A) and 5.2(B)). To create the TiO_2 layer, Ti is first deposited from an e-beam source onto the MgO buffer layer at room temperature (RT). The Ti thickness is chosen according to the number of desired surface Ti atoms corresponding to 1, 1.5, or 2 monolayers of lattice matched 2×2 reconstructed TiO (chemical composition TiO_2) as described more fully in the following section. The Ti layer is exposed to molecular oxygen (5×10^{-8}) at 500°C for 30 minutes. For subsequent growths on either the TiO_2 or directly on the MgO buffer layer, EuO films are produced by reactive MBE where a high purity metal

source is sublimed and allowed to react with a molecular oxygen partial pressure. Typical stoichiometric growth in the adsorption-controlled (distillation and oxygen-limited) regime proceeds as follows. 99.99% pure Eu metal is evaporated from a thermal effusion cell and the flux ($\sim$8 Å/min) is incident upon the heated substrate which is maintained at 500°C. Next, molecular oxygen is leaked into the chamber with a partial pressure of 1×10^{-8} torr enabling the growth of stoichiometric EuO.[88, 96, 97] Such films on bare MgO have been shown to be approximately 5 nm thick for a 30minute growth time by AFM profiling giving a growth rate of 0.17 nm/min.[88]

5.3 Growth and Electrostatics at the EuO/MgO(001) Interface

Heteroepitaxy between insulating oxides, such as of large cation oxides on MgO, is greatly determined by interface electrostatics.[102] Purely structural considerations are insufficient to fully understand the EuO/MgO interface. The cube-on-cube (EuO(001)[100] // MgO(001)[100]) growth on MgO[88, 97] suggests that some structural arrangement (i.e. either 1:1, 3:4, 4:5, etc) is favored. A 3:4 spacing has a reduced lattice mismatch of 8.4% and a 4:5 spacing has a mismatch of 2.3%. For a clearer picture, a 4:5 (EuO:MgO) stacking, displayed using VESTA software,[107] is shown in Figure 5.1(A). An examination of the 4:5 stacking shows that while the center Eu^{2+} ion has a favorable position above an O^{2-} ion, at the left edge, the first Eu^{2+} ion is sitting above an Mg^{2+} ion and the first O^{2-} ion is above another O^{2-} ion.

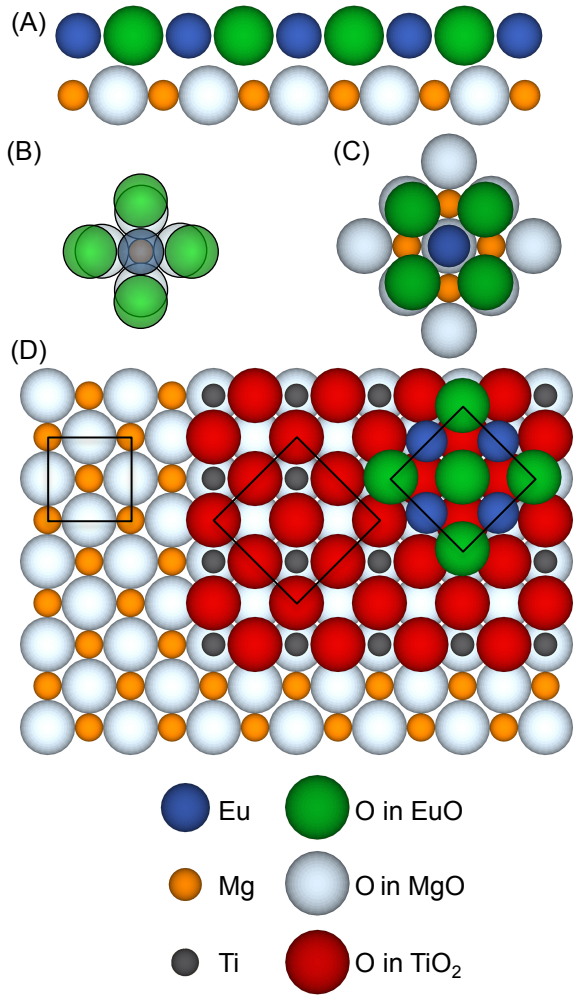

Figure 5.1: Various Crystal Structure Schematics of EuO on MgO. (A) Schematic of cube-on-cube EuO/MgO(001) in a 4:5 (EuO:MgO) configuration at the interface. Ions are represented as follows: the Mg ions are shown as small spheres (orange), the O in MgO ions are large white spheres, Eu ions are the medium spheres (blue) and O in EuO are the large dark spheres (green). (B) Shows the ion size effect for cube-on-cube growth of EuO (transparent over layer) on MgO (under layer). (C) Configuration for a 45 rotated EuO over layer on MgO demonstrating the anion-anion overlap between the oxygen ions of the EuO and MgO. (D) Structure of the EuO/TiO_2/MgO layers. Ti ions are the smallest gray spheres and O ions in TiO_2 are the large gray spheres (red). Boxes show the unit cells for each oxide. For (A) - (D), the ions in each schematic are sized according to their ionic radius. The MgO and TiO_2 are drawn to scale with the bulk MgO lattice parameter while all EuO layers correspond to the bulk EuO lattice constant.

This is repeated at the right edge of the 4:5 configuration. From an electrostatic point of view, strong Coulomb repulsion between like ions suggests that such a stacking is not ideal despite the improved lattice match and would certainly lead to surface roughening at the interface. Another concern for the cube-on-cube growth mode for direct heteroepitaxy is the ion-size difference effect,[102] which is related to the difference in size between the Mg-O bond and the Eu-O bond. The Mg^{2+} ionic diameter, 0.130 nm, combined with two Oxygen (O^{2-}) ionic radii of 0.140 nm, forms a nearly close- packed system with the ions spanning 97% of the lattice constant.[108] Figure 5.1(B) illustrates that replacing the Mg^{2+} ion with a Eu^{2+} ion changes the cation ionic diameter to 0.234 nm and increases the O-O nearest neighbor bond by 22% from 0.298 nm to 0.363 nm. Effectively, the deposition of an atomically flat EuO layer on a pristine MgO(001) surface is equivalent to 100% substitutional doping the Mg atoms in the top layer of an MgO surface with Eu atoms. In such a case, the ion-size difference would force the Eu or O atoms to find equilibrium positions in a roughened structure.

Alternatively, another possible structural alignment would be a 45° in-plane rotation of the EuO lattice relative to the underlying MgO orientation. Figure 5.1(C) shows a 45° rotated EuO layer on an MgO underlayer with the placement of a Eu ion on an oxygen bonding site. Such a configuration would remove the ion-size effect ($a_{EuO} / 2 = 2.57 < a_{MgO} / \sqrt{2} = 2.91$), reduce the lattice mismatch to 12% and could potentially improve the growth mode. However, anion-anion or cation-cation electrostatics makes the structure energetically unfavorable because the oxygen ions in the EuO overlayer sit atop oxygen ions in the underlying MgO

surface. With these considerations in mind, any attempt to engineer the interface to minimize the electrostatic repulsion of like ions, while simultaneously maintaining an atomically smooth surface, could greatly improve the epitaxy.

To alleviate the interfacial electrostatic repulsion and stabilize EuO epitaxy on MgO(001), we propose a special TiO_2 template at the interface. Such an approach has been employed to produce high quality epitaxy of $BaTiO_3$ films on MgO(001).[102] Figure 5.1(D) shows the stacking for subsequent depositions of a TiO_2 layer followed by EuO on MgO(001). Starting from left to right in Figure 5.1(D) is the MgO buffer layer, followed by a monolayer of TiO_2, and lastly, a single unit cell of EuO is shown rotated 45° relative to the MgO in-plane orientation. The displayed MgO lattice spacing is that of bulk MgO and the TiO_2 layer is shown lattice matched to the MgO. The EuO is shown with bulk EuO lattice constant. For the single monolayer of TiO_2, O atoms are positioned above Mg atoms. The Ti atoms and vacancy positions are located above the O atoms of the MgO layer. This configuration allows for the subsequent EuO layer to be positioned such that the Eu atoms are located above the vacant positions in the TiO_2 layer, while the O atoms are located above the Ti atoms. Within this EuO/TiO_2/MgO(001) interface, all nearest neighbor ions have opposite charge to produce attractive Coulomb forces for an energetically stable interface. Specifically, there are no O-O or Eu-cation nearest neighbor bonds. Thus, the TiO_2 interfacial layer eliminates the ion-size effect and electrostatic problems described for the growth of EuO directly onto MgO(001).

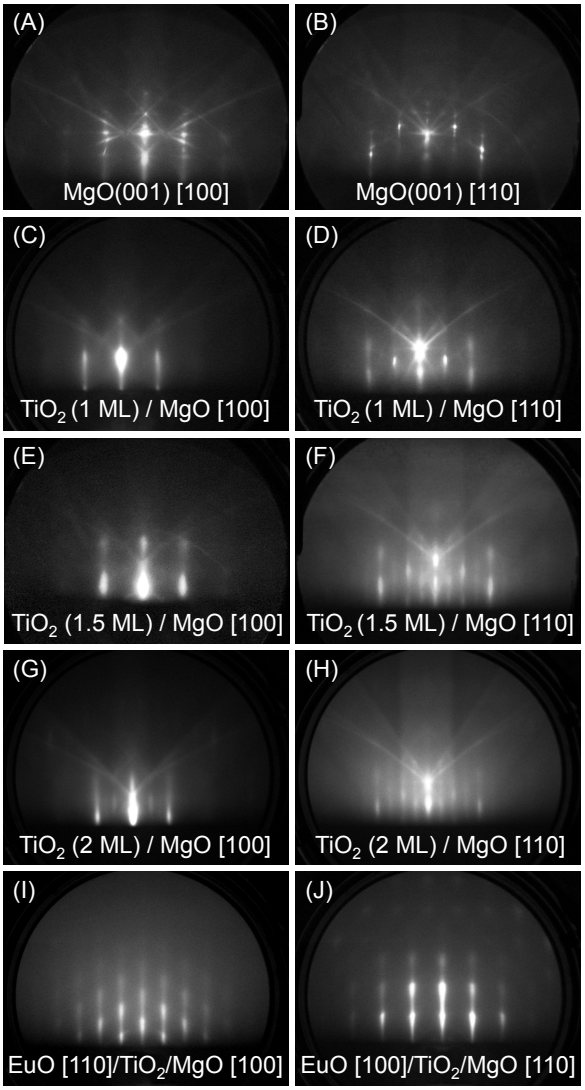

Figure 5.2: RHEED patterns for the 10nm MgO buffer layer in the (A) MgO(001)[100] and (B) MgO(001)[110] directions. (C) and (D) are the RHEED patterns for 1 ML TiO_2 monolayer on MgO(001) in the [100] and the [110] directions, respectively. (E) and (F) are the RHEED patterns for 1.5 ML TiO_2 in the [100] and the [110] directions. (G) and (H) are the RHEED patterns for 2 ML TiO_2 in the [100] and the [110] directions. Final RHEED patterns for a 5nm EuO film on TiO_2(2ML) showing (I) EuO(001)[110] // MgO(001)[100] and (J) EuO(001)[100] // MgO(001)[110].

5.4 Results and Discussion

Figure 2 shows the RHEED patterns for TiO_2 monolayers on MgO(001). Figure 5.2(A) and (B) show the 10 nm MgO/MgO(001) buffer layer pattern along the [100] and [110] directions, respectively. Figure 5.2(C), (E), and (G) are the RHEED images for oxidized Ti layers of 1, 1.5, and 2 ML along the [100] direction, while Figure 5.2(D), (F), and (H) are the corresponding TiO_2 monolayers along the [110] direction of MgO. The main features of the oxidized Ti patterns remain that of MgO with a slight broadening of the outer diffraction rods. In the RHEED image of 2 ML TiO_2/MgO(001)[100] (Figure 5.2(G)) the underlying MgO structure is readily visible with the important addition of inner streaks between the main MgO(001)[100] rods. As discussed previously, the TiO_2 layer is comprised of both Ti sites and vacant sites above the underlying oxygen atoms. Thus, the unit cell periodicity is increased to twice the size creating diffraction rods of half-spacing in the [100] direction. Equivalently, this TiO_2 layer can be perceived as a TiO rock salt surface of identical unit cell with the MgO lattice, but missing the face-centered Ti atoms.[109] This would then be a 2×2 reconstructed TiO surface producing diffraction streaks inside the MgO [100] rods. However, in no instances were inner streaks seen for the case of 1 ML oxidized Ti. Interestingly, as seen in Figure 5.2(D) and (F), inner rods appeared for 1.5 and 2 ML of oxidized Ti along the [110] direction. This suggests decreased periodicity of the 2×2 reconstructed TiO_2, possibly from an ordered stacking effect or superstructure causing increased periodicity in the k-space lattice along the [110] direction. The subsequent RHEED patterns of a 5 nm EuO film grown

on 2 ML TiO_2/MgO(001) in the adsorption-controlled regime are shown in Figures 5.2(I) and (J). These final films have an in-plane orientation of EuO(001)[110] // MgO(001)[100] and are thus 45° rotated. Importantly, as Fig 5.1(B) and Fig 5.1(D) illustrate, the ion-size effect is eliminated since the rotated EuO lattice has a smaller unit cell than the underlying TiO_2 template. While, generally, EuO growths on 1 ML TiO_2 surfaces resulted in polycrystalline films, deposition on 1.5 ML TiO_2 surfaces produced high quality EuO single crystal films of identical growth behavior and evolution to depositions on 2 ML TiO_2 (see Fig 5.3(A) and 5.3(B)). This is interesting since the 1.5 ML TiO_2 RHEED only shows part of the features seen in the 2 ML RHEED, suggesting that the 1.5 ML TiO_2 still has the critical structure of the 2×2 reconstructed TiO layer. Because of this result, and in combination with the desire to keep the TiO_2 interface as thin as possible, the 1.5 ML TiO_2 layer will be used throughout the remainder of this study.

To further examine the growth of EuO on the TiO_2 layer, the time evolution of a line cut across the RHEED pattern is monitored along the MgO(001)[110] in-plane crystal direction over the first 10 minutes of EuO growth. A line cut is obtained by plotting the intensity of the image against the CCD cameras horizontal pixel position and therefore crosses several diffraction rods. The initial line cut of 1.5 ML TiO_2 (in MgO(001)[110] direction) is shown at the top of Figure 5.3(C). After 20 seconds (dashed line (C1)), the Eu flux is introduced and immediately the RHEED begins to change. After the RHEED pattern is stabilized, oxygen is introduced into the chamber (dashed line (C2)), and the RHEED pattern changes to that of EuO(001)[100]. During this period, the RHEED quickly shifts (1 minute) to that of bulk EuO

indicating epitaxy within 1 ML with the introduction of oxygen. The final line cut (1 nm EuO) is shown below the time lapse. Analysis of the final EuO/TiO_2 line cut compared to the MgO lattice constant gives a EuO lattice parameter of 0.513 ± 0.006 nm. For comparison, the time evolution for direct deposition of EuO on the MgO buffer layer is shown in Figure 5.2(D). As indicated by dashed line (D1), elemental Eu flux is directed onto the MgO(001) substrate held at 500 °C. During this period, the RHEED pattern remains that of MgO, indicating that Eu is re-evaporating and not bonding to the surface. Once oxygen is leaked into the system (dashed line (D2)), the time evolution of the RHEED pattern consists of a fading out of the MgO(001)[110] pattern followed by a gradual recovery to a EuO(001)[110] pattern over several minutes ($\sim$2 nm). The diffraction rods increase in intensity over the subsequent 20 minutes of the growth.

Several key differences are immediately apparent between the two growths. First, comparative analysis of the diffraction pattern peak positions in the final line cuts between EuO/TiO_2/MgO and EuO/MgO demonstrates that EuO epitaxy on the TiO_2 is rotated 45-degree in-plane with respect to MgO, while the direct growth on MgO is cube-on-cube. Second, the evolution from the initial line cut to single crystal EuO takes place at a faster rate for the deposition on TiO_2/MgO and indicates fast strain relaxation for 45° rotated EuO in agreement with observations of EuO growth on Ni.[105] Third, during the distillation period, before the introduction of an oxygen partial pressure, the re-evaporation for each surface is distinctly different. While in both cases the opening of the Eu shutter decreases the RHEED intensity, on bare MgO buffer layer, the incident Eu flux re-evaporates leaving

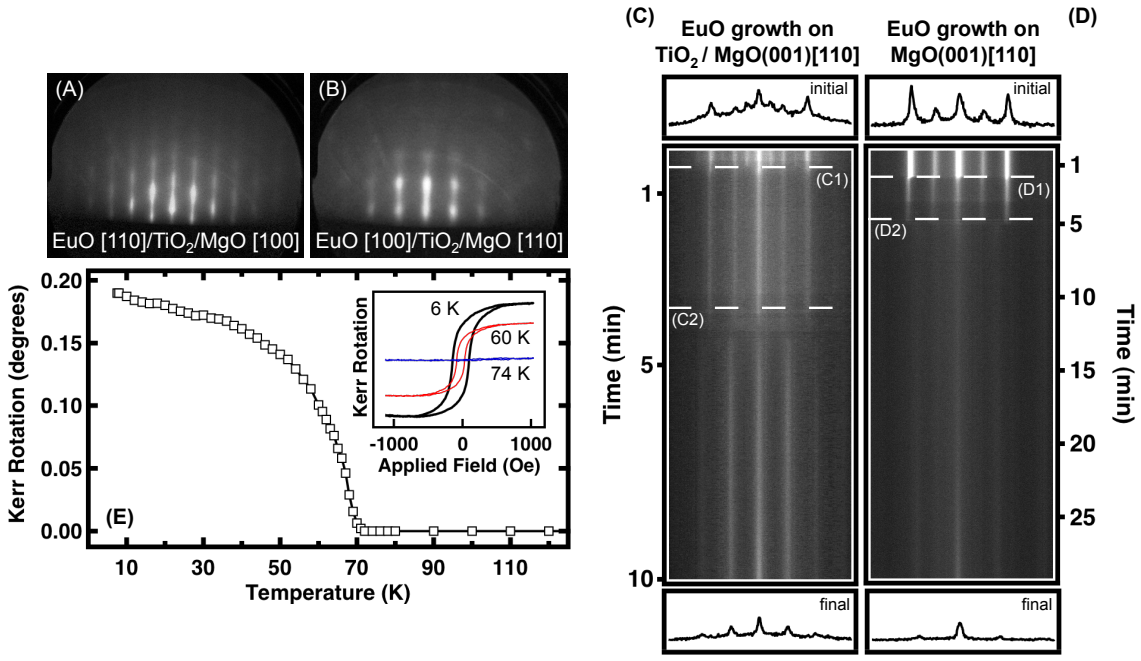

Figure 5.3: (A) and (B) are the RHEED patterns for a 5nm EuO thin film deposited on TiO_2(1.5ML)/MgO(10nm)/MgO(001) along EuO(001)[110] // MgO(001)[100] and EuO(001)[100] // MgO(001)[110], respectively. (C) is the time evolution of the initial 10 minutes EuO growth on TiO_2(1.5ML)/MgO. The initial and final line cuts are shown above and below, respectively. In (C), the peaks in the initial line cut correspond to diffraction rods seen in the 1.5 ML TiO_2 RHEED pattern (Fig. 5.2(F)), while the final line cut corresponds to the diffraction rods seen for EuO [100] // MgO [110] (Fig. 5.3(B)). (C1) (dashed line) indicates when the Eu flux is incident on the TiO_2 layer and (C2) (dashed line) indicates the introduction of O_2 into the system. (D) The time evolution of direct deposition of EuO on MgO(10nm)/MgO(001) in the MgO [110] direction and the peaks in the initial line cut shown above correspond to the diffraction rods in Fig. 5.2(B). (D1) (dashed line) indicates when the Eu flux is incident on the MgO and (D2) (dashed line) indicates the introduction of O_2. Below (D) is the final line cut of EuO after 30 minutes of growth directly on the MgO buffer layer. (E) Temperature dependence of the measured MOKE angle (degrees) taken at 0 Oe (remanence) for EuO (5nm)/TiO_2/MgO(001). Insert shows representative hysteresis loops for T = 6 K (Black), T = 60 K (Red or grey) and T = 74 K (Blue or dark grey)

the MgO(001)[110] RHEED pattern unaltered. However, on the TiO_2, the incident flux only re-evaporates after an initial time period for which the inner diffraction streaks associated with the TiO_2 are lost but the overall MgO diffraction positions in the RHEED pattern are maintained. Lack of bonding and full re-evaporation at 500 °C on bare MgO suggests, in agreement with the discussion in section 5.3, that there is some additional interfacial energy

at the EuO/MgO interface that inhibits Eu bonding. Interestingly, this is not seen for Eu deposition on either the TiO_2/MgO or YSZ12 at elevated temperatures. At this point, while the in-plane rotation, in conjunction with the TiO_2 RHEED pattern and lack of re- evaporation, would suggest that we have successfully reduced the interfacial energy at the interface by limiting electrostatic effects, one possibility that cannot be ruled out is Eu-Ti-O reactivity at the interface and that the lack of re-evaporation is due to some complex composition.

To investigate the magnetic properties of the EuO within the MgO-cap(2nm)/EuO(5nm)/TiO_2(1.5ML)/MgO(10nm)/MgO(001) structure, the magneto-optic Kerr effect (MOKE) is measured *ex situ* in an optical flow cryostat with variable temperature control. Longitudinal MOKE was measured with a p-polarized 635nm diode laser and an incident angle near 45 degrees with respect to an applied in-plane magnetic field (H). Figure 5.3(E) inset shows representative M-H hysteresis loops at T = 6 K with a coercivity (H_c) of 117 Oe and ratio (M_r/M_s) between magnetization remanence (M_r) and saturation (M_s) of 0.53. Representative loops at T = 60 K and T = 74 K are also shown. In Figure 5.3(E), M_r is plotted (in degrees) as a function of temperature. Starting at 6 K, the Kerr rotation at remanence is 0.19 degrees and decreases with increasing temperature, following typical Curie-Weiss behavior down to the transition temperature at 69 K, the bulk T_C value for EuO.

We next investigate the interfacial structure and material quality at the interface between EuO and the 1.5 ML TiO_2/MgO stacking in the following manner. 1.5 ML TiO_2 is grown on an MgO buffer layer and maintained at 500°C. Next, a Eu flux is exposed to the heated

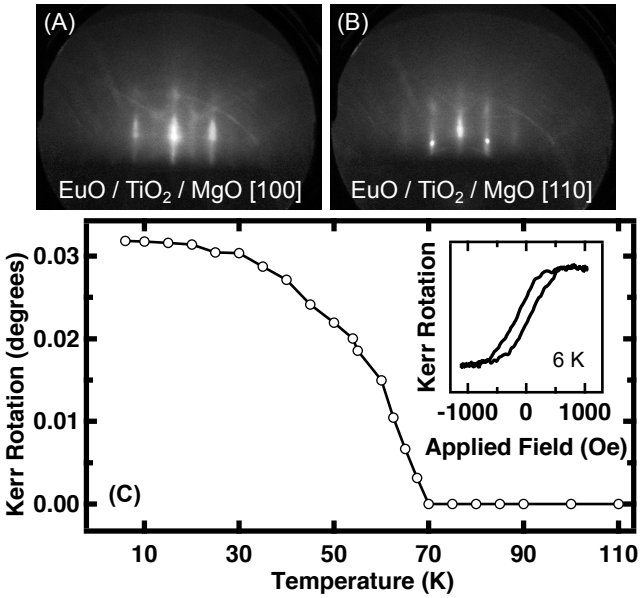

Figure 5.4: RHEED patterns for Eu deposition on the TiO_2 layer without leaking O_2 into the system in the (A) MgO(001)[100] and (B) MgO(001)[110] directions. (C) Temperature dependence of the MOKE signal measured at saturation and the insert shows a representative hysteresis loop at T = 6 K.

TiO_2 without introducing an oxygen partial pressure. Unlike the case for Eu flux incident on the bare MgO, the RHEED pattern immediately changes (Fig. 5.4(A) and 5.4(B)), indicating bonding of Eu atoms to the TiO_2 surface. Furthermore, the faint streaks between the underlying MgO(001) [100] RHEED pattern (Fig 5.4(A)) indicates layer-by-layer epitaxial growth of EuO(001)[110] // MgO(001)[100] in the ultrathin limit. As in the case of oxygen-free growth of EuO on YSZ(001),[97] the oxygen atoms are believed to be supplied by the substrate. After a few minutes, the RHEED pattern stabilizes indicating steady state re- evaporation of the incoming Eu flux and thus the growth is terminated. The short time frame and visible underlying MgO RHEED pattern suggests that at most, only a few monolayers of material are deposited.

The sample is then capped with 3nm MgO and MOKE measurements are performed as shown in Fig 5.4(C). Hysteresis loops taken at 6 K (Fig 5.4(C) inset) clearly show ferromagnetic behavior with H_c = 98 Oe and M_r/M_s = 0.24. A temperature dependence of the magnetization remanence shows the transition temperature to be 69 K, indicating that the initial growth mode for Eu flux incident on the TiO_2/MgO interface is EuO and not a reacted Eu-Ti-O compound. Interestingly, the fact that T_C is equal to the bulk value suggests that the resulting film thickness is large enough to avoid finite size effects, which should decrease T_C.[110] Furthermore, these magnetic results shed light on the initial growth mode seen in the RHEED time evolution (Fig 5.3(C)). The reconstruction streaks immediately fade once the Eu flux is incident upon the TiO_2 surface. This occurs because the TiO_2 layer minimizes the electrostatic interactions between the EuO and MgO layers and creates nucleation sites for subsequent EuO epitaxy. The ability for Eu atoms to find a favorable binding site in the 2×2 reconstructed TiO (see Fig 5.1(D)), results in the formation of EuO with oxygen supplied by the substrate.

5.5 Conclusion

In conclusion, electrostatic interactions at the interface between EuO and MgO can greatly determine the growth sequence of the EuO layer. To improve the epitaxy of EuO on MgO, a TiO_2 interfacial template was introduced and shown to alleviate like-ion repulsion and decrease the structural mismatch between EuO and MgO. Furthermore, the initial growth se-

quence is drastically different with the TiO_2 interface than on the bare MgO as demonstrated by in-plane rotation and fast strain relaxation. Also, the addition of the TiO_2 layer allows for substrate-supplied oxidation leading to ultrathin ferromagnetic EuO films. Such a template could be an avenue for combining emerging materials onto MgO such as EuTiO3 or other rock salt magnetic oxides in single crystal heterostructures

References

[43] S. Parkin, C. Kaiser, A. Panchula, P. Rice, B. Hughes, M. Samant, and S. Yang, Nature materials **3**, 862 (2004).

[44] S. Yuasa, T. Nagahama, A. Fukushima, Y. Suzuki, and K. Ando, Nature materials **3**, 868 (2004).

[45] S. Yuasa, A. Fukushima, H. Kubota, Y. Suzuki, and K. Ando, Applied Physics Letters **89**, 042505 (2006).

[86] T. S. Santos, J. S. Moodera, K. V. Raman, E. Negusse, J. Holroyd, J. Dvorak, M. Liberati, Y. U. Idzerda, and E. Arenholz, Phys. Rev. Lett. **101**, 147201 (2008).

[87] H. Haugen, D. Huertas-Hernando, and A. Brataas, Phys. Rev. B **77**, 115406 (2008).

[88] A. G. Swartz, J. Ciraldo, J. J. I. Wong, Y. Li, W. Han, T. Lin, S. Mack, J. Shi, D. D. Awschalom, and R. K. Kawakami, Appl. Phys. Lett. **97**, 112509 (2010).

[89] K. Y. Ahn and M. W. Shafer, J. Appl. Phys. **41**, 1260 (1970).

[90] S. A. Wolf, D. D. Awschalom, R. A. Buhrman, J. M. Daughton, S. von Molnar, M. L. Roukes, A. Y. Chtchelkanova, and D. M. Treger, Science **294**, 1488 (2001).

[91] M. R. Oliver, J. O. Dimmock, A. L. McWhorter, and T. B. Reed, Phys. Rev. B **5**, 1078 (1972).

[92] Y. Shapira, S. Foner, and T. B. Reed, Phys. Rev. B **8**, 2299 (1973).

[93] A. Schmehl, V. Vaithyanathan, A. Herrnberger, S. Thiel, C. Richter, M. Liberati, T. Heeg, M. Rockerath, L. F. Kourkoutis, S. Muhlbauer, P. Boni, D. A. Muller, Y. Barash, J. Schubert, Y. Idzerda, J. Mannhart, and D. G. Schlom, Nature Materials **6**, 882 (2007).

[94] T. Yamasaki, K. Ueno, A. Tsukazaki, T. Fukumura, and M. Kawasaki, Appl. Phys. Lett. **98**, 082116 (2011).

[95] H. Ott, S. J. Heise, R. Sutarto, Z. Hu, C. F. Chang, H. H. Hsieh, H.-J. Lin, C. T. Chen, and L. H. Tjeng, Phys. Rev. B **73**, 094407 (2006).

[96] R. W. Ulbricht, A. Schmehl, T. Heeg, J. Schubert, and D. G. Schlom, Appl. Phys. Lett. **93**, 102105 (2008).

[97] R. Sutarto, S. G. Altendorf, B. Coloru, M. Moretti Sala, T. Haupricht, C. F. Chang, Z. Hu, C. Schüßler-Langeheine, N. Hollmann, H. Kierspel, H. H. Hsieh, H.-J. Lin, C. T. Chen, and L. H. Tjeng, Phys. Rev. B **79**, 205318 (2009).

[98] X. Jiang, R. Wang, R. M. Shelby, R. M. Macfarlane, S. R. Bank, J. S. Harris, and S. S. P. Parkin, Phys. Rev. Lett. **94**, 056601 (2005).

[99] T. Sasaki, T. Oikawa, T. Suzuki, M. Shiraishi, Y. Suzuki, and K. Tagami, Appl. Phys. Express **2**, 053003 (2009).

[100] Y. Zhou, W. Han, L.-T. Chang, F. Xiu, M. Wang, M. Oehme, I. A. Fischer, J. Schulze, R. K. Kawakami, and K. L. Wang, Phys. Rev. B **84**, 125323 (2011).

[101] W. Han, K. Pi, K. M. McCreary, Y. Li, J. J. I. Wong, A. G. Swartz, and R. K. Kawakami, Phys. Rev. Lett. **105**, 167202 (2010).

[102] R. A. McKee, F. J. Walker, E. D. Specht, G. E. Jellisen, and L. A. Boatner, Phys. Rev. Lett. **72**, 2741 (1994).

[103] D. M. Lind, S. D. Berry, G. Chern, H. Mathias, and L. R. Testardi, Phys. Rev. B **45**, 1838 (1992).

[104] N. Iwata, G. Pindoria, T. Morishita, and K. Kohn, J. Phys. Soc. Jpn. **69**, 230 (2000).

[105] D. F. Forster, J. Klinkhammer, C. Busse, S. G. Altendorf, T. Michely, Z. Hu, Y. Y. Chin, L. H. Tjeng, J. Coraux, and D. Bourgault, Phys. Rev. B **83**, 045424 (2011).

[106] J. J. I. Wong, L. Ramirez, A. G. Swartz, A. Hoff, W. Han, Y. Li, and R. K. Kawakami, Phys. Rev. B **81**, 094406 (2010).

[107] K. Momma and F. Izumi, J. Appl. Crystallogr. **41**, 653 (2008).

[108] R. D. Shannon, Acta Crystallogr., Sect. A: Cryst. Phys. Diff., Theor. Gen. Crystallogr. **32**, 751 (1976).

[109] H. Kawanowa, D. Mori, Y. Gotohand, and R. Souda, Surf. Interface Anal. **36**, 1001 (2004).

[110] R. Rausch and W. Nolting, J. Phys.: Condens. Matter **21**, 376002 (2009).

Chapter 6

Magnetoelectric Effect in MgO/Fe/Ag system

6.1 Background

Recently, there has been much interest in the scientific and technological communities in controlling magnetism with external influences other than magnetic fields. One such avenue is through the magneto-electric effect, where magnetic properties can be tuned through applied electric fields and visa versa [28–33]. Thin films of ferromagnetic metals with thicknesses typically below a few nanometers, were recently shown to exhibit large changes in the magnetocrystalline anisotropy (MCA) under the influence of larger static electric fields[27–29, 34, 35]. In the MgO/Fe/Au system, it was shown that a larger negative electric fields (in reference to the top electrode) caused the MCA of the Fe layer to prefer an perpendicular

alignment and positive fields caused an in-plane preference[28]. Other work has shown that by utilizing an Antiferromagentic magnetoelectric material, Cr_2O_3, the exchange bias can be tuned though the application of electric fields [32]. In this study, we explore the magnetoelectric effect in the MgO/Fe/Ag system. The Fe/Ag system was chosen because it has been shown to have perpendicular magnetic anisotropy (PMA) for very thin thicknesses of Fe [111–114], but is usually only seen for *in-situ* measurements. We show here that by using an MgO cap on the Fe/Ag layers, the Fe layer maintains its PMA *ex-situ*, allowing for device fabrication for electrical gating. Also, the techniques developed here for dielectric and measurement are employed in the layer studies.

6.2 Growth of Fe/Ag system on MgO

First, in order for the perpendicular magnetic anisotropy (PMA) to to arise in the Fe/Ag system, a clean single crystal interface is needed between the Fe and Ag layers. Here, we choose to used single crystal MgO (001) substrates and grow an Ag buffer layer on top. This will provide a single crystal template for the growths and electrical isolation for the application of the electric field. In order to achieve this, the growth of a single crystal Ag buffer layer on MgO needed to be developed. Ag does not wet well on MgO and tends to have a 3D growth during the initial stages of the growth [ref]. Therefore, a 4 nm single crystal Fe seed layer is used to promote a layer by layer, epitaxial growth of the Ag material. After the growth of the MgO (10 nm) buffer layer on the MgO (001) substrate, the sample is then

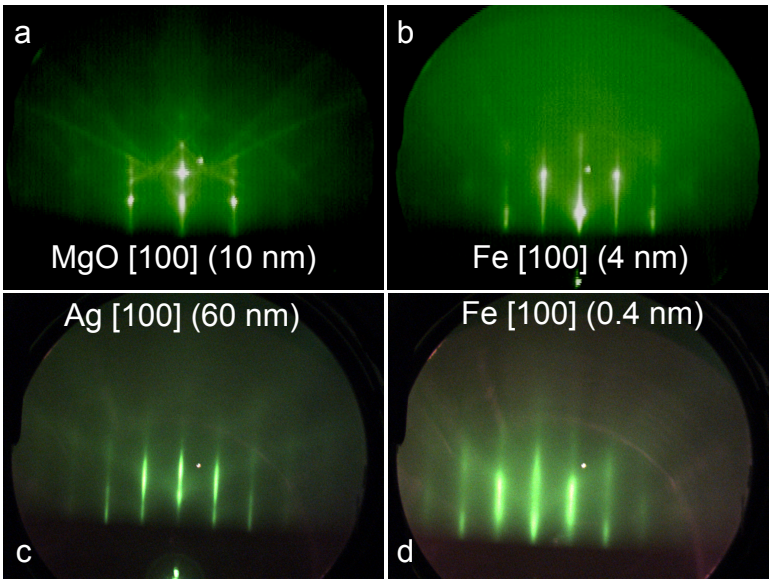

Figure 6.1: RHEED patterns for the different layer in the Fe (4 Å)/Ag (60nm)/Fe (4 nm)/MgO system. The RHEED pattern for a) MgO[100] buffer layer, b) the Fe (4 nm) seed layer, c) Ag (60 nm) buffer layer and d) 4Åof Fe on Ag buffer layer.

cooled to room temperature(RT) and the RHEED of the MgO layer is shown in 6.1a. The sample is then heated to 200°C and 4 nm of Fe is deposited followed by an 15 minute anneal at 450°C. Figure 6.1b shows the final RHEED pattern for the 4 nm of Fe seed layer. After the annealing, the sample is then cooled to RT, after which 50 nm of Ag is grown. Once the 50nm Ag layer is finished, the sample is then annealed at 250°C for 15 minutes followed by a final growth of 10 nm of Ag at 250°C. Figure 6.1c is the RHEED pattern for the single crystal Ag (60 nm) buffer and that Ag[100]//Fe[100]. The sample is cooled to RT once again and 4 monolayers (ML) of Fe (1ML = 0.143 nm) are epitaxy grown (Fig. 6.1d). Finally, the sample is capped with 10 nm of MgO inside the MBE system followed by the *ex-situ* growth of Al_2O_3 (50 nm). The series of RHEED patterns in Figure 6.1 show that a single crystal

Fe/Ag system can be grown on top of a MgO (001) substrate. Next, we explore the magnetic characteristics of the MgO/Fe/Ag layers.

6.3 Magnetic Characterization

For exploring the magnetic properties of the Fe in the MgO/Fe/Ag system, we grew an Fe wedge on the Ag buffer layer and used MOKE to measure the magnetic properties' dependence on Fe thickness (t_{Fe}). Figure 6.2a so the a schematic for the Al_2O_3 (50 nm)/MgO (10 nm)/Fe (wedge)/Ag (60 nm)/MgO(10 nm)/MgO(001) sample. The Fe wedge ranged in thickness from 0 nm to 2 nm and polar MOKE was preformed across the wedge. In figure 6.2b show representative hysteresis loops at thicknesses of 0.72 nm (black), 0.66 nm (blue) and 0.48 nm (red) with the inset showing the thickness dependence of the saturation field (H_S) and ratio between remanence / saturation magnetizations (M_R/M_S). In 6.2b, the Fe layer has a PMA for thicknesses below 0.72 nm with the PMA increasing as the thickness decreases. At a thickness of 0.48 nm, the hysteresis loop is almost square with a M_R/M_S ratio of $\sim$50%. The orange curve in 6.2b insert shows the (M_R/M_S) various thicknesses of Fe showing an increasing squareness in the hysteresis loops with decreasing thickness, indicating the increasing strength of the PMA. This is supported by the saturation field dependence of the on the Fe layer thickness (Green curve), which shows a decrease in H_S with decreasing thickness. In figure 6.3 shows the MOKE signal (blue dots) versus the Fe layer thickness. At 2 nm (not shown in graph), the Fe film prefers in-plane magnetization and as the thickness

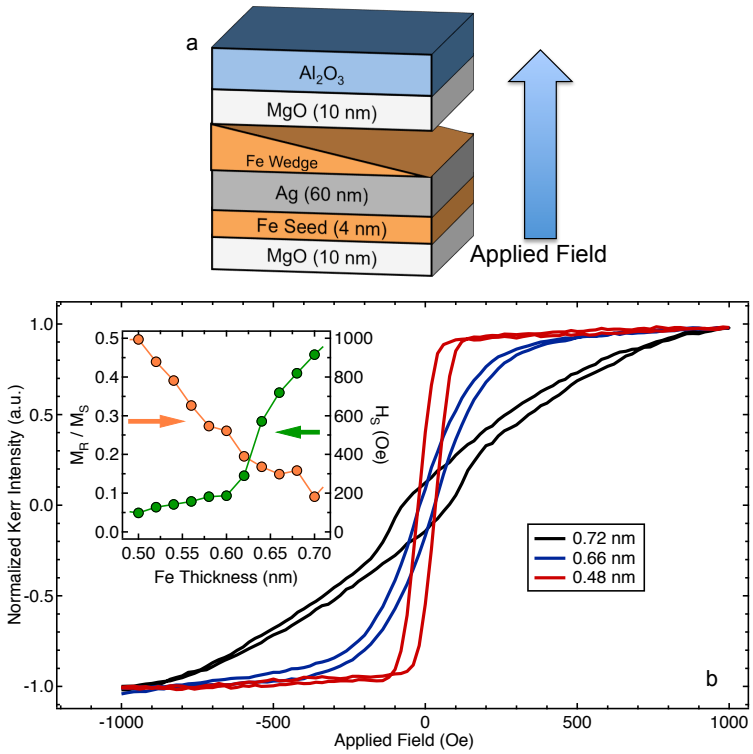

Figure 6.2: MOKE analysis of the MgO/Fe/Ag/Fe/MgO(10 nm) system on MgO(001) substrate. a) is a schematic of the sample with applied magnetic field out-of-plane. b) is the resulting MOKE loops of the Fe wedge layer at different thicknesses. The red curve is for t_{Fe} =0.48 nm, blue is for t_{Fe} =0.66 nm, and the black is t_{Fe} =0.72 nm. The left insert is the M_R/M_S ratio (orange) versus t_{Fe} and the green curve is H_S versus t_{Fe}.

decreases, the polar MOKE signal increases. Below 1 nm, the signal increases to a maximum at 0.72 nm indicating that the sample is transitioning from a preferred in-plane magnetization to a perpendicular magnetization and combined with what is shown in figure 6.2, sample's preferred magnetization direction is mostly out-of-plane but with a saturation field is near 1000 Oe. As the Fe layer continues to decreases in thickness, the MOKE signal decrease linearly as expected due the MOKE signal being proportional to the thickness (Fig 6.3 - black dashed line). However, at an t_{Fe} of $\sim$0.32 nm, the signal decrease much more rapidly and no signal is detected below $\sim$0.13 nm (Red dashed line). This sharp decrease is due because

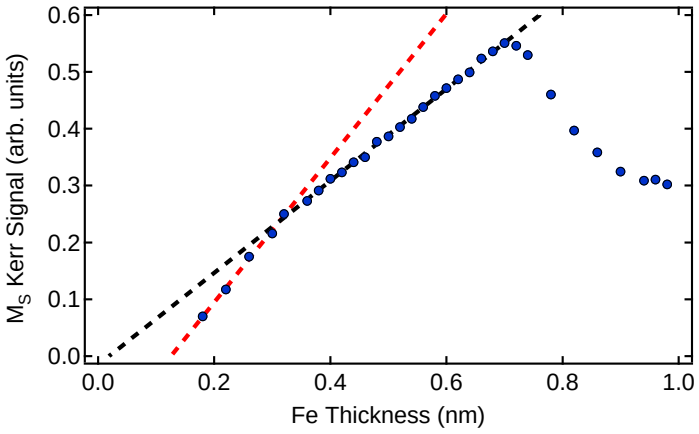

Figure 6.3: Polar MOKE signal versus Fe layer thickness. The black dash line indicated the signal decrease due to thickness once sample showed PMA and the red dashed line show the signal decrease due to changes in the T_C.

the Curie temperature (T_C) of Fe significantly decrease to below room temperature below thickness of 1.5 ML. Many samples where grown and the magnetic behavior seen in figure

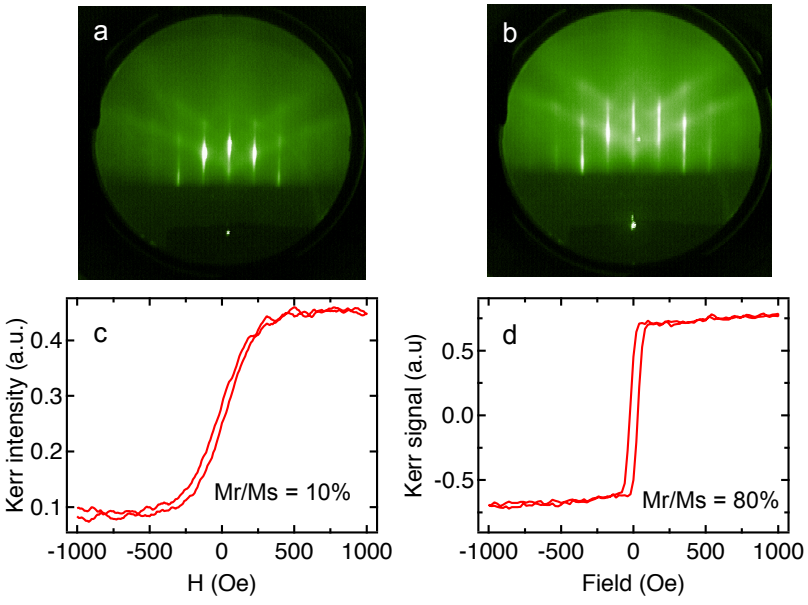

Figure 6.4: a) and b) are RHEED patterns for two Ag layers having small differences in quality and c) is the resulting MOKE loop for t_{Fe} of 0.63 nm on (a) and d) the MOKE loop for t_{Fe} of 0.8 nm on Ag layer on (b).

6.2 and 6.3 was repeated many times. However, the quality of the Ag buffer layer greatly de-

termined the quality of the magnetic properties and characteristics of the Fe layer and small differences can lead to drastic differences with some samples having little PMA and some having large PMA. In figure 6.4a and 6.4b are two RHEED patterns of an Ag buffer layer from two different samples. The RHEED patterns are quite similar with 6.4b being slightly better, but the magnetic properties of the Fe layer are quite different as shown in figure 6.4c and 6.4d. Figrue 6.4c is a hysteresis loop taken at an t_{Fe} of 0.63 nm and shows M_R/M_S = 0.1, where as figure 6.4d has a M_R/M_S = 0.8 for a t_{Fe} of 0.8 nm. We find that the PMA in the Fe/Ag layers is quite sensitive to the quality and crystallinity of the interface between the two layers. With the desired magnetic properties of the MgO/Fe/Ag achieved, next was the development of a dielectric that for applying a static electric field over a large area sample.

6.4 Development of Large Area Dielectric

In order to look at the magneto electric effect within the MgO/Fe/Ag system, a dielectric was needed that would be pinhole free over an large area ($\sim$4 mm^2 or larger) and would not break down with the application of a large electric field. To achieve this, the polymer Poly(methyl methacrylate) or PMMA was used. PMMA is a standard polymer used for many applications and is a common resist in the use for device fabrication through e-beam lithography. To test the electrically strength of PMMA for the use as an dielectric, a simple Au/PMMA/Au device was made through shadow mask with a schematic shown in figure 6.5. First, on an MgO substrate, a Au(100 nm)/Ti (20 nm) strip with dimensions of 4 mm wide

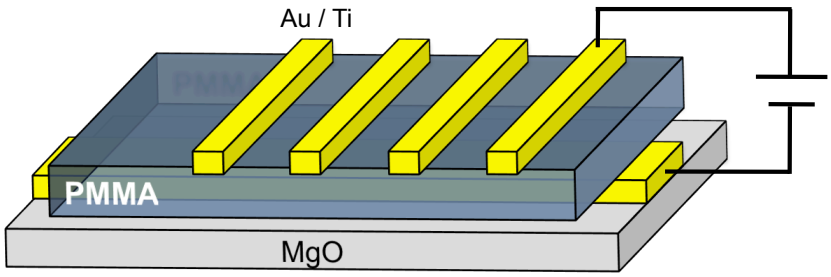

Figure 6.5: Schematic for Au/PMMA/Au device for electrical testing. The yellow electrodes are Au/Ti and the blue layer is the PMMA layer. Positive voltage is denoted as positive voltage applied to top electrode.

and 10 mm long was grown through a shadow mask by e-beam deposition. Next, the PMMA layer was applied through a series of spin coating and baking. The PMMA resist was first spin coated onto the sample at 3500 rpm and baked in a vacuum environment at 170 °C for 45 minutes, producing a layer 250 nm in thickness. This process was repeated three times to produce the final PMMA dielectric layer. Finally, another shadow mask was used to deposit a series of Au(100 nm)/Ti (20 nm) electrodes on top with a width of 1 mm as shown in figure 6.5 producing a 4 mm^2 cross section. A voltage was then applied across the top and bottom electrodes and the leakage current was measured in a DC 2-probe geometry. For all the I-V measurements, a loop style sweep was used with positive voltages corresponding positive voltages applied to the top electrode. The measurement started at 0 V and the applied voltage was slowly increased to the maximum for that range with the current measured at every 1 V. The applied V was then swept from the maximum V to the minimum V and then back to 0 V. Figure 6.6a show the resulting leakage current (nA) versus the applied voltage for Au/PMMA/Au device. The blue curve is for a voltage range of ± 60 V, the red curve is for the voltage range of ± 100 V and the black curve is for a voltage range of ± 150 V. For ± 100

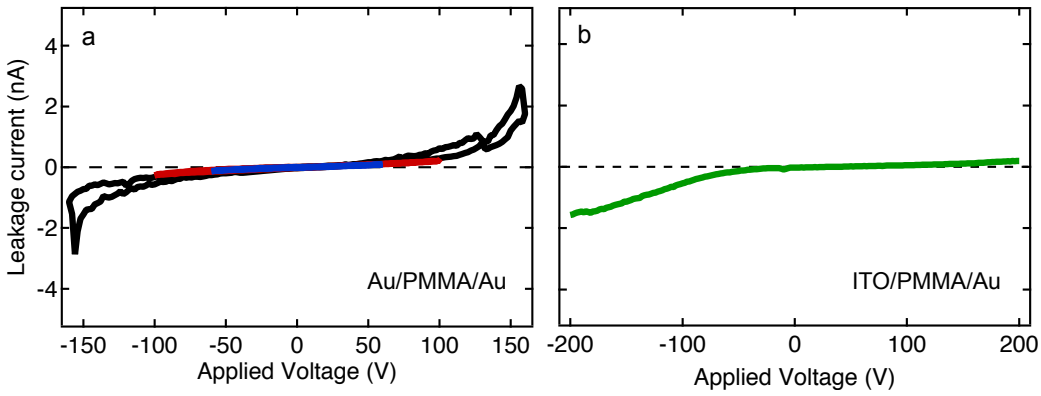

Figure 6.6: PMMA dielectric testing - Leakage current vs Gate voltage. a) is the leakage current vs. gate voltage on a Au/PMMA/Au device for voltage ranges of ± 60 V (blue), ± 100 V (red), and (± 150) V (black). b) is the leakage current vs. gate voltage for a ITO/PMMA/Au device with a voltage range of (± 200) V (green)

V and ± 60 V, the I-V curves are very linear with very little to no differences seen between the two. Also, the different voltage sweeps lie on the same curve indicating there was no irreversible changes arising from breakdown. The maximum leakage current seen for the ± 100 V range was $\sim$0.5 nA. For the ± 150 V range, we see that the there is some evidence for slight breakdown of the dielectric above 130 V, indicated by the loops in the black curve. However, even with the dielectric showing some breakdown, the maximum leakage current observed was only $\sim$3 nA at 150 V. For such a large cross sectional area, the PMMA shows that its quite robust to the applications of large voltage potentials. Next, the same test was done using an Indium tin oxide (ITO)/PMMA/Au device. The ITO is a transparent conductor and allows for MOKE to be performed through the electrode, which is critical for examining the magnetoelectric effect in MgO/Fe/Ag system. The ITO was deposited through a shadow mask inside a sputtering system. It should be noted that post annealing of ITO will increase the conductance and transparency, however, annealing on PMMA will cause the electrode

to develop cracks due to the difference in thermal expansion between ITO and PMMA. As deposited, the ITO is quite transparent and for this study, no post anneal was necessary. Figure 6.6b shows the I-V curve for Indium tin oxide (ITO)/PMMA/Au device for a voltage range of ± 200 V. The ITO/PMMA/Au device was quite robust and the maximum leakage current seen was $\sim$2 nA at -200 V. With the development of a robust dielectric for large area gating, we combine the MgO/Fe/Ag system with the ITO/PMMA layers to examine the electrical gating effects on the magnetic anisotropy in Fe.

6.5 Magnetoelectric Effect in MgO/Fe/Ag

A substrate mask was used to grow the MgO/Fe (wedge)/Ag on MgO(001) in a strip form similar to the bottom electrode shown in figure 6.5, followed by the growth of Al_2O_3 (100 nm), the PMMA layer and finally the ITO top electrodes (similar to figure 6.5).

The Fe wedge spanned across the with of the 4 mm electrode with a maximum thickness of 1 nm. Polar MOKE was performed on the sample through the ITO to ensure the Fe layer had the desired magnetic properties before applying the gate. In Figure 6.7a show a schematic of the sample and 6.7b, 6.7c, and 6.7d are representative hysteresis loops. Figure 6.7b is the hysteresis loop at $t_{Fe} = 0.53$ nm, figure 6.7c is at $t_{Fe} = 0.49$ nm and figure 6.7d is at $t_{Fe} = 0.35$ nm.

We find that the Fe layer still shows PMA even after the device processing with near square hysteresis loops at $t_{Fe} = 0.35$ nm. The region of interest however is at the thickness

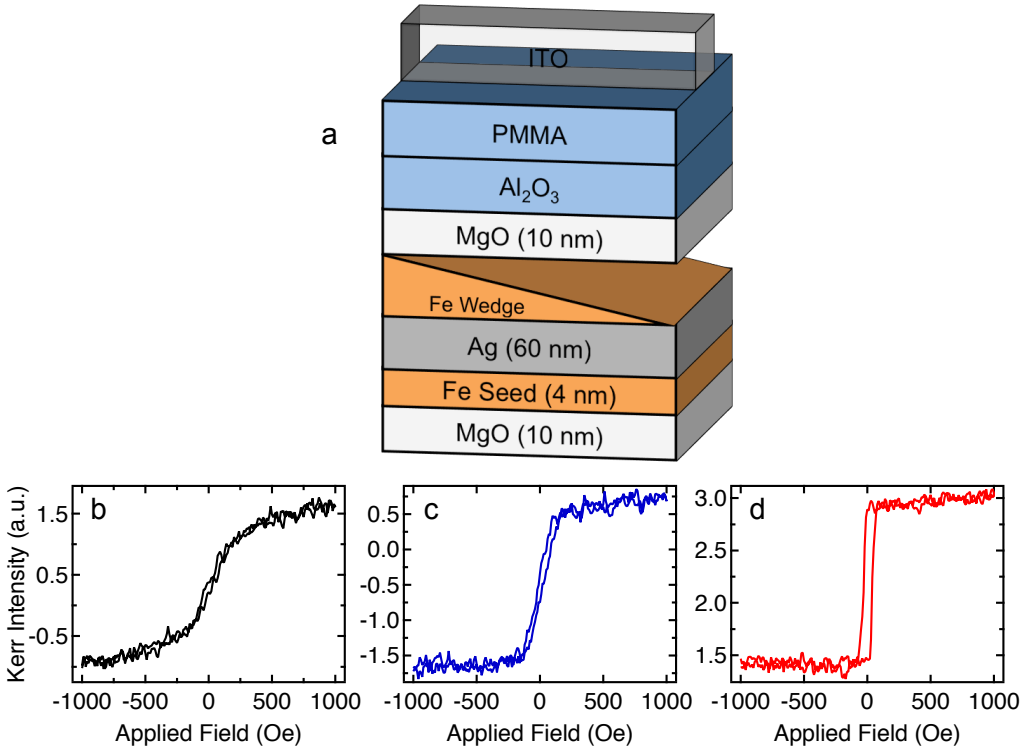

Figure 6.7: a) Polar MOKE analysis of ITO/PMMA/Al_2O_3/MgO/Fe/Ag system. MOKE was preformed through the ITO/PMMA/Al_2O_3/MgO layers. b) is the resulting MOKE loop for Fe thickness of $t_{Fe} = 0.53$, c) $t_{Fe} = 0.49$, and d) $t_{Fe} = 0.35$.

of 0.53 nm. Here, the anisotropy of the system is somewhere in-between perpendicular and in-plane, thus making it desirable for seeing maximum changes in anisotropy due to electrical gating. Next, a static gate voltage is applied across the Fe layer (Fig. 6.8a) and the resulting hysteresis loops are shown in figure 6.8b. With the application of a large positive voltage, the anisotropy of the Fe layer changes and prefers a more in-plane alignment (blue curve) where as the application of a larger negative voltage tilts the anisotropy more out of plane (red curve). The change is in the anisotropy is small but noticeable and the loops return to the the 0 V states, indicating there is no irreversible changes to the system. We find that the application of positive voltages (to the top electrode) always produces a change in the

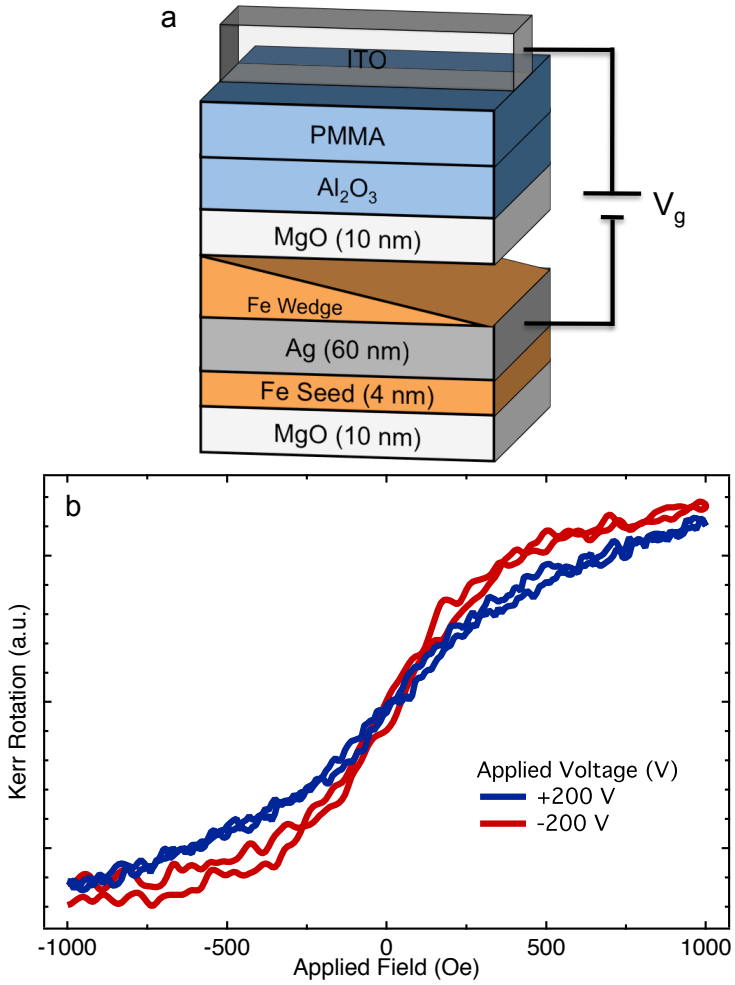

Figure 6.8: a) is the schematic of the sample. Positive voltages indicate positive applied V to the ITO top electrode. b) the resulting change in the anisotropy of the Fe layer at ($t_{Fe} = 0.49$. Red curve is for applied voltage of -200 V and blue curve is for applied voltage of $+200$ V.

anisotropy that prefers a more in-plane alignment and negative voltages tend to bring the anisotropy out-of-plane. We find that the effect shrink quite rapidly as t_{fe} is decrease and no noticeable effects were seen below 0.49 nm. As the t_{fe} is increased, the gating effect is still seen but is much less noticeable. An possible reasoning for voltage control anisotropy in the MgO/Fe/Ag system is that with the application of negative voltage could cause an increase in energy in the $d_{3z^2-r^2}$ ($m_z = 0$) states from the charge build up at the MgO/Fe interface. This leads to a reductions in the occupancy in $d_{3z^2-r^2}$ states and therefore possibly increasing the occupancy in the d_{xy} and $d_{x^2-y^2}$ states. This change in occupancy could lead to a modulation of the magnetic anisotropy of the Fe layer [28]. Further studies are need however to full understand the magneto electric effect in the MgO/Fe/Ag system.

6.6 Conclusion

In Conclusion, we show that a single crystal MgO/Fe/Ag system shows PMA for fe thicknesses below 1 nm and small difference in crystal quality of the Ag buffer layer can produce large changes in the PMA in the Fe layer. A PMMA dielectric layer was developed for applying large gate voltages across large cross-sectional areas of a samples and combine with an ITO electrode, enabled us to explore the magnetoelectric effect in MgO/Fe/Ag. We found that the application of a larger negative voltage causes the anisotropy of the Fe layer to prefer an perpendicular alignment where as large positive voltages produced a preference for in-plane alignment.

References

[27] M. Fiebig, J. Phys. D: Appl. Phys. **38**, R123 (2005).

[28] T. Maruyama, Y. Shiota, T. Nozaki, K. Ohta, N. Toda, M. Mizuguchi, A. Tulapurkar, T. Shinjo, M. Shiraishi, S. Mizukami, et al., Nature Nanotechnology **4**, 158 (2009).

[29] M. Weisheit, S. FŁhler, A. Marty, Y. Souche, C. Poinsignon, and D. Givord, Science **315**, 349 (2007).

[30] P. Borisov, A. Hochstrat, X. Chen, W. Kleemann, and C. Binek, Phys. Rev. Lett. **94**, 117203 (2005).

[31] X. Chen, A. Hochstrat, P. Borisov, and W. Kleemann, Applied physics letters **89**, 202508 (2006).

[32] X. He, Y. Wang, N. Wu, A. N. Caruso, E. Vescovo, K. D. Belashchenko, P. A. Dowben, and C. Binek, Nature Mater **9**, 579 (2010).

[33] Y. Chu, L. Martin, M. Holcomb, M. Gajek, S. Han, Q. He, N. Balke, C. Yang, D. Lee, W. Hu, et al., Nature materials **7**, 478 (2008).

[34] W. Eerenstein, N. Mathur, and J. Scott, Nature **442**, 759 (2006).

[35] V. Novosad, Y. Otani, A. Ohsawa, S. Kim, K. Fukamichi, J. Koike, K. Maruyama, O. Kitakami, and Y. Shimada, Journal of Applied Physics **87**, 6400 (2000).

[111] Z. Q. Qiu, J. Pearson, and S. D. Bader, Phys. Rev. Lett. **70**, 1006 (1993).

[112] M. Stampanoni, A. Vaterlaus, M. Aeschlimann, and F. Meier, Phys. Rev. Lett. **59**, 2483 (1987).

[113] B. Heinrich, K. B. Urquhart, A. S. Arrott, J. F. Cochran, K. Myrtle, and S. T. Purcell, Phys. Rev. Lett. **59**, 1756 (1987).

[114] N. C. Koon, B. T. Jonker, F. A. Volkening, J. J. Krebs, and G. A. Prinz, Phys. Rev. Lett. **59**, 2463 (1987).

Chapter 7

Fe_3O_4 Growth and Characterization

7.1 Introduction

Magnetite, Fe_3O_4, is known since ancient times, as a "lodestone" and was used to magnetize the mariner's compass. It belongs to the family of strongly correlated materials (i.e., with strong electron-electron interactions) and still attracts significant attention due to its interesting magnetic and electronic properties. Magnetite has a ferrimagnetic ordering, a classic example of the Nëel two-sublattice model of ferrimagnetism, archetypical of the spinel ferrites. It has a high Curie temperature ($>$850 K), low electrical resistivity at room temperature, and is predicted to be a half metal (100% spin polarization). These features and the high Curie temperature makes magnetite a good candidate for room temperature spintronic application. Fe_3O_4 is most famously known for it charge ordering phase transition called the Verwey transition [2].

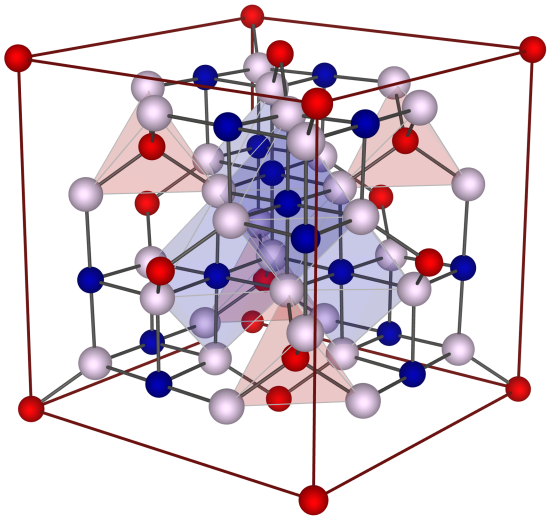

Figure 7.1: Crystal structure for Fe_3O_4 at room temperature drawn in *VESTA3* [115]. The tetrahedral (Fe^{3+}) A-sites shown in red spheres, the octahedral ($Fe^{3+/2+}$) B-sties are shown in blue and the oxygen atoms are shown in white.

7.1.1 Magnetite Properties

Magneties contains both Fe^{2+} and Fe^{3+} ions and is sometimes formulated as $FeO{\cdot}Fe_2O_3$. Fe_3O_4, at room temperature, crystallizes in the cubic inverse spinel structure with space group $Fd3m$, lattice constant of $a = 8.396$Å. Within the inverse spinal structure, the oxygen anions, O^{2-}, form a close-packed face-centered-cubic (fcc) sublattice with Fe^{2+} and Fe^{3+} cations located in interstitial sites [2, 116]. Figure 7.1 shows the inverse spinal structure of Fe_3O_4 at room temperature. The Red spheres represent the tetrahedral A (8-fold) positions are occupied by Fe^{3+} cations and the blue sphere are the octahedral B (16-fold) positions containing the $Fe^{3+/2+}$ cations. Because of the B-sites having a probability of having either Fe ion state, shows that there is electron exchange (thermally activated fast electron hopping) between B-sites and gives rise to its conductivity [2]. The fact that spinal ferrets, like $CoFe_2O_4$, only

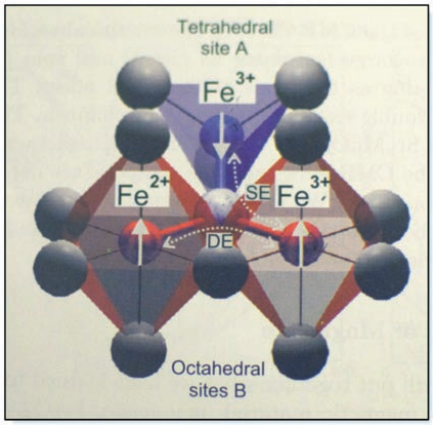

Figure 7.2: The presence of both double exchange and superexchange in Fe_3O_4 adapted from reference [117].

have Fe^{3+} at the B-sites and are insulating, support the explanation of the charge disorder and conductivity in Fe_3O_4

Another interesting feature of magnetite is that it is a ferrimagnetic material due to both having double and superexchange present as depicted in figure 7.2. In the figure 7.2, it shows the magnetic superexchange (SE) and double exchange (DE) coupling of one Fe ion to the other inequivalent neighbors. The SE between the A site and B site ions causes the two Fe^{3+} ions to align anitferromagnetically, give zero magnetic moment. The DE between the different B site ions causes them to align ferromagnetically, giving rise to a net moment. The Fe^{3+} ions have a moment of $5\mu_B$ and the Fe^{2+} has a moment of $4\mu_B$. So with the SE canceling out the $\pm 5\mu_B$ of the Fe^{3+} ions, we find that the Fe_3O_4 has a net magnetic moment of $4\mu_B$ (per formula unit). Magnetite has a high Curie temperature of 858 K and is also predicted to be a half metal [117, 118].

Most interesting, magnetite also has a first-order phase transition at T_V=120 K, called the Verwey transition. The Verwey transition, discovered in 1939 as one of the first metal-

to-insulator transitions generated by electron-electron correlations, has been studied intensively over the past seven decades. As magnetite is cooled through the Verwey temperature (T_V), an abrupt change in the crystallographic and electronic structure are observed and accompanied by changes in related properties such as electrical, magnetic, thermodynamic and mechanical interactions. The electrically conductivity changes from a (bad) metal ($10^3 < \sigma < 3 \times 10^4 Ohms^{-1}m^{-1}$) to an insulating state ($\sigma \sim 0.1 Ohms^{-1}m^{-1}$) through the Verwey transition.

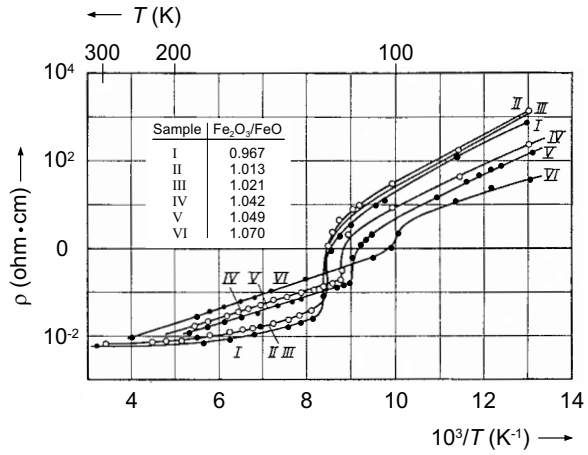

Figure 7.3: Resistivity versus temperature for magnetite taken from Ref. [2] The large jump in resistivity seen in the graph is indicative for the Verwey transition. The curves in the figure shows the effects of chemical composition on the Verwey transition.

Figure 7.3 from reference [2] shows resistivity versus temperature measurements for magnetite at various chemical concentrations, work done originally by Verwey. The Verwey transition is a charge order-disorder transition, but the detail and origins are still debated. At room temperature, magnetite is in a charge-disorder state, as mentioned above. As the same is cooled, the electron hopping at the B sites stops and the charge-ordering occurs. Only recently has the charge-ordering state been verified through various x-ray scattering

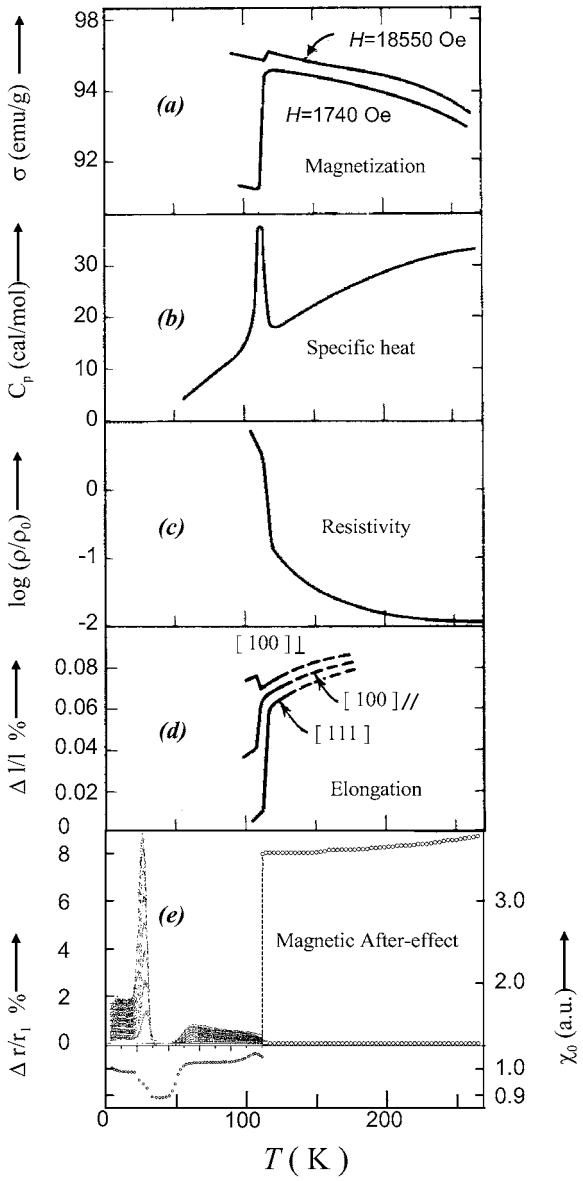

Figure 7.4: Adapted from Ref. [2] showing how different properties are affected at the Verwey transition.

experiments [119–125]. In the review done in ref. [2] shows a figure summarizing the many property changes seen at the Verwey transition shown in figure . Studies on bulk single-crystals have established that stoichiometry, impurities, and hydrostatic pressure (strain) are important factors in determining T_V [2, 126–128].

Overall, magnetite is a very interesting material with many intriguing properties that makes it very attracttive for research purposes. In this chapter, I will go over on how we grew Fe_3O_4 thin films through reactive MBE techniques in order to explore magnetite.

7.2 Fe_3O_4 Growth Through Reactive MBE

7.2.1 Varying Oxygen Partial Pressure

In order to explore all the fascinating properties of magnetite, especially the verwey transition, we need to first develop a reliable growth recipe for producing high quality single crystal Fe_3O_4. Due to the double lattice matching between MgO ($a_{MgO} = 4.213$Å) and Fe_3O_4 ($a_{Fe_3O_4} = 8.3967$Å), single crystal MgO(001) substrates are used for studying the electrical and magnetic properties of epitaxial grown magnetite thin films. The MgO substrates are first rinsed in DI water and then loaded into the molecular beam epitaxy (MBE) ultra high vacuum (UHV) growth system with a base pressure of 1×10^{-10} torr. The MgO substrate is annealed in UHV at 600°C for 45 minutes, followed by the growth of the 10 nm MgO Buffer layer at 350°C. (Details in section 2.5) Typical RHEED patterns of the MgO (10 nm) layer is shown in figure 7.5a and 7.5b. Next, we use a reactive MBE to grow the magnetite on the MgO. First, the substrate is heated an elevated temperature (i.e. 200°C) followed by the introduction of molecular oxygen into the UHV chamber. Elemental Fe is then evaporated in the oxygen environment through a thermal effusion cell at a rate of $\sim$0.13 nm / min. There are many different ways of producing Fe_3O_4 and has been shown that heating the substrate

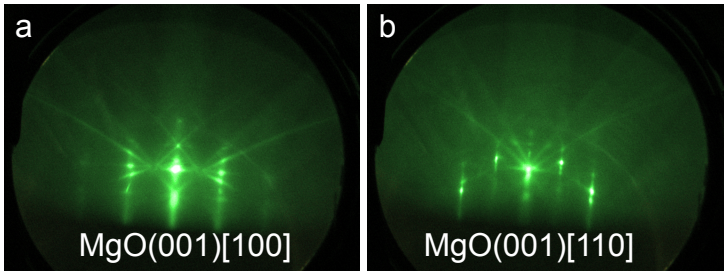

Figure 7.5: Typical RHEED patterns of the MgO (10 nm) layer a) in the MgO[100] direction and b) in [110] direction.

during the growth helps improve the structural quality and promotes higher quality deposition compared those at room temperature.

Initial test growths of Fe_3O_4 set out to see what partial pressures of O_2 is needed for growing Fe_3O_4. Three test samples where grown at different O_2 partial pressures (P_{O_2}) at a substrate temperature, T_S, = 200°C. Previous work done in the group[ref yan] showed similar temperatures was an ideal for formation of Fe_3O_4 on GaAS through post-oxidation. However, with reactive MBE (rMBE), T_S dependence will still need to be explored and explained in a later section. Three samples were grown, Sample A had a $P_{O_2} = 8.0 \times 10^{-8}$ torr, Sample B had $P_{O_2} = 1.0 \times 10^{-7}$ torr, and Sample C had $P_{O_2} = 1.2 \times 10^{-7}$ torr. All the samples had equivalent amount of Fe deposited, that is 10 nm of Fe, which leads to$\sim$20 nm of Fe_3O_4. The resulting RHEED patterns for Sample A, B, and C are shown in Figure 7.6. Fig. 7.6a, 7.6b, and 7.6c are RHEED patterns taken in the MgO(001)[100] for Sample A, B, and C, respectively. Fig. 7.6d, 7.6e, and 7.6f are RHEED images along the MgO(001)[110] for sample A, B, and C, respectively. What is revealed is that for reactive MBE, the threshold O_2 partial pressure needed is $\sim 1.0 \times 10^{-7}$ torr and below this, a Fe-rich Fe oxide forms (Fe_xO_y)

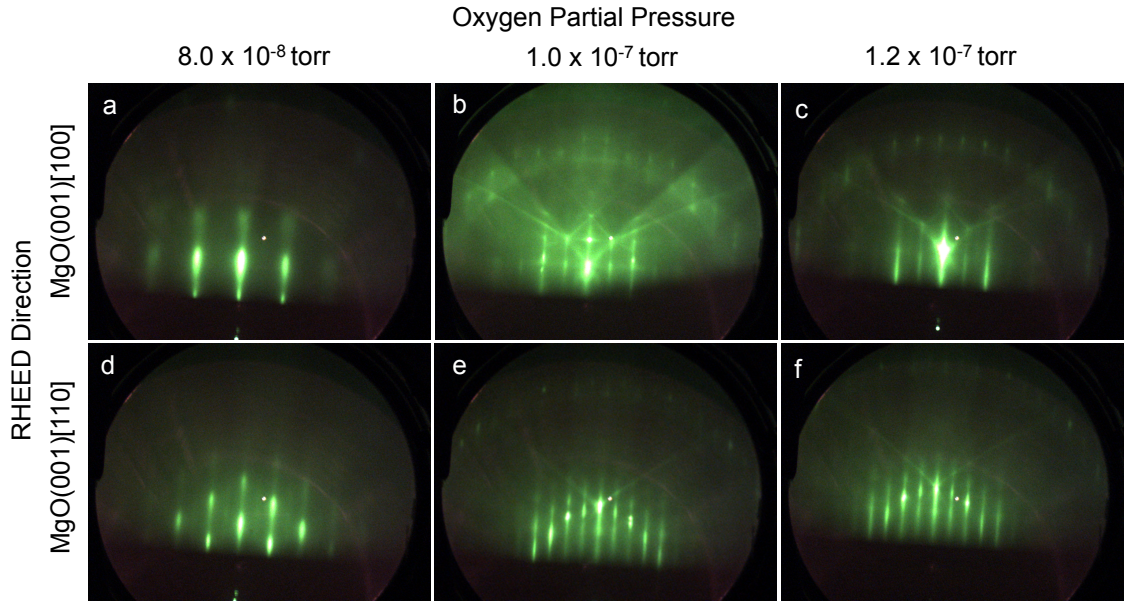

Figure 7.6: Fe_3O_4 RHEED patterns - Oxygen Pressure. The top row is the RHEED patterns taken in the MgO [100] direction and the bottom row is the RHEED patterns in the MgO [110]. a) and d) are the RHEED patterns after the rMBE growth of iron oxide at $P_{O_2} = 8.0 \times 10^{-8}$ torr. b) and e) is the RHEED patterns of Fe_3O_4 after rMBE growth at $P_{O_2} = 1.0 \times 10^{-7}$ torr and $P_{O_2} = 1.2 \times 10^{-8}$ torr (c and f).

as seen in the RHEED patterns in Fig. 7.6a and 7.6d. In figure 7.6a, that the diffraction streaks have a defuse nature with a periodic broadening, suggesting is landing growth sequence. The broad diffraction spots also indicate a non-uniform surface. Finally, the spacing between the RHEED diffraction streaks is more indicative to a Fe RHEED pattern than that of Fe_3O_4. All of this is suggesting that the thin films grown are heavy Fe rich and are not fully oxidized. However, once the pressure reaches $\sim 1.0 \times 10^{-7}$ torr and above (Sample B and C), we find that the RHEED pattern is much different and is very indicative to the expect RHEED pattern of Fe_3O_4 on MgO(001). [ref ann and others] Figure 7.6b and 7.6e for Sample B shows very sharp, streaky diffraction rods with spacings expected for Fe_3O_4. The pattern shows small bright diffraction spots and bright Kikuchi lines, indicating the sample has a

atomically smooth single-crystalline surface. Sample C (Fig. 7.6c and 7.6f) has very similar RHEED patterns to Sample B but with slightly sharper diffraction streaks and Kikuchi lines. This suggest, structurally, Sample B and C are very similar with Sample C having slightly better crystalline properties and shows a $P_{O_2} > 1.0 \times 10^{-7}$ torr is needed for epitaxial growth of Fe_3O_4 on MgO(001).

7.2.2 Structural Dependence on T_S

Next, the temperature dependent growth quality is examined for the Fe_3O_4. To examine how the growth temperature (T_S) influences the growth evolution and quality of the Fe_3O_4, we grow various samples at different substrate temperatures and examine the crystalline structure through the growth. Again, elemental Fe is then evaporated at a rate of ~0.13 nm / min in the oxygen environment at $P_{O_2} \sim 1.2 \times 10^{-7}$ Torr. Each sample consist of Fe_3O_4(20 nm)/MgO(10 nm)/MgO(001) and were monitored by RHEED before, during and after the growth of the Fe_3O_4. Low energy electron diffraction (LEED) and Auger spectroscopy was performed in an adjacent UHV chamber well as.

Figure 7.7 shows representative RHEED patterns of the Fe_3O_4 layer grown at different T_S ranging between 150°C and 250°C. The left side (Fig. 7.7a, 7.7c, 7.7e, and 7.7g) are the RHEED patterns for the Fe_3O_4 layers along the Fe_3O_4 [110] crystal direction and the right side (Fig. 7.7b, 7.7d, 7.7f, and 7.7h) are the RHEED patterns along the Fe_3O_4 [100] direction. What is found is that there is little to no noticeable differences between the RHEED patterns between the different T_S. The RHEED patterns in the Fe_3O_4(001)[110] look very

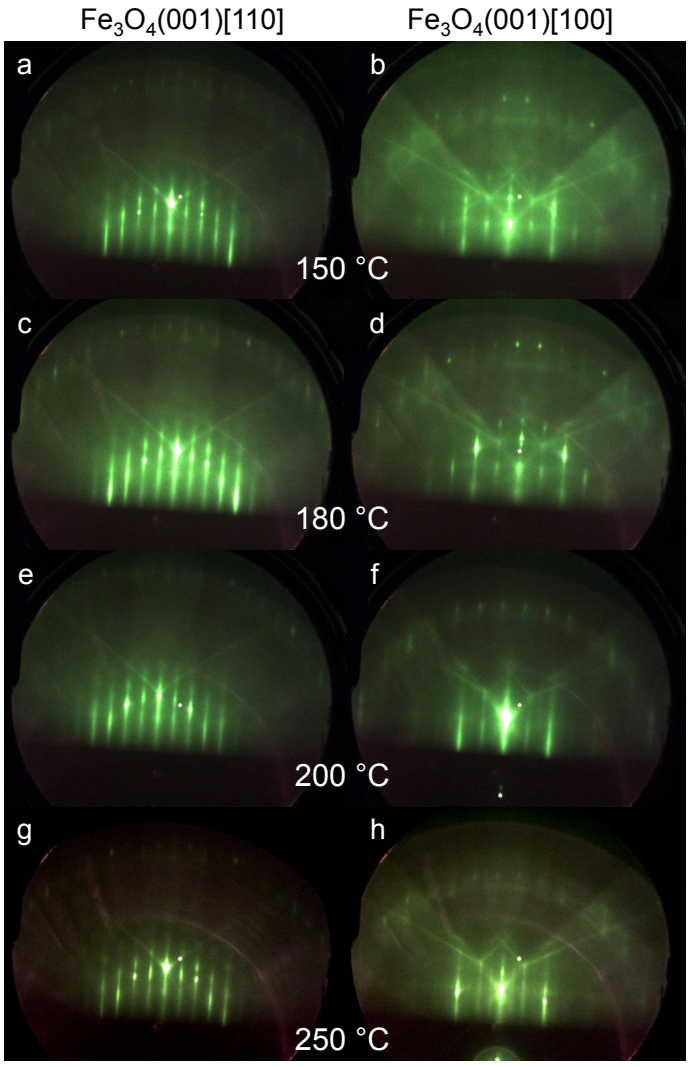

Figure 7.7: Fe_3O_4 RHEED patterns for various T_S The RHEED patterns of Fe_3O_4 grown at T_S =150°C (a and b), T_S =180°C (c and d), T_S =200°C (e and f) and T_S =250°C (g and h). The left column are the RHEED images in the Fe_3O_4 [110] direction and right column are the RHEED images in the Fe_3O_4 [100] direction.

similar, all showing sharp, streaky diffraction rods with sharp Kikuchi lines. The same can be said for the RHEED patterns looking in the Fe_3O_4(001)[110]. Due the variations in RHEED that arises from differences in the incident beam angle and sample to sample variations, it is difficult to conclude that there is any small difference in crystal structure.

To further examine the growth sequence of the Fe_3O_4 at the different T_S, time evolution of a RHEED line cut is explored. Figure 7.8 shows a representative time laps RHEED for the initial 15 minutes of the growth at $T_S = 200°C$. Figure 7.8a is the initial line cut of the

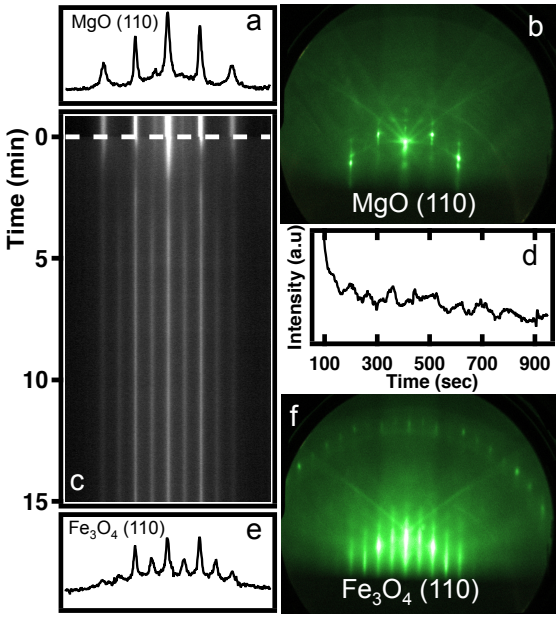

Figure 7.8: Fe_3O_4 Timelaps RHEED at 200°. a) Is the line cut across the MgO[110] RHEED pattern and b) is the RHEED pattern. c) is the time evolution of the growth of Fe_3O_4 for the first 15 minutes. The dash line indicated the opening of the Fe shutter. d) is small RHEED oscillations for the Fe_3O_4 growth, e) is the final line cut and f) is the RHEED pattern of the Fe_3O_4 layer.

MgO(001)[110] RHEED pattern (Fig. 7.8b) and Figure 7.8c is the time evolution of the line cut as the Fe_3O_4 is grown. The dash line in figure 7.8c indicates the opening of the Fe shutter. Fig. 7.8c shows that the line cut transitions continuously from the MgO[011] RHEED pattern (Fig. 7.8a and 7.8b) to the Fe_3O_4[011] (Fig. 7.8e and 7.8f) RHEED pattern, indicating epitaxial growth of Fe_3O_4 on MgO. Figure 7.8d show the RHEED intensity oscillations obtained from the time laps, supporting that the Fe_3O_4 is growing epitaxially. Interestingly, all the growth ranging between T_S = 150°C and 250°C exhibited the same behavior seen in

Figure 7.8, showing epitaxial growth of Fe_3O_4 and suggest, structurally, that there is little dependence on T_S agreeing with figure 7.7.

LEED and Auger spectroscopy was also performed on the various samples following the growth inside an adjacent UHV chamber without breaking vacuum. Figure 7.9 shows the resulting LEED patterns and Auger spectra for the Fe_3O_4 grown at $T_S = 100°C$. The magnetite thin films exhibit shape LEED patterns, which is shown in Figure 7.9a and 7.9b with energies of 92.7 eV and 155.4 eV, respectively. The observation of the sharp LEED patterns in the magnetite film indicates a well ordered surface, in agreement with observation in the RHEED (Fig. 7.7 and Fig. 7.8). Figure 7.9c is the Auger Spectra showing Oxygen peak at ∼516 eV and Fe peaks ∼599 eV, ∼652 eV and ∼707 eV, well within the range expected for magnetite. Again, all these properties are seen for all T_S between 150°C and 250°C, further supporting that the Fe_3O_4 is growing epitaxially through this T_S range.

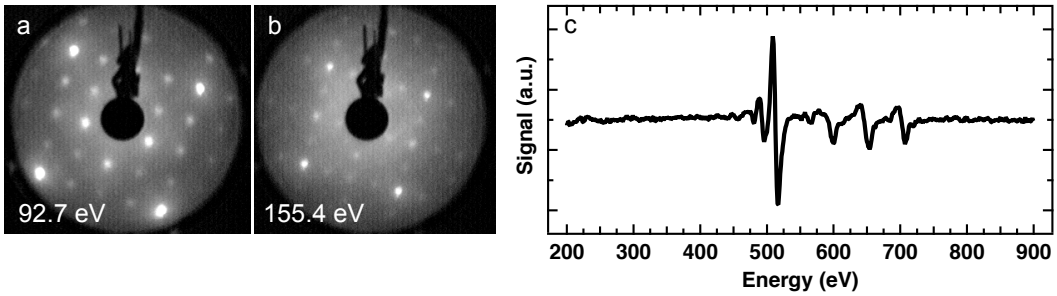

Figure 7.9: Fe_3O_4 (50 nm) ($T_G = 200°$) LEED and Auger spectroscopy. a) and b) are the LEED patterns for Fe_3O_4 at 92.7 eV and 155.4 eV, respectively. c) is the Auger Specra for the Fe_3O_4.

Finally, to further verify the single crystal nature of the Fe_3O_4 thin films and lack of dependence on T_S, X-ray diffraction (XRD) is preformed on thicker 50 nm Fe_3O_4 samples grown at 150°C, 200°C, and 250°C. What was observed is that the XRD scans were nearly

identical for all the samples and a representative XRD scan is shown in figure 7.10a. The XRD scan (Fig. 7.10a) shows peaks only at the MgO (200) and (400), which is expected for Fe_3O_4 on MgO due to the high lattice matching. The lack of other peaks show that there is no other phase of Fe oxide, such as Fe_2O_3, present in the Fe_3O_4 thin film and verifies the single-crystal structure of the material. High Resolution XRD (HRXRD) was measured around the location of the MgO (200) peak on the T_S=200°C sample and the Kiessig fringes indicates atomically smooth films with a thickness of 50 nm. XRD verifies what was observed in RHEED and LEED, that structurally, the epitaxial growth varies very little between T_S = 150°C and 250°C. It should be noted that epitaxial growth was observed at T_S as low at

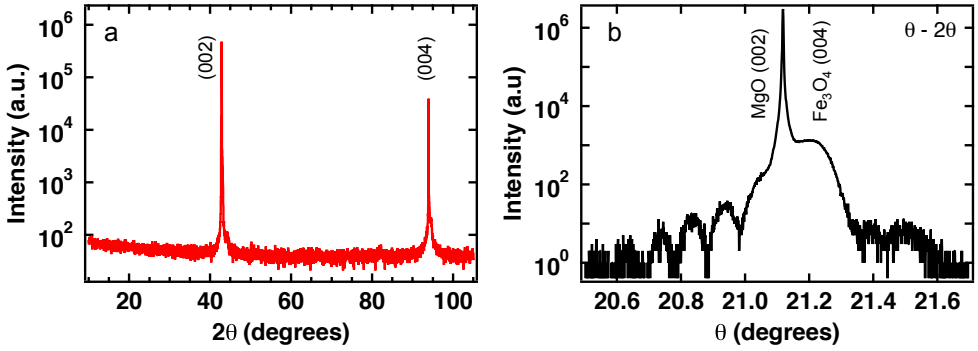

Figure 7.10: X-ray Differaction of 50 nm Fe_3O_4 thin fims on MgO(001). a) is the XRD scan of the Fe_3O_4 thin film and b) is the HRXDR of the same film centered around the MgO(002) peak.

110°C and as high as 280°C but, as explained in the following sections, the electrical and magnetic properties suffer suggesting that the composition of the Fe_3O_4 is compromised. Most likely the Fe_3O_4 thin films are Fe rich at the lower temperatures due to the lack of heat energy for full oxidation and Fe^{3+} rich at the higher temperatures. Therefore, at the length scale of the lattice (i.e. Structurally), we find practically no dependence on the T_S, yielding

epitaxial growth of Fe_3O_4 in growth region between 150°C to 250°C. However, due to the complex nature of Fe_3O_4, small changing below this length scale (i.e. chemically) can have drastic effects on the electric and magnetic properties.

7.3 Electrical Properties of Fe_3O_4

For more precise testing of the quality of Fe_3O_4 in the temperature region of 150°C to 250°C, electrical measurements will give more insight to compassion quality of the Fe_3O_4. The electric properties of magnetite is quite interesting because of its famous metal-to-insulator phase transition known as the Verwey transition with a phase transition temperature, the Verwey temperature (T_V), near 120 K. As bulk Fe_3O_4 is cooled through T_V, magnetite goes from metallic to insulating with a large discontinuous jump at T_V. Therefore, by examining how the Verwey transition is effected by the different T_S, we can further refine the temperature range for growing high quality Fe_3O_4 thin films.

The temperature dependent resistance of Fe_3O_4 thin films was examined with the Van der Pauw (VDP) sheet resistance measurement within a liquid He flow cryostat. For the temperature dependence, temperature cycling was kept the same for all samples and for every scan. All the samples were first cooled and measure through a warming process in the following way. First, the sample was cooled to 40 K and was allowed to stabilized for 1 hour. The sample was then warmed to 50 K and again stabilize for another 30 minutes. Once stabilized, the measurement began with the sample slowly warmed to each set temperature, allowed to

stabilize for 5 min, followed by the measurement of the *I-V* curve through the VDP sheet resistance measurement.

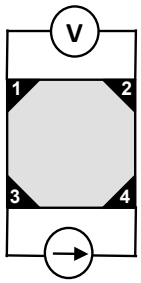

Figure 7.11: Van Der Pauw Measurement setup. Current is applied between electrodes 3 and 4, and voltage is measured between electrodes 1 and 2.

The Van Der Pauw method is commonly used to measure the resistively thin film sample geometry. The the set up used in this experiment, square thin film were contacted on the outer four corners as shown in figure 7.11. A current source is used to pass a current across two adjacent electrodes on one side of the sample between electrodes 3 to 4 (I_{34}) and the voltage is measured on the opposite side across electrodes 1 to 2 (V_{12}). An *I-V* is collected ranging from $\pm$ 0.5 μA with scans starting and ending at 0 μA (Fig. 7.12a inset). The slope of the *I-V* curve yields the resistance, $R_{34,12}$. The same measurement is measured is initially repeat for for the vertical combinations, that is I_{13} and V_{42}, and for all combinations in the vertical and horizontal directions to ensure the measured van der pauw resistance (R_{VDP}) is constant in all reciprocal geometries. Typically, there is only a $< 4\Omega$ difference between all measurements, leading to

$$R_{34,12} = R_{12,34} = R_{43,21} = R_{21,43} = R_{horizontal} \tag{7.1}$$

$$R_{31,42} = R_{42,31} = R_{13,24} = R_{24,13} = R_{vertical} \tag{7.2}$$

and therefore, we can say

$$R_{horizontal} = R_{vertical} \tag{7.3}$$

In order to calculate the sheet resistance (R_s), measured in Ω/square, one has to use the van der pauw relation, which is

$$e^{-\pi R_{vertical}/R_s} + e^{-\pi R_{horizontal}/R_s} = 1 \tag{7.4}$$

and since $R_{horizontal} = R_{vertical} = R_{VDP}$, equation 7.5 reduces to

$$2e^{-\pi R_{VDP}/R_s} = 1 \tag{7.5}$$

and solving for R_s,

$$R_s = \frac{\pi R_{VDP}}{\ln 2} \tag{7.6}$$

The resulting temperature (T) dependent R_s curve for an Fe_3O_4 (20 nm) sample grown at T_S = 200°C is show in figure 7.12. Figure 7.12a is the R_s vs T curve plotted on a (log)-(linear) scale, receptively, and figure 7.12b is the same graph but is plotted as R_s (log) vs 1000/T. The top axis in figure 7.12b is the corresponding temperatures for the 1000/T axis. The R_s vs T graph is used to determine T_V and R_s vs 1000/T plot is used to compare temperature dependent curves. The R_s vs 1000/T graph accentuate features, making it easier to

distinguish difference between characteristics of different samples. In figure 7.12a, the 20 nm Fe_3O_4 film starts in an insulting state with $R_s \sim 9 \times 10^8$ Ω/sq. near 50 K. As the sample is warmed, R_s decreases by orders of magnitude until the sample reaches a temperature of 115 K. At this point, the resistance decrease at a much slower rate, dropping from $R_s \sim 9 \times 10^4$ Ω/sq to $R_s \sim 7 \times 10^3$ Ω/sq over a temperature range of $\sim \Delta 180$ K. This sharp transition at 115 K (Blue arrow in fig. 7.12a and Red arrow fig. 7.12b) is indicative of the Verwey transition with T_V = 115 K.

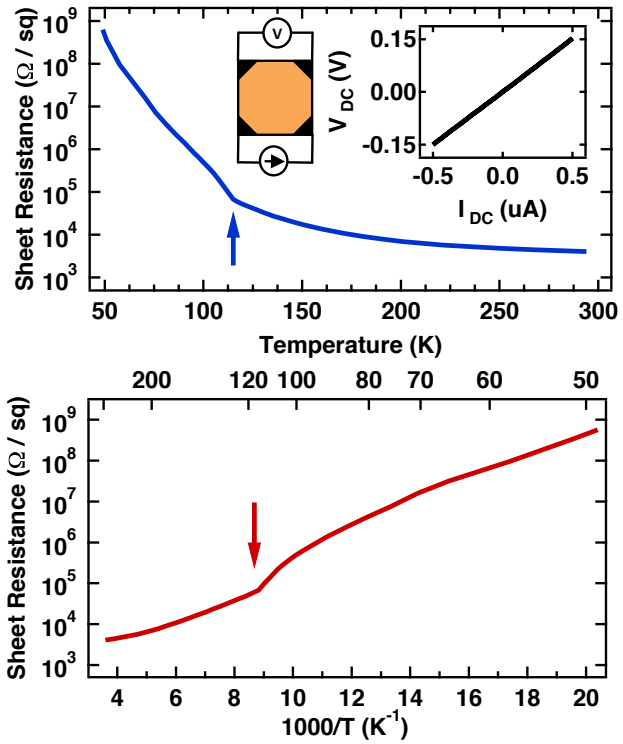

Figure 7.12: Temperature dependence measurement of the resistance in Fe_3O_4 thin films. a) is R_s vs temperature (K) with the arrow indicating the Vewey temperature (115 K). inset in a) shows a typical linear DC-IV curve. b) is the same temperature dependence shown in a) but plotted on the 1000/T scale.

By examining the R_s vs T characteristics below and above T_V and the value of T_V for samples grown at different T_S, we can refine the growth regime for Fe_3O_4. In Figure 7.13 shows representative R_s vs T for 20 nm Fe_3O_4 thin films grown at T_S=250°C (black), T_S=200°C (red) and T_S=150°C (blue) with corresponding colored arrows indicating T_V for each T_S, which summarized the T_V vs T_S inset. Figure 7.13 shows that the Verwey transition

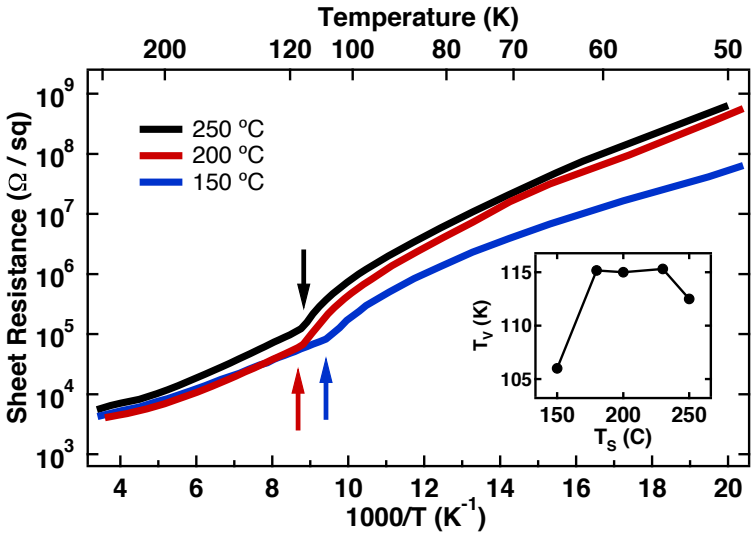

Figure 7.13: Growth Temperature Dependence for R_s vs T. The black curve is the R_s vs T for Fe_3O_4 grown at T_S=250 °C. The red curve is the R_s vs T for Fe_3O_4 grown at T_S=200 °C and the blue curve is the R_s vs T for Fe_3O_4 grown at T_S=150 °C. The corresponding colored arrows indicate the T_V for each T_S and is summarized in the inset.

is quite sensitive to T_S suggesting the chemical composition is slightly compromised if T_S is to high or to low. We find that the optimal growth regime for T_S is between 180°C and 250°C. The inset of figure 7.13 shows that outside the optimal growth regime, T_V decrease in temperature, suffering more if the T_S is to low. Looking at the sample grown at T_S=250°C (black curve in fig. 7.13), we see that the sample tends to be more resistive compared to samples grown at cooler temperatures. Typically, if Fe_3O_4 is over heated within an oxygen

environment, it will convert to another insulating stable iron oxide state, hematite or Fe_2O_3. The presence of extra Fe_2O_3 with the Fe_3O_4 would cause an imbalance between the Fe^{3+} and Fe^{2+} ions located at the *B*-sites, thus disrupting the complex charge transport seen in Fe_3O_4 leading to an overall increase in resistance. However, R_S vs T for T_S=250°C still shows a Verwey transition meaning that it is almost completely Fe_3O_4 with just a slight imbalance between the Fe^{3+} and Fe^{2+} ions. The opposite is the case for T_S=150°C (blue curve) in figure 7.13. Fe_3O_4 grown at T_S=150°C is consistently more metallic compared to the other samples, showing that the Fe_3O_4 is metal rich. Again, a Verwey transition is present for T_S=150°C, thus the sample is Fe_3O_4 with only a slight amount of unoxidized Fe present. The change in R_S at T_V and T_V itself shows that the growth regime needed for optimal growth of Fe_3O_4 thin films is between T_S=180°C and 230°C. Within this T_S window, we find the largest change in R_S at the Verwey transition and T_V is near the expected bulk value of $T_{V_{bulk}}$=120 K (red curve and inset in fig. 7.13).

With the growth temperature regime established, we next explored the effects of thickness on Verwey transition. It is well known that phase transitions, in general, tend to be suppressed as the dimensionality is decreased. Therefore, In order to explore any nanoscale effects on the Verwey transition, samples need to optimized between having a sharp, noticeable transition and thin enough for nanoscale effects to occur.

7.4 Thickness Dependence

Since it is necessary to find a regime in thickness for the Fe_3O_4 were there is a compromise between thickness and how sharp the verwey transition is, we take a look at the R_S dependence on thickness. The samples were all grown at T_S=200°C on MgO(10 nm)/MgO(001) and thicknesses ranged from 10 nm to 100 nm. Figure 7.14a shows the resulting R_S vs 1000/T curves for 10 nm (green), 20 nm (black), 50 nm (red) and 100 nm (blue). The resulting T_V vs thickness is shown in figure 7.14b. At a thickness of 10 nm, the Fe_3O_4 thin

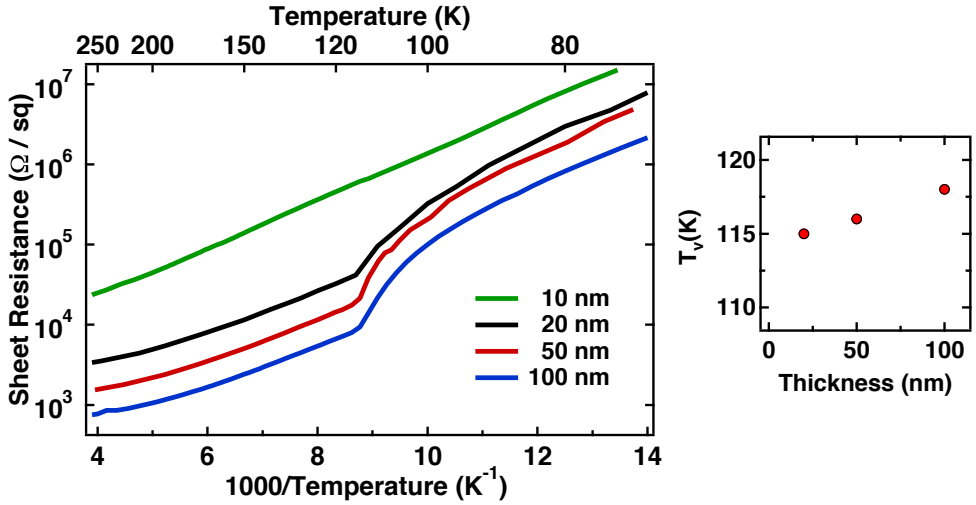

Figure 7.14: Thickness dependence of the Verwey Transition. a) shows the how thickness of the Fe_3O_4 thin film affect the Verwey transition. Green curve is for t_{Fe}=10 nm, black curve is for t_{Fe}=20 nm, red curve is for t_{Fe}=50 nm and blue curve is for t_{Fe}=100 nm. b) summarizes T_V for the different thicknesses.

film shows fairly steep R_S vs T dependence, but no Verwey transition is observed indicating that the phase transition is fully suppressed. As the thickness of the Fe_3O_4 films is increased, the resistance of the thin films decreases. At 20 nm, we see the Verwey transition and as the thickness is increased to 50 nm, there is an increase in T_V (116 K) and ΔR_S across the phase

transition. Again, at 100 nm, T_V increases to 118 K but ΔR_S nearly the same at 50 nm, showing that Verwey transition at 50 nm nearly identical to 100 nm. Below 50 nm, the phase transition begins to be suppressed and there is little difference between 50 nm and 100 nm. Therefore, thicknesses around 20 nm to 50 nm would be ideal for exploring the the Verwey transition, with 50 nm giving the best compromise between thickness and sharpness of the phase transition.

7.5 Magnetic properties of Magnetite

Another interesting property of the Verwey transition is that not only are the structural and electronic properties affected, the magnetic properties are also affected. At the Verwey transition, the magnetization of Fe_3O_4 sharply decreases as the temperature is decreased. Therefore, the magnetic properties of the optimized Fe_3O_4 thin films need to be examined. To look at the temperature dependence of the magnetization, a 100 nm Fe_3O_4 sample was grown at T_S = 200°C. The magnetic properties of Fe_3O_4 are characterized using magneto-optic Kerr effect (MOKE) with laser beam (812 nm wavelength) incident through the transparent MgO substrate. 100 nm was chosen since the Verwey transition is nearly identical to 50 nm but the MOKE signal is much better. The sample was measure as it was warmed from 70 K. The red dots plotted in figure 7.15 shows the resulting remanence (M_R) vs T and the blue curve is the R_S vs T curve for the same sample. We find that the M_R increases in signal height as the temperature is increased and abruptly plateaus at ∼118 K. Above 118 K, there is little

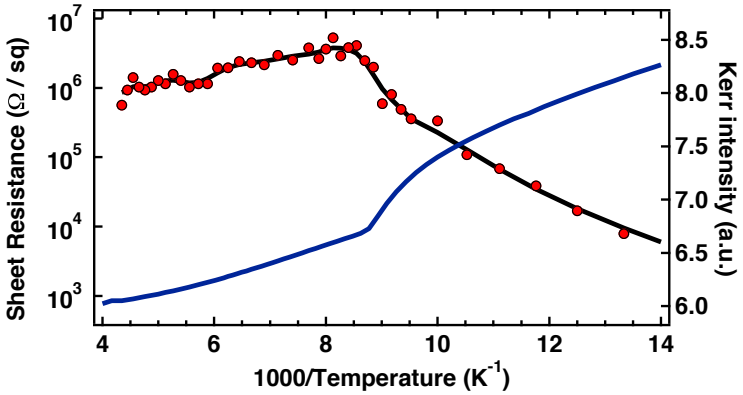

Figure 7.15: MOKE temperature dependence of Fe_3O_4. The red dots are the MOKE signal vs. temperature and the black curve is a guide to the eye. The blue curve is the R_s vs 1000/T from fig. 7.14

change in the remanence signal as the sample is warmed to RT. With the M_R vs T and R_S vs T plotted on the same graph, we see that the abrupt change in both is at 118 K, further verifying the presence of the Verwey transition.

7.6 Conclusion

Through reactive MBE, we are able to produce how quality Fe_3O_4 thin films. RHEED, LEED, Auger, and XRD showed that the thin films grew epitaxially on MgO(001). The T_S regime needed was between 150°C and 250°C and P_{O_2} needed to be greater than 1×10^{-7} torr. Sheet resistance measurements of 20 nm thin films revealed the sensitivity of Verwey transition to T_S and narrowed the optimal growth temperature range to between 180°C and 230°C. Next, the thickness was optimized for exploring nanoscaling effects and showed that 50 nm would be the preferred thickness. Finally, magnetic properties were looked at and showed that the films had the desired properties. Now with the growth of the Fe_3O_4 opti-

mized, we can begin to explore nanoscaling effects such as influences of electric fields to the properties of Fe_3O_4.

References

[2] F. Walz, J. Phys.: Condens. Matter **14**, R285 (2002).

[115] K. Momma and F. Izumi, Journal of Applied Crystallography **44**, 1272 (2011).

[116] M. Fonin, R. Pentcheva, Y. Dedkov, M. Sperlich, D. Vyalikh, M. Scheffler, U. Rüdiger, and G. Güntherodt, Physical Review B **72**, 104436 (2005).

[117] J. Sthr and H. C. Siegmann, *Magnetism*, Vol. 152 (Wiley New York, 2006).

[118] J. Wong, A. Swartz, R. Zheng, W. Han, and R. Kawakami, Physical Review B **86**, 060409 (2012).

[119] Y. Ding, D. Haskel, S. G. Ovchinnikov, Y.-C. Tseng, Y. S. Orlov, J. C. Lang, and H.-k. Mao, Phys. Rev. Lett. **100**, 045508 (2008).

[120] J. Garcia, G. Subias, J. Herrero-Martin, J. Blasco, V. Cuartero, M. C. Sanchez, C. Mazzoli, and F. Yakhou, Phys. Rev. Lett. **102**, 176405 (2009).

[121] D. J. Huang, H. J. Lin, J. Okamoto, K. S. Chao, H. T. Jeng, G. Y. Guo, C. H. Hsu, C. M. Huang, D. C. Ling, W. B. Wu, C. S. Yang, and C. T. Chen, Phys. Rev. Lett. **96**, 096401 (2006).

[122] J. E. Lorenzo, C. Mazzoli, N. Jaouen, C. Detlefs, D. Mannix, S. Grenier, Y. Joly, and C. Marin, Phys. Rev. Lett. **101**, 226401 (2008).

[123] G. K. Rozenberg, M. P. Pasternak, W. M. Xu, Y. Amiel, M. Hanfland, M. Amboage, R. D. Taylor, and R. Jeanloz, Phys. Rev. Lett. **96**, 045705 (2006).

[124] M. S. Senn, J. P. Wright, and J. P. Attfield, Nature **481**, 173 (2011).

[125] F. Zhou and C. Gerbrand, Phys. Rev. B **81**, 205113 (2010).

[126] E. J. W. Verwey, Nature **144**, 327 (1939).

[127] E. J. W. Verwey and P. W. Haayman, Physica **8**, 979987 (1941).

[128] V. A. M. Brabers, F. Walz, and H. Kronmuller, Phys. Rev. B **58**, 14163 (1998).

Chapter 8

Electric Field control of the Verwey Transition and Induced Magnetoelectric Effect in Magnetite

8.1 Background

Electric field control of magnetic and metal-to-insulator transitions in highly correlated materials has generated great interest both scientifically and technologically [129–133]. Magnetite (Fe_3O_4) is a highly correlated material that undergoes the well-known Verwey transition with sharp changes in the electric, magnetic, and structural properties at a transition temperature of $T_V \sim 120$ K [2, 126, 127]. The Verwey transition, discovered in 1939 as one of the first metal-to-insulator transitions generated by electron-electron correlations, has

been studied intensively over the past seven decades. Theoretically, Verwey proposed that the transition is due to charge ordering below T_V and subsequent models based on Mott insulator theory and band theory emerged [2]. Experimentally, studies on bulk single-crystals have established that stoichiometry, impurities, and hydrostatic pressure (strain) are important factors in determining T_V [2, 126–128]. Interestingly, the original hypothesis of charge ordering was verified only within the past few years by x-ray scattering [119–125]. Magnetite is also ferroelectric at low temperatures (<38 K) having an unusual case of ferroelectricity that originates from charge ordering of the Fe^{2+} and Fe^{3+} ions [134–138]. The electrical polarization in magnetite is generated by the rearrangement of electron distribution without a large corresponding displacement of lattice atoms [135]. Furthermore, this ferroelectric state exhibits a magnetoelectric effect where electrical polarization can be tuned by the orientation of a static magnetic field in relation to a poled perpendicular electric field [136, 138]. More recently, theoretical predictions of half-metallic behavior (100% spin polarization) [139] have motivated studies of magnetite thin films and heterostructures including incorporation into magnetic tunnel junctions [140] and integration with semiconductors [141]. Studies of thin films show the Verwey transition is weakened at low film thickness and the charge-ordered Verwey state can be destroyed by high current densities [131, 142]. Due to these interesting properties, magnetite has been the subject of many investigations by researchers in correlated electron materials, multiferroics, and spintronics.

Here, It is demonstrate that static electric fields can control the Verwey transition in Fe_3O_4 thin films. Our experiments utilize an electrostatic gate to apply a static electric field to a 50

nm magnetite film. It is found that the application of either positive or negative electric fields leads to an increase of the transition temperature (T_V). This result is quite surprising and intriguing because it was theoretically unpredicted despite years of intense research with magnetite and on the Verwey transition. Furthermore, electric field control of T_V leads to a new mechanism for generating a magnetoelectric effect distinct from the traditional magnetoelectric effect in ferroelectric magnetite [136, 138]. Previous demonstrations of electric field control of magnetic and metal-to-insulator transitions have resulted from various effects including current-induced breakdown of the insulating state [130, 131, 143], field-induced changes of carrier concentration [132, 144], field-induced strain generated by growth on piezoelectric substrate (i.e. composite system) [133, 145–147]. The results reported here are significantly distinct from these previous categories. Particularly, while current-induced breakdown is a highly non-equilibrium process, the present effect produces a true change in the equilibrium phase transition. We also find that this effect is not due to changes in carrier concentration, as shown by a symmetric dependence of T_V on gate voltage. Finally, this effect does not rely on external strain provided by adjacent layers. Thus, the electric field control of the Verwey transition represents a new type of electric field control in a highly correlated material.

8.2 Fe_3O_4 Growth and Characterization

Fe_3O_4 films of 50 nm thickness are grown on double-side polished MgO(001) substrates using reactive molecular beam epitaxy (MBE) in ultrahigh vacuum (UHV) with a base pressure of 1×10^{-10} torr. MgO substrates are first rinsed with de-ionized (DI) water. After loading into the MBE chamber, substrates are annealed at 600°C for 45 minutes. A 10 nm MgO buffer layer is grown at 350°C via electron beam (e-beam) deposition from an MgO source [106]. Next, the Fe_3O_4 layer is grown at 200°C by depositing elemental Fe in a molecular oxygen partial pressure of 1.2×10^{-7} torr. The Fe is evaporated from a thermal effusion cell at a rate of ∼0.13 nm/min (for pure Fe). The single-crystal structure is verified through *in situ* reflection high energy electron diffraction (RHEED) and low energy electron diffraction (LEED), as shown in Figs. 8.1a, 8.1b, and 8.1c inset. $\theta - 2\theta$ high resolution x-ray diffraction (HRXRD) scans exhibit a Fe_3O_4(004) peak near the MgO(002) substrate peak (Fig. 8.1c). Kiessig interference fringes indicate atomically smooth interfaces and verify the film thickness.

Electrical properties of Fe_3O_4 films are characterized using standard dc four-point probe measurements (Figure 8.1d inset). Resistance values are obtained from current-voltage (*I*-*V*) curves, which exhibit linear dependence (Figure 1e) above 70 K. The temperature dependence of resistance (Figure 8.1d, blue) exhibits a metal-to-insulator transition with a substantially higher resistance below 117 K, indicating the Verwey transition. Temperature dependence curves are measured as a function of increasing temperature, with the temperature

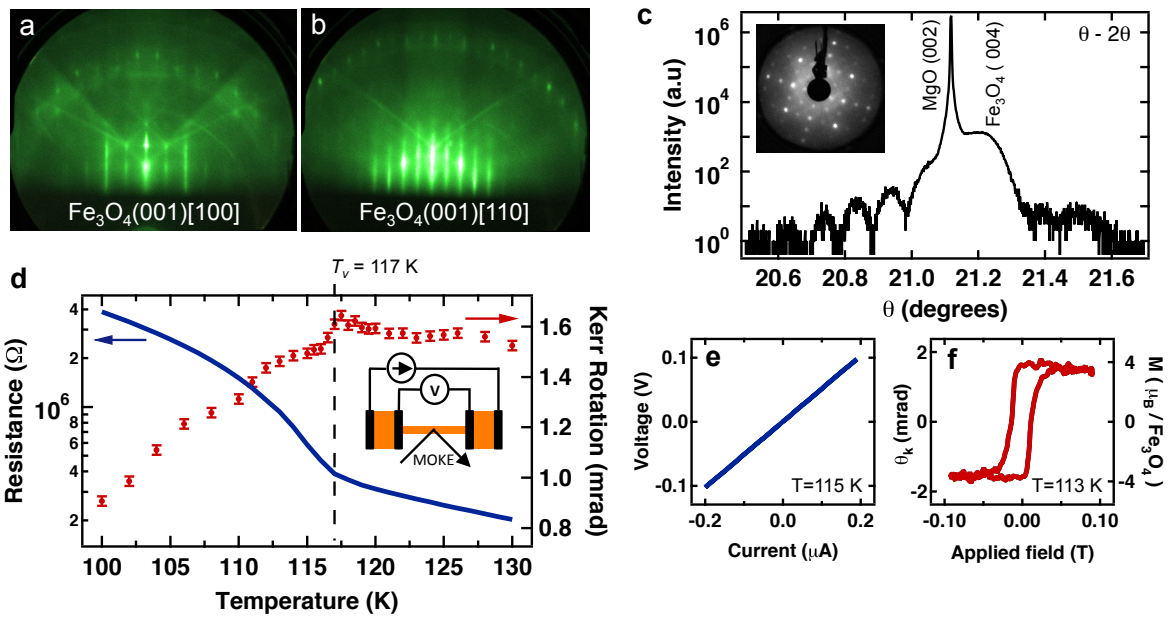

Figure 8.1: Characterization of Fe_3O_4 thin films. (a) and (b) are RHEED patterns for 50 nm Fe_3O_4 on MgO(001) along the [100] and [110] in-plane directions, respectively. (c) HRXRD $\theta - 2\theta$ scans measured around the location of the MgO(002) peak with Kiessig fringes. Inset: LEED pattern with incident energy of 160 eV. (d) Temperature dependence of resistance measured by four-point probe (blue) and magnetization measured by MOKE (red). The vertical dashed line indicates the Verwey transition. Inset: geometry for the resistance and magnetization measurements. (e) *I-V* curve for Fe_3O_4 channel at 115 K. (f) MOKE hysteresis loop for Fe_3O_4 at 113 K. The right axis shows absolute magnetization based on SQUID measurements on corresponding samples.

stabilized for 10 min before a measurement is taken. For each temperature, measurements are repeated to ensure the temperature is stable.

The magneto-optic Kerr effect (MOKE), with laser beam incident through the transparent MgO substrate, is used to characterize the magnetic properties of the Fe_3O_4 films (812 nm wavelength, *p*-polarized, 45° angle of incidence). Figure 1f shows a typical longitudinal MOKE hysteresis loop that exhibits large remanence and sharp magnetization reversal. The right hand axis of Fig. 1f displays the corresponding magnitude of the magnetization based on superconducting quantum interference device (SQUID) magnetometry. The temperature dependence of the MOKE signal (Figure 1d, red) exhibits a decrease of magnetization for temperatures below T_V. This behavior is characteristic of the Verwey transition in thin films, which is typically less sharp than in bulk materials.

8.3 Electrostatic gating of Fe_3O_4

To apply electric fields to the Fe_3O_4 film, an insulating layer (PMMA/Al_2O_3/MgO) is deposited on top of the Fe_3O_4, followed by a metallic electrostatic gate (Pd/Ti), as shown schematically in Figure 2a. The devices are fabricated through several steps of evaporation using shadow masks. For the Fe_3O_4 layer, a narrow channel is produced with a width of 210 μm, creating a small active area to reduce the occurrence of pinholes and gate leakage. The Fe_3O_4 channel length is 4.2 mm and the gate length is 3.3 mm. Alternate samples with Fe_3O_4 films covering a large area of the substrate produce similar results (Fig. 8.3). Pd(100

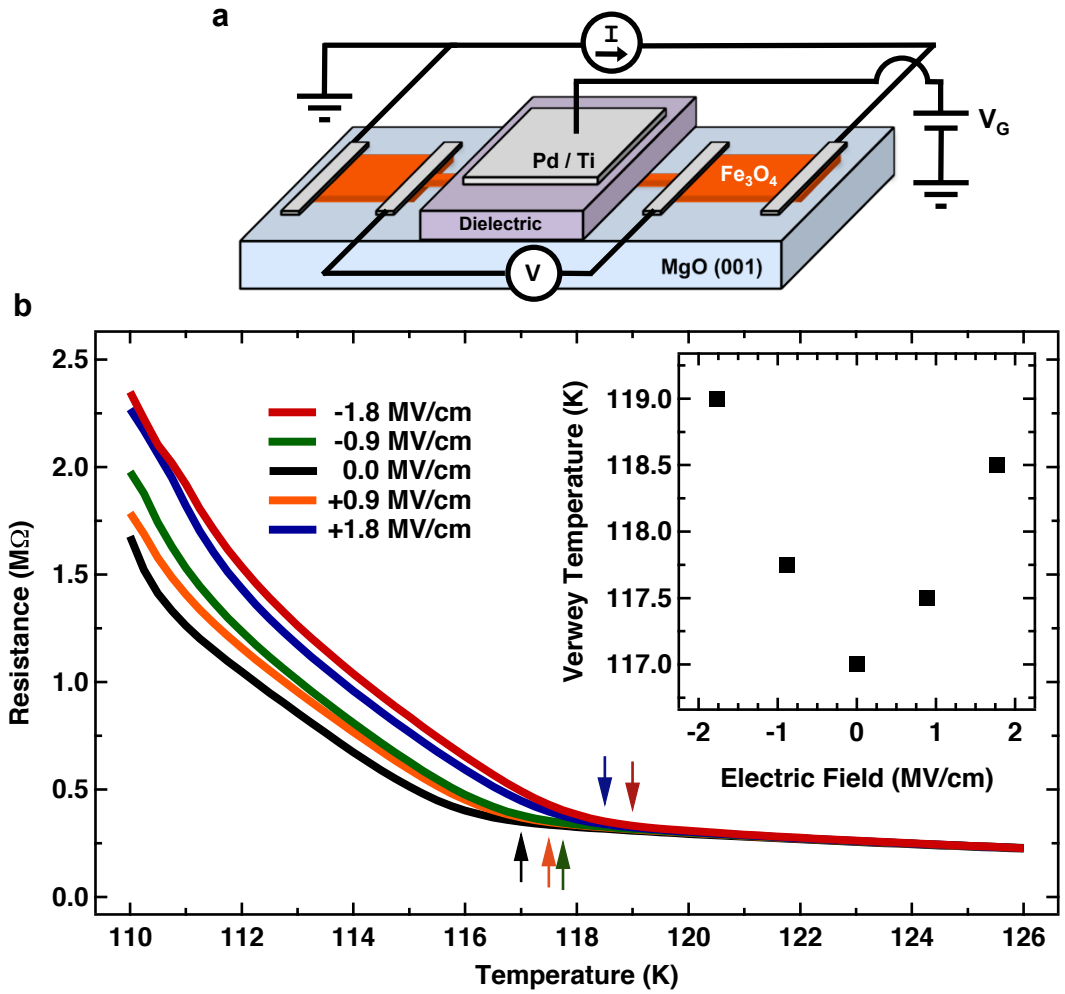

Figure 8.2: Electrical gating of Fe_3O_4 and Manipulation of the Verwey transition. (a) A schematic of the sample device structure. The dielectric layer consists of PMMA(900 nm)/Al_2O_3(50 nm)/MgO(10 nm). Positive electric field corresponds to the application of positive voltage to the top gate electrode. (b) Temperature dependence of resistance for applied electric fields of +1.8 MV/cm (blue), +0.9 MV/cm (orange), 0 MV/cm (black; from Fig. 8.1d), -0.9 MV/cm (green), -1.8 MV/cm (red). The arrows show T_V for each electric field, which is summarized in the inset.

nm)/Ti(15 nm) contacts (for four-point probe) are e-beam evaporated through a shadow mask in a separate system. Then a 10 nm MgO layer is grown on the Fe_3O_4 followed by a 50 nm Al_2O_3 layer. PMMA is then spin coated onto the sample at 3000 rpm and cured under a vacuum environment at 170°C. The spin coating and baking sequence is repeated three times giving a final PMMA layer thickness of 900 nm. Finally, a shadow mask is used to grow the Pd(100 nm)/Ti(15 nm) top gate electrode. Typical gate leakage is 0.5 nA for electric fields of $\pm$1.8 MV/cm.

An electric field is produced by applying a voltage (V_G) between the gate electrode and the Fe_3O_4 film. Figure 8.2b shows the temperature dependence of resistance for applied electric fields of +1.8 MV/cm (V_G = +60 V, blue), +0.9 MV/cm (V_G = +30 V, orange), 0 MV/cm (V_G = 0 V black), -0.9 MV/cm (V_G = -30 V, green), -1.8 MV/cm (V_G = -60 V, red) with corresponding colored arrows indicating T_V. The data clearly show that T_V varies as a function electric field, as summarized in the inset of Fig. 8.2c. At zero electric field, T_V is 117 K. Strikingly, both positive and negative electric fields cause T_V to increase, indicating that the shift in T_V depends primarily on the magnitude of electric field as opposed to its sign. The maximum effect is observed for -1.8 MV/cm, where T_V increases to 119 K, giving ΔT_V = +2 K.

We also examined the electric field effects for a large area Fe_3O_4 thin film device. A shadow mask is used to define a channel for magnetite deposition with dimensions of 4.2 mm wide and 9.0 mm in length, covering a large portion of the substrate. Again, Fe_3O_4 is deposited through the shadow mask and onto the MgO(001) buffer layer for single crystal

growth by reactive molecular beam epitaxy. The dielectric layer (PMMA/Al_2O_3/MgO) and top gate electrode (Pd/Ti) is then deposited onto the Fe_3O_4. The top gate electrode has a length of 4.5 mm producing a gating region of 4.2 mm $\times$ 4.5 mm in the center of the sample. Temperature dependent resistance is measured through standard 2-probe measurements and DC $I-V$ curves are taken at each temperature step to determine resistance values.

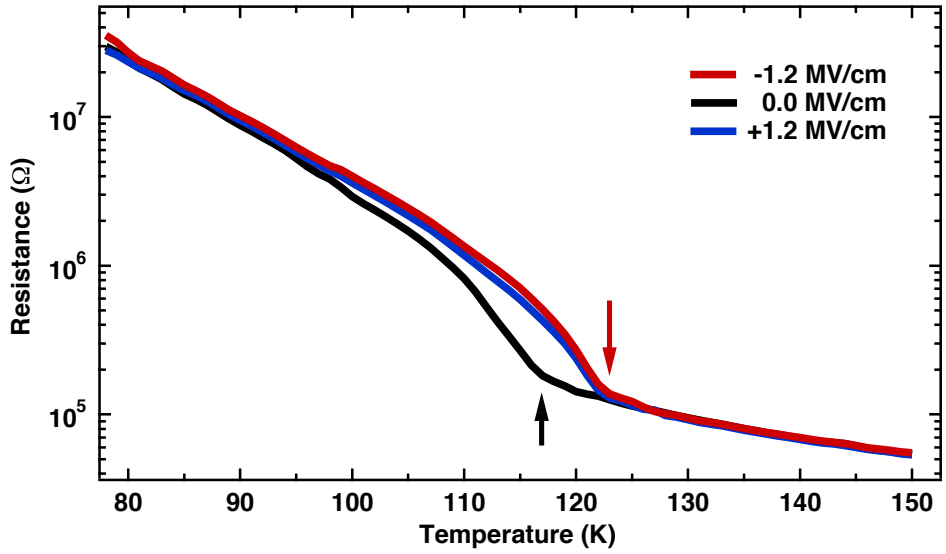

Figure 8.3: Manipulation of the Verwey Transition in Large area Fe_3O_4 device. Temperature dependence of resistance for applied electric fields of $+1.2$ MV/cm (blue), 0 MV/cm (black), -1.2 MV/cm (red). The red arrow shows T_V for electric fields of ± 1.2 MV/cm and the black arrow shows the T_V for electric fields of 0 MV/cm, with $\Delta T_V = +6$ K.

Figure 8.3 shows the temperature dependence of resistance for applied electric fields of -1.2 MV/cm (V_G = -40 V, red), 0 MV/cm (V_G = 0 V, black), $+1.2$ MV/cm (V_G = $+40$ V, blue), with the red arrow corresponding to T_V for electric fields ± 1.2 MV/cm and the black arrow for 0 MV/cm. For zero electric field, T_V = 117 K. In general, 50 nm Fe_3O_4 films demonstrated equivalent Verwey transition temperatures regardless of channel geometry. With the application of either positive or negative field, we find T_V increases to 123 K,

giving a $\Delta T_V = +6$ K, which is larger than the 210 μm wide channel device. As in the case of the 210 μm wide devices, the shift in T_V depends primary on the magnitude of the applied electric field as opposed to its sign. Typical gate leakage observed for the large area sample was $\sim$10 nA at the maximum applied electric field.

The increase of T_V seen in both the large area and 210 μm devices cannot be due to Joule heating because a heating artifact would appear as a reduction of T_V. We also rule out effects of irreversible sample change by measuring the zero electric field temperature dependence of resistance before and after taking the data in Fig. 8.2b and no irreversible changes were observed. Finally, we observe that temperature dependent resistance above T_V does not change with applied electric field, which shows that the metallic phase is insensitive to electric field.

8.4 Gate Dependent Resistance of Fe_3O_4

To gain further insight into the electric field effect, we perform a detailed study of the gate dependent resistance of the 210 μm channel Fe_3O_4 device under isothermal conditions. Figure 8.4a shows the resistance at 115 K as the electric field is swept between +1.8 MV/cm and -1.8 MV/cm. Consistent with the shift in T_V (inset Fig. 8.2b), the resistance increases for both positive and negative electric fields and the effect is slightly larger for negative electric fields. To quantify the symmetry of the electric field effect, we separate the change in resistance $\Delta R(E) = R(E) - R(0)$ into a symmetric part $\Delta R_S(E) = [\Delta R(E) + \Delta R(-E)]/2$ (Fig.

8.4b) and anti-symmetric part $\Delta R_A(E) = [\Delta R(E) - \Delta R(-E)]/2$ (Fig. 8.4c). Comparing

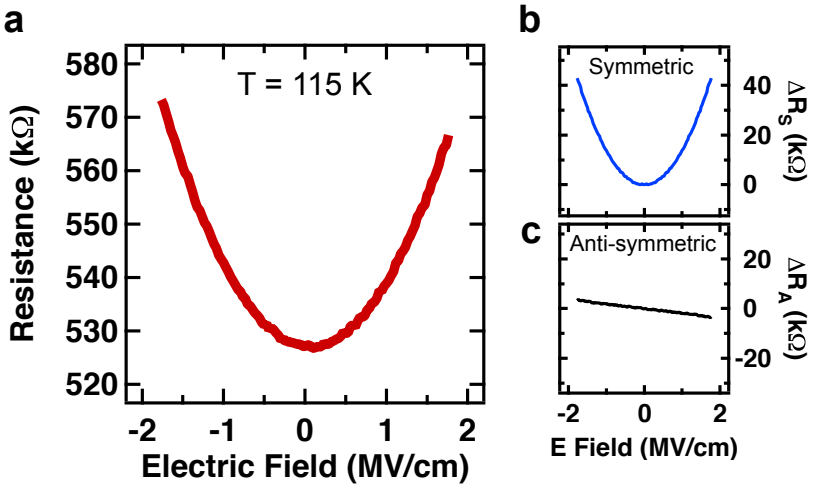

Figure 8.4: Electrostatic gate dependence of resistance. (a) Gate dependent resistance for Fe_3O_4 at a temperature of 115 K. (b) and (c) show the symmetric and anti-symmetric components of the gate dependent resistance change, respectively.

Fig. 8.4b and 8.4c, the symmetric part is up to 11 times larger than the anti-symmetric part. Because the change in carrier concentration is proportional to E (i.e. anti-symmetric), the small contribution of ΔR_A indicates that electric field control of the Verwey transition is not driven by a carrier concentration effect. Instead, a symmetric effect can be driven by other interactions with the electric field. The presence of an electric field will induce electric polarization given by $P = \chi_e E = (\kappa - 1)\epsilon_0 E$, where χ_e is the electric susceptibility, ϵ_0 is the permittivity of free space, and κ is the relative dielectric constant of Fe_3O_4. The induced polarization will produce an energy contribution $U = -\frac{1}{2}(PE) = -\frac{1}{2}(\kappa - 1)\epsilon_0 E^2$ that is symmetric in E. In addition, as Fe_3O_4 undergoes the Verwey transition, the dielectric constant changes sharply with κ being larger for the insulating state than for the metallic state $(\kappa_{ins} > \kappa_{metal})$ [148]. Thus, energy is lower for the insulating state than for the metallic state,

which stabilizes the low temperature insulating state and causes T_V to increase. Therefore, this provides a macroscopic explanation for an electric field effect that is symmetric in E and produces an increase in T_V, consistent with experimental results. Further theoretical work is needed, including a microscopic model that can provide an explanation for the magnitude of the effect. In addition, a contribution from electric field induced strain could generate this symmetry and should also be investigated [149].

8.5 Induced Magnetoelectric Effect

Since the Verwey transition in Fe_3O_4 is a correlated phase transition that couples both the charge and magnetic properties, it should be possible to tune magnetic properties with applied electric field. Figure 8.5a shows MOKE hysteresis loops measured at 113 K with

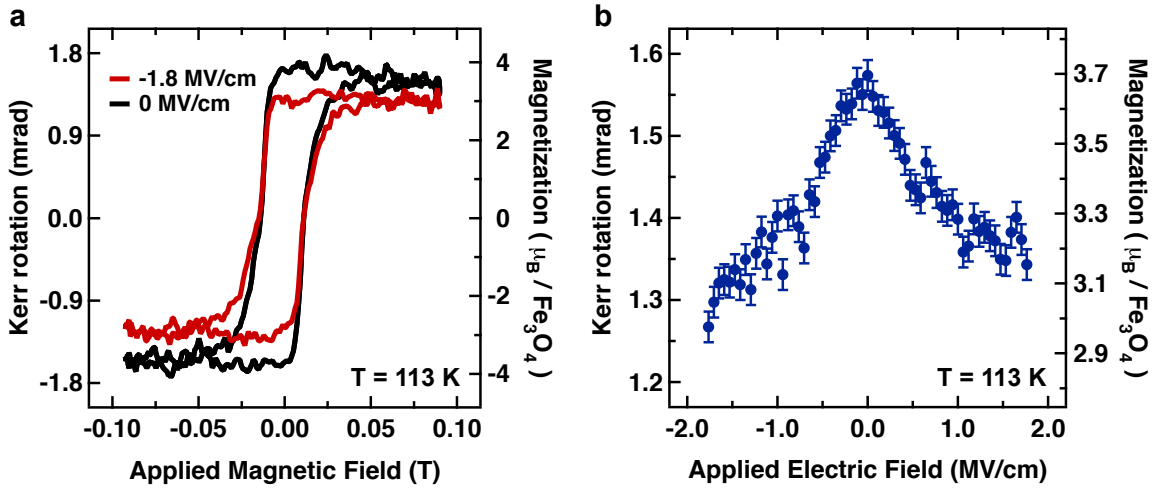

Figure 8.5: Electrostatic Gate Dependence of Magnetization in Fe_3O_4. (a) MOKE loops measured at 113 K with applied electric fields of 0 MV/cm (black) and -1.8 MV/cm (red), showing a decrease in magnetization with the application of an electric field. (b) Magnetization as a function of electric field, demonstrating a magnetoelectric effect induced by electric field control of the Verwey transition.

applied electric field of 0 MV/cm (black) and -1.8 MV/cm (red). The absolute magnetization is determined by SQUID measurements (right axis of Figure 8.5a). An electric field of -1.8 MV/cm causes a decrease in the saturation magnetization of 18%. Figure 8.5b displays the saturation magnetization as the electric field is swept between +1.8 MV/cm and -1.8 MV/cm. With the application of either positive or negative field, the magnetization decreases with a slightly stronger effect for negative fields. The magnetoelectric behavior is generated because the magnetization has strong temperature dependence below T_V (Figure 8.1d). When electric field is applied, the increase of T_V causes magnetization M to decrease because dM/dT is positive at T = 113 K; the intuitive picture is that the M vs T curve of Fig. 8.1d shifts in temperature as T_V increases. Thus, the decrease of magnetization for both positive and negative fields (with slightly stronger effect for negative fields) is consistent with the electric field dependence of T_V (Fig. 8.2b inset) and resistance (Fig. 8.4). The change in magnetization as a function of electric field is quantified by a magnetoelectric coefficient, $\alpha_{ME} = |\Delta M/\Delta E|$, where ΔM is the change in magnetization and ΔE is the change in electric field. Comparing the values at $E = 0$ MV/cm and $E = -1.8$ MV/cm yields a value of $\alpha_{ME} = 585 \pm 39$ pT m/V. Although at low temperatures, this is quite a large magnetoelectric coefficient compared to other materials shown below in Table 8.1. These results are compelling because they demonstrate a new method for generating magnetoelectric effects by controlling a correlated phase transition.

Table 8.1: Magnetoelectric coefficients for various material systems

Material	**Type**	$\lvert\alpha_{\mathbf{ME}}\rvert$ **(pT m / V)**	**Temp (K)**	**Ref.**
Cr_2O_3	Single-Phase	4.13	RT	[32, 146]
$Bi_5FeTi_3O_15$	Single-Phase	18.5	RT	[150]
$TbMn_2O_5$	Single-Phase	21	28 K	[151]
$LiCoPO_4$	Single-Phase	30.6	4.2 K	[27]
YIG	Single-Phase	$\sim$30	RT	[27]
$BiFeO_3$-$CoFe_2O_4$	Composite	31.8	RT	[147]
$TbPO_4$	Single-Phase	36.7	$\sim$1.3 K	[27]
Fe_3O_4	**Single-Phase**	**585**	**113 K**	**This Work**
$CoFe_2O_4$ / $BaTiO_3$	Composite	722	RT	[27]
LSMO / PZT	Composite	6500	100 K	[144]
PZT / Terfenol-D trilayer	Composite	65040	RT	[145]

8.6 Conclusion

In conclusion, we have demonstrated the electric field control of the Verwey transition in Fe_3O_4 thin films. An electric field stabilizes the charge-ordered insulating state causing the Verwey transition temperature to increase. By manipulating a correlated phase transition that combines both charge and magnetic transitions, we realize a large and novel magnetoelectric effect.

References

[2] F. Walz, J. Phys.: Condens. Matter **14**, R285 (2002).

[27] M. Fiebig, J. Phys. D: Appl. Phys. **38**, R123 (2005).

[32] X. He, Y. Wang, N. Wu, A. N. Caruso, E. Vescovo, K. D. Belashchenko, P. A. Dowben, and C. Binek, Nature Mater **9**, 579 (2010).

[106] J. J. I. Wong, L. Ramirez, A. G. Swartz, A. Hoff, W. Han, Y. Li, and R. K. Kawakami, Phys. Rev. B **81**, 094406 (2010).

[119] Y. Ding, D. Haskel, S. G. Ovchinnikov, Y.-C. Tseng, Y. S. Orlov, J. C. Lang, and H.-k. Mao, Phys. Rev. Lett. **100**, 045508 (2008).

[120] J. Garcia, G. Subias, J. Herrero-Martin, J. Blasco, V. Cuartero, M. C. Sanchez, C. Mazzoli, and F. Yakhou, Phys. Rev. Lett. **102**, 176405 (2009).

[121] D. J. Huang, H. J. Lin, J. Okamoto, K. S. Chao, H. T. Jeng, G. Y. Guo, C. H. Hsu, C. M. Huang, D. C. Ling, W. B. Wu, C. S. Yang, and C. T. Chen, Phys. Rev. Lett. **96**, 096401 (2006).

[122] J. E. Lorenzo, C. Mazzoli, N. Jaouen, C. Detlefs, D. Mannix, S. Grenier, Y. Joly, and C. Marin, Phys. Rev. Lett. **101**, 226401 (2008).

[123] G. K. Rozenberg, M. P. Pasternak, W. M. Xu, Y. Amiel, M. Hanfland, M. Amboage, R. D. Taylor, and R. Jeanloz, Phys. Rev. Lett. **96**, 045705 (2006).

[124] M. S. Senn, J. P. Wright, and J. P. Attfield, Nature **481**, 173 (2011).

[125] F. Zhou and C. Gerbrand, Phys. Rev. B **81**, 205113 (2010).

[126] E. J. W. Verwey, Nature **144**, 327 (1939).

[127] E. J. W. Verwey and P. W. Haayman, Physica **8**, 979987 (1941).

[128] V. A. M. Brabers, F. Walz, and H. Kronmuller, Phys. Rev. B **58**, 14163 (1998).

[129] C. H. Ahn, J. M. Triscone, and J. Mannhart, Nature **424**, 1015 (2003).

[130] A. Asamitsu, Y. Tomioka, H. Kuwahara, and Y. Tokura, Nature **388**, 50 (1997).

[131] S. Lee, A. Fursina, J. T. Mayo, C. T. Yavuz, V. L. Colvin, R. G. S. Sofin, I. V. Shvets, and D. Natelson, Nature Mater. **7**, 130 (2008).

[132] T. Lottermoser, T. Lonkai, U. Amann, D. Hohlwein, J. Ihringer, and M. Fiebig, Nature **430**, 541 (2004).

[133] H. Zheng, J. Wang, S. E. Lofland, Z. Ma, L. Mohaddes-Ardabili, T. Zhao, L. Salamanca-Riba, S. R. Shinde, S. B. Ogale, F. Bai, D. Viehland, Y. Jia, D. G. Schlom, M. Wuttig, A. Roytburd, and R Ramesh, Science **303**, 661 (2004).

[134] M. Alexe, M. Ziese, D. Hesse, P. Esquinazi, K. Yamauchi, T. Fukushima, S. Picozzi, and U. Gosele, Adv. Mater. **21**, 4452 (2009).

[135] J. van den Brink and D. I. Khomskii, J. Phys.: Condens. Matter **20**, 434217 (2008).

[136] G. T. Rado and J. M. Ferrari, Phys. Rev. B **15**, 290 (1977).

[137] K. Kato, S. Iida, K. Yanai, and K. Mizushima, J. Magn. Magn. Mater. **31-34**, 783 (1983).

[138] Y. Miyamoto, S. Ishihara, T. Hirano, M. Takada, and N. Suzuki, Solid State Comm. **89**, 51 (1994).

[139] Z. Zhang and S. Satpathy, Phys. Rev. B **44**, 13319 (1991).

[140] P. Seneor, A. Fert, J. L. Maurice, F. Montaigne, F. Petro, and A. Vaures, Appl. Phys. Lett. **74**, 4017 (1999).

[141] Y. Li, W. Han, A. G. Swartz, K. Pi, J. J. I. Wong, S. Mack, D. D. Awschalom, and R. K. Kawakami, Phys. Rev. Lett. **105**, 167203 (2010).

[142] W. Eerenstein, T. T. M. Palstra, T. Hibma, and S. Celotto, Phys. Rev. B. **66**, 201101(R) (2002).

[143] F. Wang, C.-H. Li, T. Zou, L. Yi, and Y. Sun, J. Phys.: Condens. Matter **22**, 496001 (2010).

[144] C. A. F. Vaz, J. Hoffman, Y. Segal, J. W. Reiner, R. D. Grober, Z. Zhang, C. H. Ahn, and F. J. Walker, Phys. Rev. Lett. **104**, 127202 (2010).

[145] J. Ryu, A. V. Carazo, K. Uchino, and H.-E. Kim, Jpn. J. Appl. Phys. **40**, 4948 (2001).

[146] J. Ryu, S. Priya, K. Uchino, and H.-E. Kim, J. Electroceram. **8**, 107 (2002).

[147] L. Yan, Z. Wang, Z. Xing, and J. Li, J. Appl. Phys. **107**, 064106 (2010).

[148] A. Pimenov, S. Tachos, T. Rudolf, A. Loidl, D. Schrupp, M. Sing, R. Claessen, and V. A. M. Brabers, Phys. Rev. B **72**, 035131 (2005).

[149] Y. Nagasawa, M. Kosaka, S. Katano, N. Mori, S. Tado, and Y. Uwatoko, J. Phys. Soc. Jpn. **76**, 110 (2007).

[150] S. Suryanarayana, Bull. Mater. Sci. **17**, 1259 (1994).

[151] N. Hur, S. Park, P. A. Sharma, J. S. Ahn, S. Guha, and S.-W. Cheong, Nature **429**, P392 (2004).

Chapter 9

Conclusion

In Conclusion, this thesis has shown many different ways of controlling magnetism at the nanoscale. By utilizing MBE synthesis, we are able to highly control the various materials grown throughout the studies. We showed that by modifying the Fe/MgO interface through controlled oxidation in the Fe/MgO/Fe systems, we can induce a higher order Biquadratic coupling between the Fe layers [24]. Second, we then placed Fe nanoclusters within the MaO barrier and showed that the bilinear coupling and be tuned by the location of the Fe nanoclusters. We also showed that the materials dependent coupling between a thin film and nanoclusters is enhanced when compared to analogous thin film systems [106]. Next, we investigate the initial growth modes and the role of interfacial electrostatic interactions of EuO epitaxy on MgO(001) by reactive molecular beam epitaxy. We found that electrostatic interactions played a important role in the epitaxial growth of EuO on MgO and can be treated by using a TiO_2 electrostatic template on MgO. The TiO_2 layer allows for substrate assisted

oxidation to form EuO, leading to ultrathin ferromagnetic EuO films normally not observed with direct growth of EuO on MgO [152]. The second half of the thesis focused on electric field control of magnetism and here we showed that electric fields can tune the perpendicular magnetic anisotropy in the MgO/Fe/Ag system on MgO (001). Finally, we investigate the electrical gating effects inside the highly correlated system of Fe_3O_4. We developed a recipe for rMBE growth of high quality magnetite on MgO(001). We demonstrated the electric field control of the Verwey transition and show electric fields stabilizes the charge-ordered insulating state causing the Verwey transition temperature to increase. By using electric fields to tune a correlated phase transition, we realize a large and novel magnetoelectric effect on Fe_3O_4 [118].

References

[24] Y. F. Chiang, J. J. I. Wong, X. Tan, Y. Li, K. Pi, W. H. Wang, H. W. K. Tom, and R. K. Kawakami, Phys. Rev. B **79**, 184410.

[106] J. J. I. Wong, L. Ramirez, A. G. Swartz, A. Hoff, W. Han, Y. Li, and R. K. Kawakami, Phys. Rev. B **81**, 094406 (2010).

[118] J. Wong, A. Swartz, R. Zheng, W. Han, and R. Kawakami, Physical Review B **86**, 060409 (2012).

[152] A. Swartz, J. Wong, I. Pinchuk, and R. Kawakami, Journal of Applied Physics **111**, 083912 (2012).

Appendix A

The Magnetism Cheat Sheet

In cgs units

$$B = (H + 4\pi M) \tag{A.1}$$

where B is the magnetic induction (gauss, G), H is the magnetic field intensity (Orested, Oe) and M is the volume magnetization (emu/cm^3).

In SI units

$$B = \mu_\circ (H + M) \tag{A.2}$$

where B is the magnetic induction measured in Tesla (T) or Wb/m^2, H is the magnetic field intensity and M is the volume magnetization measured in (Amperes / meter, A/m). Sometimes, $B = \mu_\circ(H + M)$ is written as $B = \mu_\circ H + M$, meaning that M in this case has the units of T. $\mu_\circ$ is the magnetic permeability of free space.

$\mu_\circ = 4\pi \times 10^{-7}$ Vs/(Am)$\approx 1.257 \times 10^{-6}$ H/m or N/A^2 or T·m/A or Wb/(A·m)

Table A.1: Magnetism Unit Conversion Table

Quantity	**Symbol**	**cgs units** $B = H + 4\pi M$	**Conversion Factor, C** (SI)=C×(cgs)	**Si Units** $B = \mu_\circ(H + M)$ $\mu_\circ/4\pi = 10^{-7}$ H/m
Magnetic Induction	B	gauss (G)	10^{-4}	tesla (T) Wb/m^2
Magnetic Flux	Φ	G cm^2 Maxwell (Mx)	10^{-8}	weber (Wb)
Magnetic Field Intensity (Auxiliary magnetic field)	H	Oersted (Oe)	$10^3/4\pi$	A/m
Magnetic Moment	m	emu, erg/Oe	10^{-3}	A-m^2, J/T
(Volume) Magnetization	M	emu/cm^3	10^3	A/m
	4πM	G	$10^3/4\pi$	A/m
Mass Magnetization	M$_g$	emu/g	1 $4\pi \times 10^{-7}$	A-m^2/kg Wb-m/kg
Volume Susceptibility	χ	dimensionless	4π	dimensionless
Permeability	μ	dimensionless	$4\pi \times 10^{-7}$	Wb/A-m

A.1 Magnetic Moments and Magnetization, cgs units

A magnetic moment is denoted as

$$\mu \text{ (emu = erg/Oe)} \tag{A.3}$$

and the magnetization is the sum of all magnetic moments divided by the volume of the material, that is

$$M = \frac{\sum \mu_i}{V} \text{ (erg/Oe} \cdot \text{cm}^3 \text{ or emu/cm}^3\text{)} \tag{A.4}$$

Specific magnetization is the magnetic moments per mass

$$M_g = \frac{\sum \mu_i}{\text{mass}} = \frac{\sum \mu_i}{\rho V} = \frac{M}{\rho} \text{ (emu/g)} \tag{A.5}$$

The atomic (magnetic dipole) moment measured in Bohr Magneton is

$$\mu_B = \frac{eh}{4\pi m_e c} = 0.927 \times 10^{-20} \text{ erg/Oe or emu} \tag{A.6}$$

where e is the elementary charge, h is Planks constant, m_e is the rest mass of an electron and c is the speed of light.

Atomic moment, ordered moment

$$\mu = -\gamma \hbar \mathbf{J} = -g\mu_B \mathbf{J} \tag{A.7}$$

where **J** is the total angular momentum of the atomic ground state, γ is the atomic gyromagnetic ratio and g is the landé g-factor, $g = 1 + \frac{J(J+1)+S(S+1)-L(L+1)}{2J(J+1)}$.

A.2 Magnetic Susceptibility and Permeability

The magnetic susceptibility, χ, is a dimensionless proportionality constant that indicates the degree of magnetization of a material when subjected to an applied magnetic field. The

susceptibility is given by

$$\chi = \frac{M}{H} \tag{A.8}$$

and for materials with an linear response, $M = \chi H$, leads to

$$B = (H + 4\pi M) = (1 + 4\pi\chi)H \qquad \text{(in cgs)} \tag{A.9}$$

The magnetic permeability, μ, is the measure of the ability of a material to support the formation of a magnetic field within itself. The Auxiliary magnetic field, H represents how an applied magnetic field B influences the organization of magnetic dipoles in a given medium. Its relation to permeability is

$$\mu = \frac{B}{H} \tag{A.10}$$

and the permeability can be related to susceptibility by

$$\mu = 1 + 4\pi\chi \tag{A.11}$$

and in cgs units, both χ and μ are dimensionless units. Depending on the material, the values of χ and μ can vary.

Table A.2: Magnetism Unit Conversion Table

Material	χ	μ
Vacuum	0	1
Diamagnetic	<0 and small	slightly < 1
Paramagnetic	>0 and small	slightly > 1
Antiferromagnetic	>0 and small	slightly > 1
Ferromagnetic	$\gg 0$ and small	$\gg 0$ and history dependent

A.3 Diamagnetism and Paramagnetism

Diamagnetism appears in all materials, and is the tendency of a material to oppose an applied magnetic field, and therefore, to be repelled by a magnetic field. It is characterized by a weak, negative magnetic susceptibility, and very small permeability. It is due to the

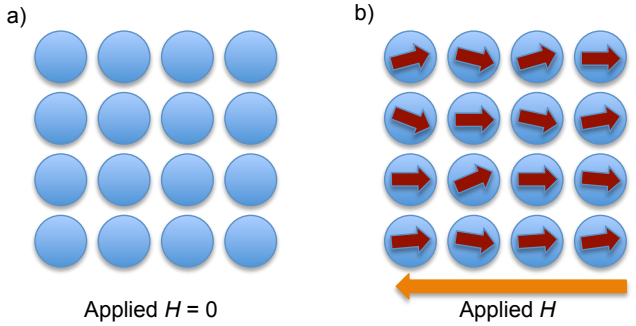

Figure A.1: Schematic for the Magnetization in Diamagnetic Materials

non-cooperative behavior of orbiting electrons when exposed to an applied magnetic field. Diamagnetic substances are composed of atoms which have no net magnetic moments (ie., all the orbital shells are filled and there are no unpaired electrons), so the intrinsic electron magnetic moments cannot produce any bulk effect. Thus, when a magnetic field is applied to

the material, a negative magnetization arises from the electrons' orbital motion [153]. Typical χ for a diamagnetic material is usually on the order of -10^{-5}.

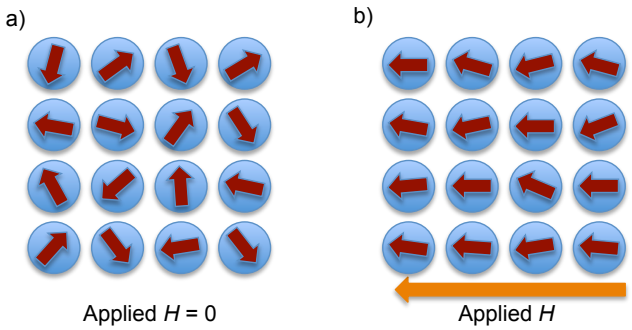

Figure A.2: Schematic for the Magnetization in Paramagnetic Materials

Paramagnetism is the magnetic material response to an applied field, having a small mall, positive susceptibility to the magnetic field. The material will be slightly attracted by the applied field and produce a small magnetization within the material. Paramagnetic materials have atoms or ions and each of these have a magnetic moment due to unpaired electrons in partially filled orbitals. This effect occurs due to the quantum mechanical spin and orbital angular momentum of the electron. Without an applied magnetic field, these magnetic moments point in random directions because there is a very weak interaction between magnetic moments of neighboring atoms and thermal fluctuations. In the presence of an applied field, these moments then align parallel with the applied field and the degree of the induced magnetization depends on the strength of the applied field However, due to the weak interaction between the moments, the material will not retain the magnetic any magnetic ordering once a magnetic field is turned off much like Diamagnetic materials [153]

Diamagnetics		*Paramagnetics*	
Material	***Susceptibility χ_m (volume) (SI units)***	***Material***	***Susceptibility χ_m (volume) (SI units)***
Aluminum oxide	-1.81×10^{-5}	Aluminum	2.07×10^{-5}
Copper	-0.96×10^{-5}	Chromium	3.13×10^{-4}
Gold	-3.44×10^{-5}	Chromium chloride	1.51×10^{-3}
Mercury	-2.85×10^{-5}	Manganese sulfate	3.70×10^{-3}
Silicon	-0.41×10^{-5}	Molybdenum	1.19×10^{-4}
Silver	-2.38×10^{-5}	Sodium	8.48×10^{-6}
Sodium chloride	-1.41×10^{-5}	Titanium	1.81×10^{-4}
Zinc	-1.56×10^{-5}	Zirconium	1.09×10^{-4}

Figure A.3: A table magnetic susceptibility for various materials adapted from Ref. [154]

A.4 Ferromagnetism

Ferromagnetism are a class of materials that usually what other consider to be ”magnetic”. These materials possess a permanent magnetic moment in the absence of an external field, and manifest very large and permanent magnetizations. Some well-known ferromagnetic materials that exhibit easily detectable magnetic properties (to form magnets) are nickel, iron, cobalt, gadolinium and their alloys. A ferromagnetic material, like a paramagnetic substance, has unpaired electrons and in addition to the electrons' intrinsic magnetic moment's, a long-range ordering between magnetic moments. This long-range effect is generally due to the exchange interactions between moments. The exchange interaction between the moments causes them to orient parallel to each other to maintain a lowered-energy state and the moment will maintain this arrangements in the presence and absence of a magnetic field. There are two distinct characteristics of a ferromagnetic material. First, spontaneous magnetization and the existence of, and the second is a magnetic ordering temperature. The spontaneous magnetization is the net magnetization that is inside a magnetized volume in the absence

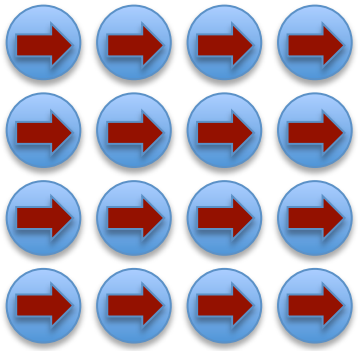

Figure A.4: Schematic for the Magnetization in Ferromagnetic Materials

of a field. The magnitude of this magnetization, at 0 K, is dependent on the spin magnetic moments of electrons. A related term is the saturation magnetization (M_S), which is the maximum induced magnetic moment that can be obtained in a magnetic field (H_{sat}) and further application of larger fields will yield no increase in magnetization. The difference between spontaneous magnetization and M_S has to do with the magnetic domains within a material (more on this below). M_S is an intrinsic property and is independent of the size of the material but does depend on temperature.

Every ferromagnetic substance has its own individual temperature, called the Curie temperature, or Curie point, above which it loses its ferromagnetic properties. Even though there are very strong interactions between the magnetic moments, thermal energy will eventually overcomes the exchange and produces a randomizing effect. This occurs at a the Curie temperature (T_C). Below the Curie temperature, the ferromagnet is ordered and above it, disordered. The M_S goes to zero at the Curie temperature. A illustrative plot in figure A.5a shows a typical temperature dependence of M in a ferromagnetic material. The red curve is

M vs T with a critical temperature at T_C. To first order, the temperature dependence of the magnetization at low temperatures is given by Bloch's Law

$$M(T) = M(0)(1 - BT^{\frac{3}{2}} + ...) \tag{A.12}$$

where M_O is the magnetization at 0 K, B is a coefficient (units of $K^{-3/2}$) and T is temperature in kelvin. As the temperature is increased, the magnetization of goes as $\sim (1 - T/T_C)^{\beta}$, where β is a critical exponent that depends on composition (Fe$\sim$0.34). Figure A.5b illustrates the effects on the magnetization temperature dependence in the presence of an applied magnetic field ($H_2 > H_1$). A related temperature dependence is the Curie-Weiss law, which describes the magnetic susceptibility of a ferromagnetic material above T_C,

$$\chi = \frac{C}{T - T_C} \tag{A.13}$$

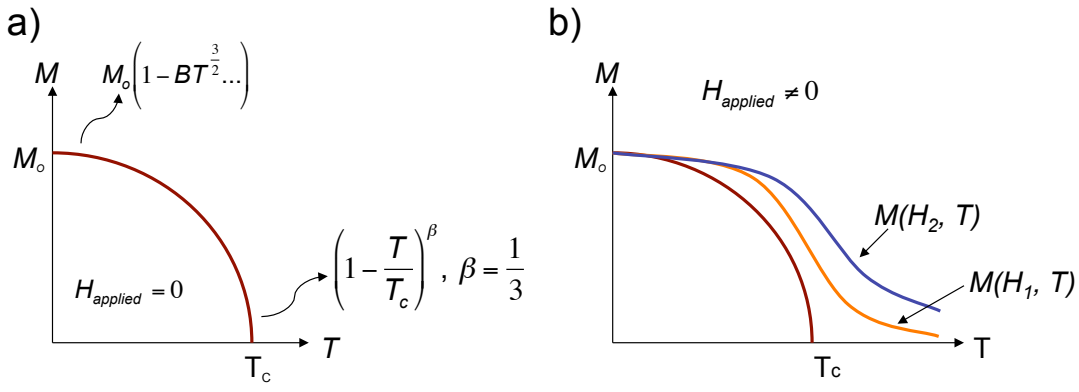

Figure A.5: Schematic M_S vs T curve - Bloch's law a) An illustration of M_S vs T for $H = 0$ and b) for $H \neq 0$

A.5 Domains and Hysteresis

Within ferromagnetic or ferrimagnetic material that is at a temperature below T_C, small regions comprised of parallel magnetic moments are formed as shown in figure A.6. Such a region is called a domain, and each one is magnetized to its saturation magnetization. Domains walls or boundaries separate each of these domains and magnetization gradually changes across one of these domain walls [154]. At long distances, the exchange energy

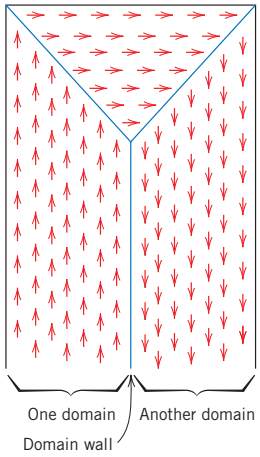

Figure A.6: Illustration of Domains from Ref. [154] Schematic depiction of domains in a ferromagnetic or ferrimagnetic material; arrows represent atomic magnetic dipoles.Within each domain, all dipoles are aligned, whereas the direction of alignment varies from one domain to another [154].

between magnetic moments is overtaken by the classical tendency of dipoles to anti-align. This is why in a ferromagnetic material in equilibrium; the dipoles in the whole material are not aligned. Rather, they organize into magnetic domains that have moments that are aligned at short range, but at long range adjacent domains are anti-aligned [153]. Domains are microscopic in size, so typically, a ferromagnetic (and ferrimagnetic) materials has many domains and all have a different magnetization orientations. Therefore, M is the total vector

sum of all the magnetizations of all domains. For samples that have not experienced an applied H field usually have a magnetization of zero.

The existence of domains helps explain the reason why some ferromagnetic specimens can attain saturation magnetization of the whole sample with the use of a relatively weak applied magnetic field [153]. This effect within the ferromagnetic materials is due to the fact that the applied field does not have to order the magnetic moments macroscopically. The moments within the domain are already ordered, so the applied field needs to merely align the domain moment. The domains also gives rise to the phenomenon of the ferromagnetic materials having a spontaneous magnetization[153].

The question arises though, It cost energy to create a domain wall and so it should raise the question why domains would form at all? The answer is that the formation of domain walls saves energy associated with the dipolar field of the magnetic moments [153]. If we take the equation $\nabla \cdot H = -\nabla \cdot M$ and look at when M stop and starts, at the edges of the sample, the magnetic field diverges. The result of this is that there is a demagnetization field that fills space at a cost of energy $B^2/2\mu_o$ or J/m^3 (SI units). The dipole energy can be saved if the sample brakes up into domains. The energy of a domain wall is given by,

$$E_W = 2\pi\sqrt{AK_u} \tag{A.14}$$

where $A = JS^2/a$, the exchange stiffness with units of energy/length, a is the lattice constant and K_u is the magnetocrystalline anisotropy (MCA). The domain wall thickness d is given

by of $d = \pi\sqrt{A/K_u}$. It cost energy to create a domain wall so the formation of the domain walls are balanced between the cost of the demagnetization field and the cost of the domain wall or the balancing of the exchange energy and the dipole energy. Figure A.7 shows three

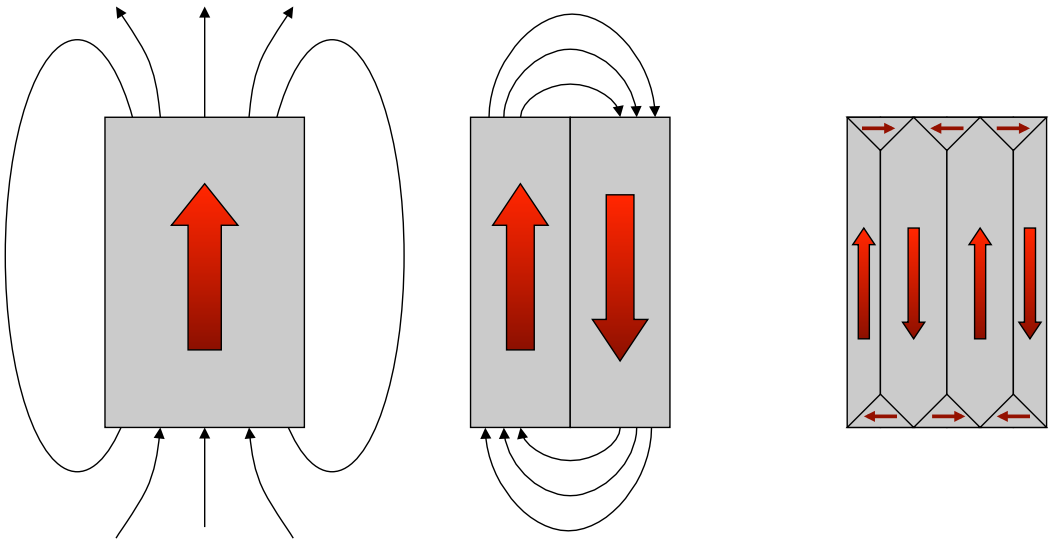

Figure A.7: Schematic of domains and fringe fields. Left represents a single domain, middle is a AF domain alignment, and right is a full domain state.

different illustrated choices for a domain structure in a FM material. The first is a single domain in which it has no domain walls and single orientation of its magnetization. The dipole energy of a single domain is quite large compared to the others. In order to reduce its dipole energy, it will break up into domains. The closure domain structure eliminates the dipole energy but at the cost of introducing a number of domain walls [153]. A closure domain structure is characterized by the closed magnetic flux circuit and having no magnetic flux leakage outside of the sample (right diagram in fig. A.7) [117].

When a material is ”fresh”, meaning it has not experience an magnetic field before, it will typical have no net magnetization. The FM material can be place in a magnetometer

where the magnetization is measured as a function of applied H. In Ref. [154] has a great illustration of what happens in the FM when measuring the "virgin" curve, seen in figure asdfas. Figure A.8 point U show that material is made up many domains causing it to have

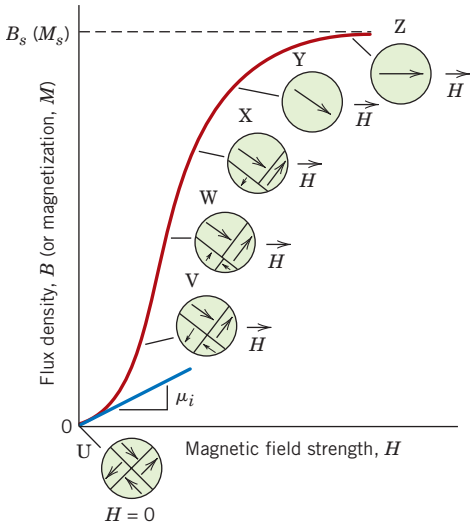

Figure A.8: The M_S vs. H behavior for a FM or ferrimagnetic material that was initially unmagnetized. Domain configurations during several stages of magnetization are represented by U, V, W, X, Y, Z. [154]

no net magnetic moment. As the external is applied, the domains that are oriented in the direction that is the most energy favorable, that is aligned with H, will grow at the expense to domains that are not in energy favorable directions (V through X). As the field strength is increased further, unfavorable domains are annihulated and the material is essentially a single domain that is nearly align with the field (Y). Once the field is increased further, the domain magnetization will align with the field and M_S is achieved [154].

Because the sample is ferromagnetic and will retain a magnetization with no applied field, the reversal curve will not track back onto the initial magnetization curve. A hysteresis effect, thus hysteresis loop, is produced in which the M lags behind the applied H field, or

decreases at a lower rate. Figure A.9 shows an schematic of a magnetic hysteresis loop. Say

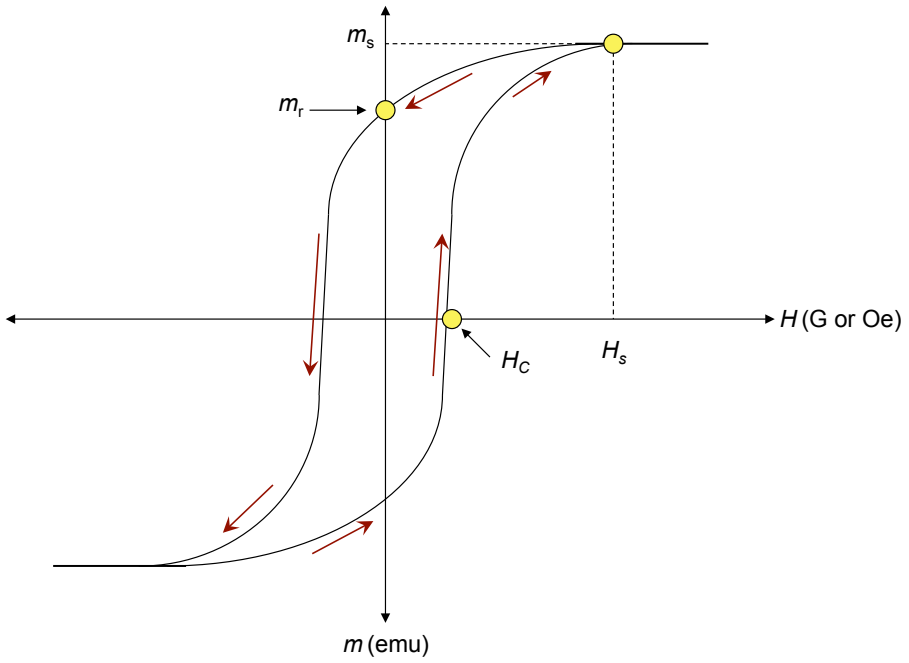

Figure A.9: Schematic m vs H Hysteresis Loop. Points H_S is the saturation field, m_S is the saturation moment, m_R is the remanence and H_C is the coercivity.

we are at positive saturation and the H field direction then decreased in strength. The domain structure process will begin to reverse as shown in figure **??**, but with changes. First, there is a rotation of the single domain with the reversed field. Next, small domains will start to form and the domains having magnetic moments align with the direction of how the field is changing (negative direction). These smaller domains will grow a little, annihilating some of the previous domains that were aligned at H_S. This happens at a slower rate then before, thus m will lag H, because of the resistance to movement of domain walls that occurs in response to the increase in magnetic field in the negative direction. When the applied field reaches zero, there is still some, if not most, domains oriented in the positive directions still remain, resulting in the sample having a magnetic remanence (m_R). As the field is applied in

the negative direction, the domains that are now align with the negative field will grow faster and faster. At some negative field, there will be no net magnetic moment and this is known as the coercivity, H_C. The coercive field is the amount of negative field needed to have no net moment in the sample. H_C is the measure of how "hard" a magnetic is, the larger H_C is, the harder the magnetization to switch directions. Once the field is applied slightly pass H_C, the sample's magnetization switch to the negative direction quickly. Basically, the favorable domains annihilate the others quite fast. From the negative saturation, the field can then be reversed and the process begins again, resulting in a Hysteresis loop. The m vs H hysteresis loop is the most important tool to use to characterize a magnetic material.

A.6 Antiferromagnetism

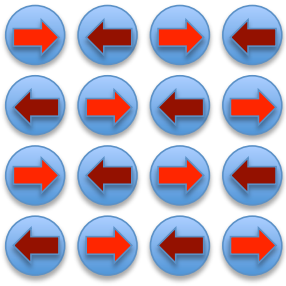

Figure A.10: Schematic for Antiferromagnetism.

The phenomenon of exchange coupling between magnetic moments of adjacent atoms occurs in other materials, not just in ferromagnetic materials. One such group has a coupling that causes antiparallel alignments between adjacent magnetic moments. This alignment of the spin moments of neighboring atoms in exactly opposite directions is termed antiferromag-

netism (AF). A classic example of a antiferromagnetic material is Manganese oxide (MnO). MnO is a rock salt material much like MgO, being composed of Mn ions and O ions. In this

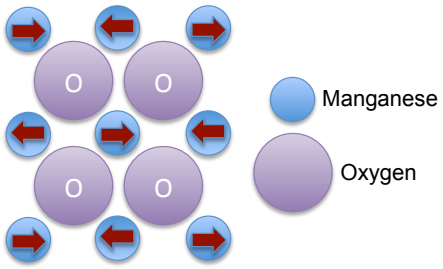

Figure A.11: Schematic of the Antiferromagnetic MnO. The blue spheres are Mn and Purple are the oxygens. The red arrows represent the magnetic moments of the Mn.

structure, O ions have no net magnetic moment but the Mn does. The magnetic moments between adjacent Mn ions interact through the oxygen ion due to an exchange coupling called superexchange [117, 153, 154]. This interaction cause the moments to align anitparallel causing the material to have no net magnetization. Because AF is an order magnetism, it has a critical temperature know as the Néel temperature (T_N), which above the material is paramagnetic. However, sometimes varying temperatures can cause the antiferromagnets to exhibit diamagnetic and ferrimagnetic properties. Antiferromagnets are less common compared to the other types of behaviors, many transition metal oxides exhibit AF (i.e. NiO, CoO, FeO) and are mostly observed at lower temperatures.

A.7 Ferrimagnetism

In ionic compounds, such as oxides, more complex forms of magnetic ordering can occur as a result of the crystal structure. One type of magnetic ordering is call ferrimagnetism.

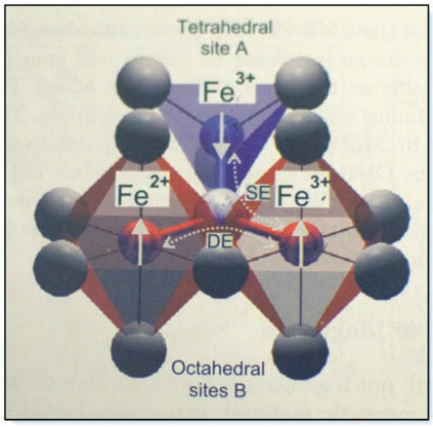

Figure A.12: The presence of both double exchange and superexchange in Fe_3O_4 adapted from reference [117].

Like ferromagnetism, ferrimagnets retain their magnetization in the absence of a field. However, like antiferromagnets, neighboring pairs of magnetic moments like to point in opposite directions. These two properties are not contradictory, because in a lattice such as Fe_3O_4, the magnetic moments are arranged in such there is more moment pointing in one direction than the opposite direction. In figure A.12, shows the exchange that causes the ferrimagnetic alignment for one unit of Fe_3O_4. Essential, we have to moments pointing up and only one pointing down and this can be viewed as the most simple explanation of ferrimagnetism. Another way ferrimagnetism can come about is through an superexchange between two sub lattices with different magnetic moment sizes. The magnetic structure is composed of two magnetic sublattices (called A and B) separated by oxygens and the resulting superexchange interactions causes antiparallel alignment of spins between the A and B sublattice. Since A and B sublattices are not equal and result in a net magnetic moment.

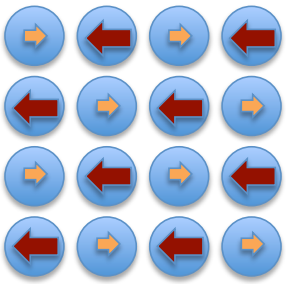

Figure A.13: Ferrimagnetism schematic.

Ferrimagnetism is therefore similar to ferromagnetism. It exhibits all the of ferromagnetic behavior; spontaneous magnetization, Curie temperatures, hysteresis, and remanence. However, ferromagnetic and ferrimagnetic materials have very different magnetic ordering.

A.8 Anisotropy

Anisotropy means that a property is to be directionally dependent. Therefore for a magnetic anisotropy means that the magnetization has a preference to lie in a particular direction, known as the easy axis. The magnetic anisotropy is defined as the energy to rotate the magnetization direction from the easy axis direction to the hard axis direction. The energy equation of anisotropy is given by

$$E_{MA} = K_1 \sin^2\theta + K_2 \sin^4\theta + ... \tag{A.15}$$

Where K_i are the anisotropy constants, θ is the angle from the unique axis (depends on what is easiest to define) and the units for $E_M A$ is energy/volume. We can define the zero for a

unique axis as normal to a thin film sample and then anisotropy field (H_ani) is then given by

$$H_{ani} = \frac{2K_1}{M}\cos\theta \tag{A.16}$$

where M is the saturation magnetization and K_1 is the sum of two anisotropy constants, K_{MCA} and K_S. K_{MCA} is the magnetocrystalline anisotropy and K_S is the Magnetic shape anisotropy. This the case of θ=0 is out of plane, $K_1 > 0$ says the easy axis is out of plane and $K_1 < 0$ means the easy axis is in-plane.

Materials with high magnetic anisotropy usually have high coercivity; that is they are hard to demagnetize. These are called "hard" ferromagnetic materials and are typically used in permanent magnets. It takes much more applied H field, thus energy, to switch the magnetizations of these materials. On the other hand, materials with low magnetic anisotropy usually have low coercivity, their magnetization is easy to change. These are called "soft" ferromagnets and such an example is permalloy, an alloy of $Fe_{20\%}Ni_{80\%}$.

A.8.1 Shape Anisotropy

The shape anisotropy (K_S) is due to the fact that there is a demagnetization field that needs to be over come before saturation. For materials that $M \neq 0$, the field within the material, H, differs from the applied field H. For a general ellipsoid shaped sample: B, H, and $M$are uniform inside. $H' = H - DM$, where D is the demagnetization factor. The demagnetization factor will vary from 0 D 4π. For a thin films or a disk, figure A.15 show

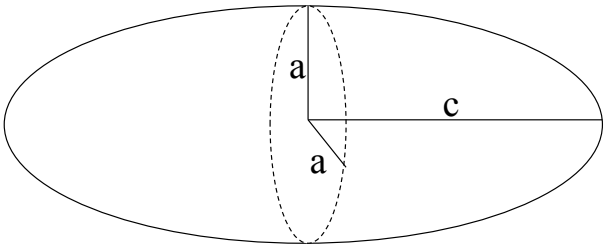

Figure A.14: Shape anisotropy axis definitions

the shape anisotropy for a plane or thin film. Figure A.16 show the shape anisotropy of for a sphere and Figure A.17 show the shape anisotropy of for a wire or a rod shape.

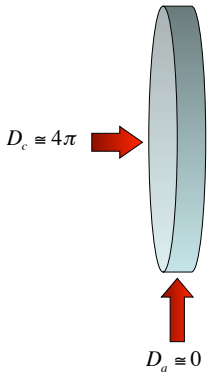

Figure A.15: Shape anisotropy for a disk or plane (c << a)

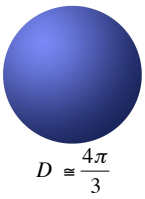

Figure A.16: Shape anisotropy for a sphere (c = a)

Basically, since $H' = H - DM$, the difference in an applied H field needed to saturate the material in one direction versus another is DM. So for a wire, the ΔH in H_S for field parallel versus perpendicular is approximately $2\pi M$.

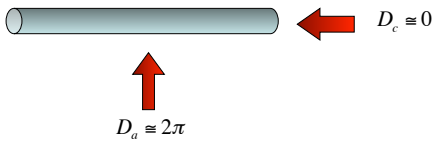

Figure A.17: Shape anisotropy for a wire or rod. (c >> a)

A.8.2 Magnetocrystalline Anisotropy

Magnetocrystalline anisotropy (MCA) is the magnetization dependence of the internal energy of a ferromagnetic material. In a crystal lattice, certain directions are the magnetization easy axes. Typically, a BCC lattice has an easy axis along the (100) directions, FCC its the (111) axis and hexagonal is the c-axis. The strength of the MCA is dependent on the crystallinity of the material and the over all anisotropy of the material is a competition between MCA and Shape anisotropy. The source of the of MCA is the anisotropy of the atomic structure and

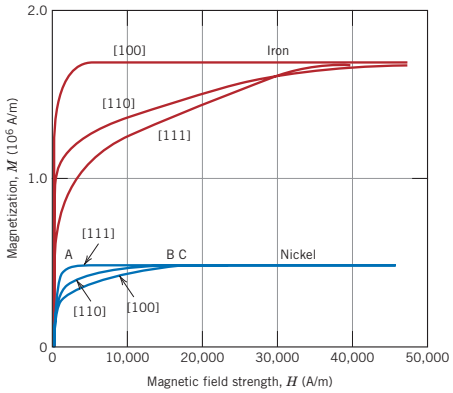

Figure A.18: Adapted from [154]. M vs H for Fe and Nickel.

bonding in conjunction with the spin orbit interaction between lattice sites. For an example, single crystal Fe the easy axis is along the [100] direction of the lattice, and the hard axis is along the [110] axis. For Nickel, the easy axis is along long the [111] directions and [100] is

the hard axis. Figure A.18 shows the magnetization, in different directions, as a function of H. [117, 154]. For more information, I suggest reading references [117, 153, 154].

Appendix B

Pair-wise coupling model

For the FM/MgO/FM system with FM nanoclusters embedded in the spacer, the energy equation of the system is

$$\begin{aligned} E &= -J_{\textit{Hard-Free}}\cos(\theta_H-\theta_F) - J_{\textit{Free-NC}}\cos(\theta_F-\theta_{NC}) - J_{\textit{Hard-NC}}\cos(\theta_H-\theta_{NC}) \\ &\quad + K_H t_H \cos^2(\theta_H)\sin^2(\theta_H) + K_F t_F \cos^2(\theta_F)\sin^2(\theta_F) \\ &\quad + K_{NC} t_{NC} \cos^2(\theta_{NC})\sin^2(\theta_{NC}) \end{aligned} \tag{B.1}$$

where θ_H, θ_F, θ_{NC} are the in-plane magnetization angle relative to the applied field direction for the hard layer, free layer, and NC, respectively, and $K_H(t_H)$, $K_F(t_F)$, $K_{NC}(t_{NC})$ are the corresponding anisotropy (thickness), respectively. The anisotropy parameters are the assumed to be positive, which is the case for Fe and bcc Co. Also, note that $J < 0$ denotes

antiferromagentic coupling and $J > 0$ denoted ferromagnetic coupling. Assuming that the magnetization of the hard layer is fixed ($\theta_H = 0°$) leads to

$$\begin{aligned} E &= -J_{\textit{Hard-Free}} \cos(\theta_F) - J_{\textit{Free-NC}} \cos(\theta_F - \theta_{NC}) - J_{\textit{Hard-NC}} \cos(\theta_{NC}) \\ &\quad + K_F t_F \cos^2(\theta_F) \sin^2(\theta_F) + K_{NC} t_{NC} \cos^2(\theta_{NC}) \sin^2(\theta_{NC}) \end{aligned} \tag{B.2}$$

Next, we assume that $K_F(t_F) >> J_{\textit{Hard-Free}}$ so that the only stable magnetization angles for the free layer is $\theta_F = 0°, 90°, 180°, 270°$. For the bilinear coupling, we only take $\theta_F = 0°$ and $180°$ leading to

$$\begin{aligned} E(\theta_F = 0°) &= -J_{\textit{Hard-Free}} - J_{\textit{Free-NC}} \cos(\theta_{NC}) \\ &\quad - J_{\textit{Hard-NC}} \cos(\theta_{NC}) + K_{NC} t_{NC} \cos^2(\theta_{NC}) \sin^2(\theta_{NC}) \end{aligned} \tag{B.3}$$

$$\begin{aligned} E(\theta_F = 180°) &= J_{\textit{Hard-Free}} + J_{\textit{Free-NC}} \cos(\theta_{NC}) \\ &\quad - J_{\textit{Hard-NC}} \cos(\theta_{NC}) + K_{NC} t_{NC} \cos^2(\theta_{NC}) \sin^2(\theta_{NC}) \end{aligned} \tag{B.4}$$

and total J_1 for the system is given by,

$$J_1 = \frac{E(\theta_F = 180°) - E(\theta_F = 0°)}{2} \tag{B.5}$$

Now, minimizing Eqs. (B.3) and (B.4), $dE/d\theta_{NC} = 0$, we find that $\theta_{NC} = 0^\circ$ or 180°. Therefore the minimum energies given by Eqs. (B.3) and (B.4) are

$$E(\theta_F = 0^\circ, \theta_{NC} = 0^\circ) = -J_{\textit{Hard-Free}} - J_{\textit{Free-NC}} - J_{\textit{Hard-NC}} \tag{B.6}$$

$$E(\theta_F = 0^\circ, \theta_{NC} = 180^\circ) = -J_{\textit{Hard-Free}} + J_{\textit{Free-NC}} + J_{\textit{Hard-NC}} \tag{B.7}$$

and

$$E(\theta_F = 180^\circ, \theta_{NC} = 0^\circ) = J_{\textit{Hard-Free}} + J_{\textit{Free-NC}} - J_{\textit{Hard-NC}} \tag{B.8}$$

$$E(\theta_F = 180^\circ, \theta_{NC} = 180^\circ) = J_{\textit{Hard-Free}} - J_{\textit{Free-NC}} + J_{\textit{Hard-NC}} \tag{B.9}$$

Looking at Eq. (B.6), the free layer, hard layer and NC are a coupled ferromagnetic (FM) ($J > 0$) whereas in the case of Eq. (B.7), the free layer and hard layer are coupled FM but the NC are coupled antiferromagnetic (AF) to both the free and hard layers ($J < 0$). For both cases of Eqs. (B.8) and (B.9), the free layer and hard layer are coupled AF but in Eq. (B.8), the NC are coupled AF to the free layer and FM coupled to the hard layer, whereas the opposite is true for Eq. (B.9). Thus, we can combine Eqs. (B.6) and (B.7) and the lower value of E yields

$$E(\theta_F = 0^\circ) = -J_{\textit{Hard-Free}} - |J_{\textit{Free-NC}} + J_{\textit{Hard-NC}}| \tag{B.10}$$

and for Eqs. (B.8) and (B.9)

$$E(\theta_F = 180^\circ) = J_{\textit{Hard-Free}} - |J_{\textit{Free-NC}} - J_{\textit{Hard-NC}}| \tag{B.11}$$

Finally, inserting Eqs. Eqs. (B.10) and (B.11) into Eq. (B.5), we find

$$J_1(t_1, t_2) = J_{\textit{Hard-Free}}(t) + \frac{|J_{\textit{Free-NC}}(t_1) + J_{\textit{Hard-NC}}(t_2)| - |J_{\textit{Free-NC}}(t_1) - J_{\textit{Hard-NC}}(t_2)|}{2} \tag{B.12}$$

Where t_1 is the spacer thickness between the free layer and NC, t_2 is the spacer thickness between the Hard layer and NC and t is the total thickness ($t = t_1 + t_2$).

Bibliography

[1] J. Slonczewski, Journal of applied physics **73**, 5957 (1993).

[2] F. Walz, J. Phys.: Condens. Matter **14**, R285 (2002).

[3] M. Stiles, J. Magn. Magn. Mater. **200**, 322 (1999).

[4] M. A. Ruderman and C. Kittel, Phys. Rev. **96**, 99 (1954).

[5] T. Kasuya, Prog. Theor. Phys. **16**, 4558 (1956).

[6] K. Yosida, Phys. Rev. **106**, 893 (1957).

[7] P. Grünberg, R. Schreiber, Y. Pang, M. B. Brodsky, and H. Sowers, Phys. Rev. Lett. **57**, 2442 (1986).

[8] C. F. Majkrzak, J. W. Cable, J. Kwo, M. Hong, D. B. McWhan, Y. Yafet, J. V. Waszczak, and C. Vettier, Phys. Rev. Lett. **56**, 2700 (1986).

[9] M. B. Salamon, S. Sinha, J. J. Rhyne, J. E. Cunningham, R. W. Erwin, J. Borchers, and C. P. Flynn, Phys. Rev. Lett. **56**, 259 (1986).

[10] M. N. Baibich, J. M. Broto, A. Fert, F. N. Van Dau, F. Petroff, P. Etienne, G. Creuzet, A. Friederich, and J. Chazelas, Phys. Rev. Lett. **61**, 2472 (1988).

[11] G. Binasch, P. Grünberg, F. Saurenbach, and W. Zinn, Phys. Rev. B **39**, 4828 (1989).

[12] A. Fert, P. Grünberg, A. Barthelemy, F. Petroff, and W. Zinn, J. Magn. Magn. Mater. **140**, 1 (1995).

[13] S. S. P. Parkin, N. More, and K. P. Roche, Phys. Rev. Lett. **64**, 2304 (1990).

[14] B. A. Jones, IBM Journal of Research and Development **42**, 25 (1998).

[15] B Heinrich, Springer Tracts in Modern Physics **227**, 185 (2007).

[16] H. Zabel, Superlattices and Microstructures **46**, 541 (2009).

[17] P. Bruno, Phys. Rev. B **49**, 13231 (1994).

[18] E. Fullerton, D. Margulies, M. Schabes, M. Carey, B. Gurney, A. Moser, M. Best, G. Zeltzer, K. Rubin, H. Rosen, et al., Applied Physics Letters **77**, 3806 (2000).

[19] J. Slonczewski, J. Magn. Magn. Mater. **150**, 13 (1995).

[20] S. Demokritov, Journal of Physics D: Applied Physics **31**, 925 (1998).

[21] D. Pierce, J. Unguris, R. Celotta, and M. Stiles, J. Magn. Magn. Mater. **200**, 290 (1999).

[22] J. C. Slonczewski, Phys. Rev. Lett. **67**, 3172 (1991).

[23] C. Marrows and B. Hickey, Physical Review B **59**, 463 (1999).

[24] Y. F. Chiang, J. J. I. Wong, X. Tan, Y. Li, K. Pi, W. H. Wang, H. W. K. Tom, and R. K. Kawakami, Phys. Rev. B **79**, 184410.

[25] I. Dzyaloshinskii, Sov. Phys. JETP **10**, 628 (1960).

[26] D. N. Astrov, Sov. Phys. JETP **11**, 708 (1960).

[27] M. Fiebig, J. Phys. D: Appl. Phys. **38**, R123 (2005).

[28] T. Maruyama, Y. Shiota, T. Nozaki, K. Ohta, N. Toda, M. Mizuguchi, A. Tulapurkar, T. Shinjo, M. Shiraishi, S. Mizukami, et al., Nature Nanotechnology **4**, 158 (2009).

[29] M. Weisheit, S. FŁhler, A. Marty, Y. Souche, C. Poinsignon, and D. Givord, Science **315**, 349 (2007).

[30] P. Borisov, A. Hochstrat, X. Chen, W. Kleemann, and C. Binek, Phys. Rev. Lett. **94**, 117203 (2005).

[31] X. Chen, A. Hochstrat, P. Borisov, and W. Kleemann, Applied physics letters **89**, 202508 (2006).

[32] X. He, Y. Wang, N. Wu, A. N. Caruso, E. Vescovo, K. D. Belashchenko, P. A. Dowben, and C. Binek, Nature Mater **9**, 579 (2010).

[33] Y. Chu, L. Martin, M. Holcomb, M. Gajek, S. Han, Q. He, N. Balke, C. Yang, D. Lee, W. Hu, et al., Nature materials **7**, 478 (2008).

[34] W. Eerenstein, N. Mathur, and J. Scott, Nature **442**, 759 (2006).

[35] V. Novosad, Y. Otani, A. Ohsawa, S. Kim, K. Fukamichi, J. Koike, K. Maruyama, O. Kitakami, and Y. Shimada, Journal of Applied Physics **87**, 6400 (2000).

[36] D. Chiba, M. Yamanouchi, F. Matsukura, and H. Ohno, Science **301**, 943 (2003).

[37] I. Stolichnov, S. Riester, H. Trodahl, N. Setter, A. Rushforth, K. Edmonds, R. Campion, C. Foxon, B. Gallagher, and T. Jungwirth, Nature materials **7**, 464 (2008).

[38] C.-G. Duan, S. S. Jaswal, and E. Y. Tsymbal, Phys. Rev. Lett. **97**, 047201 (2006).

[39] J. Rondinelli, M. Stengel, and N. Spaldin, Nature nanotechnology **3**, 46 (2007).

[40] A. Ichimiya and P. Cohen, *Reflection high-energy electron diffraction* (Cambridge University Press, 2004).

[41] J. Klein, "Epitaktische Heterostrukturen aus dotierten Manganaten", PhD thesis (Universität zu Köln, 2001).

[42] W. H. Butler, X.-G. Zhang, T. C. Schulthess, and J. M. MacLaren, Phys. Rev. B **63**, 054416 (2001).

[43] S. Parkin, C. Kaiser, A. Panchula, P. Rice, B. Hughes, M. Samant, and S. Yang, Nature materials **3**, 862 (2004).

[44] S. Yuasa, T. Nagahama, A. Fukushima, Y. Suzuki, and K. Ando, Nature materials **3**, 868 (2004).

[45] S. Yuasa, A. Fukushima, H. Kubota, Y. Suzuki, and K. Ando, Applied Physics Letters **89**, 042505 (2006).

[46] X.-G. Zhang and W. H. Butler, Phys. Rev. B **70**, 172407 (2004).

[47] H. L. Meyerheim, R. Popescu, N. Jedrecy, M. Vedpathak, M. Sauvage-Simkin, R. Pinchaux, B. Heinrich, and J. Kirschner, Phys. Rev. B **65**, 144433 (2002).

[48] X.-G. Zhang, W. H. Butler, and A. Bandyopadhyay, Phys. Rev. B **68**, 092402 (2003).

[49] C. Tusche, H. L. Meyerheim, N. Jedrecy, G. Renaud, A. Ernst, J. Henk, P. Bruno, and J. Kirschner, Phys. Rev. Lett. **95**, 176101 (2005).

[50] M. Y. Zhuravlev, E. Y. Tsymbal, and A. V. Vedyayev, Phys. Rev. Lett. **94**, 026806 (2005).

[51] B. D. Yu and J.-S. Kim, Phys. Rev. B **73**, 125408 (2006).

[52] P. G. Mather, J. C. Read, and R. A. Buhrman, Phys. Rev. B **73**, 205412 (2006).

[53] J. Velev, K. Belashchenko, S. Jaswal, and E. Tsymbal, Applied physics letters **90**, 072502 (2007).

[54] C. Tusche, H. L. Meyerheim, N. Jedrecy, G. Renaud, and J. Kirschner, Phys. Rev. B **74**, 195422 (2006).

[55] J. Faure-Vincent, C. Tiusan, C. Bellouard, E. Popova, M. Hehn, F. Montaigne, and A. Schuhl, Phys. Rev. Lett. **89**, 107206 (2002).

[56] T. Katayama, S. Yuasa, J. Velev, M. Zhuravlev, S. Jaswal, and E. Tsymbal, Evgeny Tsymbal Publications, 3 (2006).

[57] J. C. Slonczewski, Phys. Rev. B **39**, 6995 (1989).

[58] E. Snoeck, P. Baules, G. BenAssayag, C. Tiusan, F. Greullet, M. Hehn, and A. Schuhl, Journal of Physics: Condensed Matter **20**, 055219 (2008).

[59] B. Heinrich, Z. Celinski, J. F. Cochran, A. S. Arrott, K. Myrtle, and S. T. Purcell, Phys. Rev. B **47**, 5077 (1993).

[60] C. Tiusan, M. Sicot, J. Faure-Vincent, M. Hehn, C. Bellouard, F. Montaigne, S. Andrieu, and A. Schuhl, Journal of Physics: Condensed Matter **18**, 941 (2006).

[61] Y. Lu, C. Deranlot, A. Vaurès, F. Petroff, J. George, Y. Zheng, and D. Demailles, Applied Physics Letters **91**, 222504 (2007).

[62] W. Weber, C. H. Back, A. Bischof, C. Würsch, and R. Allenspach, Phys. Rev. Lett. **76**, 1940 (1996).

[63] C. Bellouard, J. Faure-Vincent, C. Tiusan, F. Montaigne, M. Hehn, V. Leiner, H. Fritzsche, and M. Gierlings, Phys. Rev. B **78**, 134429 (2008).

[64] W. Folkerts and S. Purcell, J. Magn. Magn. Mater. **111**, 306 (1992).

[65] J. Cochran, J. Magn. Magn. Mater. **147**, 101 (1995).

[66] S. Demokritov, E. Tsymbal, P. Grünberg, W. Zinn, and I. K. Schuller, Phys. Rev. B **49**, 720 (1994).

[67] A. Milner, A. Gerber, B. Groisman, M. Karpovsky, and A. Gladkikh, Phys. Rev. Lett. **76**, 475 (1996).

[68] A. Tomou, L. Panagiotopoulos, D. Gournis, and B. Kooi, J. Appl. Phys. **102**, 023910 (2007).

[69] S. Mitani, S. Takahashi, K. Takanashi, K. Yakushiji, S. Maekawa, and H. Fujimori, Phys. Rev. Lett. **81**, 2799 (1998).

[70] C Binns, M. J. Maher, Q. A. Pankhurst, D. Kechrakos, and K. N. Trohidou, Phys. Rev. B **66**, 184413 (2002).

[71] Z. Mao, Z. He, D. Chen, W. Y. Cheung, and S. P. Wong, Solid State Communications **142**, 329 (2007).

[72] S. Takahashi and S. Maekawa, Phys. Rev. Lett. **80**, 1758 (1998).

[73] H. Yang, S.-H. Yang, and S. S. P. Parkin, Nano Lett. **8**, 340 (2008).

[74] Y. Wang, X. F. Han, and X.-G. Zhang, Appl. Phys. Lett. **93**, 172501 (2008).

[75] H. Sukegawa, S. Nakamura, A. Hirohata, N. Tezuka, and K. Inomata, Phys. Rev. Lett. **94**, 068304 (2005).

[76] E Popova, N Keller, F Gendron, C Tiusan, A Schuhl, and N. A. Lesnik, Appl. Phys. Lett. **91**, 112504 (2007).

[77] H.-C. Wu, S. K. Arora, O. N. Mryasov, and I. V. Shvets, Appl. Phys. Lett. **92**, 182502 (2008).

[78] M. Y. Zhuravlev, J. Velev, A. V. Vedyayev, and E. Y. Tsymbal, J. Magn. Magn. Mater. **300**, e277 (2006).

[79] H. Li and B. P. Tonner, Phys. Rev. B **40**, 10241 (1989).

[80] S. Yuasa, T. Katayama, T. Nagahama, A. Fukushima, H. Kubota, Y. Suzuki, and K. Ando, Appl. Phys. Lett. **87**, 222508 (2005).

[81] M. Klaua, D. Ullmann, J. Barthel, W. Wulfhekel, J. Krischner, R. Urban, T. L. Monchesky, A Enders, J. F. Cochran, and B. Heinrich, Phys. Rev. B **64**, 134411 (2001).

[82] W. Wulfhekel, M. Klaua, D. Ullmann, F. Zavaliche, J. Krischner, R. Urban, T. L. Monchesky, and B. Heinrich, Appl. Phys. Lett. **78**, 509 (2001).

[83] G. Fahsold, A Pucci, and K.-H. Rieder, Phys. Rev. B **61**, 8475 (2000).

[84] R. K. Kawakami, E. Rotenberg, H. J. Choi, E. J. Escorcia-Aparicio, M. O. Bowen, J. H. Wolfe, E. Arenholz, Z. D. Zhang, N. V. Smith, and Z. Q. Qiu, Nature **398**, 132 (1999).

[85] R. K. Kawakami, E. Rotenberg, E. J. Escorcia-Aparicio, H. J. Choi, T. R. Cummins, J. G. Tobin, N. V. Smith, and Z. Q. Qiu, Phys. Rev. Lett. **80**, 1754 (1998).

[86] T. S. Santos, J. S. Moodera, K. V. Raman, E. Negusse, J. Holroyd, J. Dvorak, M. Liberati, Y. U. Idzerda, and E. Arenholz, Phys. Rev. Lett. **101**, 147201 (2008).

[87] H. Haugen, D. Huertas-Hernando, and A. Brataas, Phys. Rev. B **77**, 115406 (2008).

[88] A. G. Swartz, J. Ciraldo, J. J. I. Wong, Y. Li, W. Han, T. Lin, S. Mack, J. Shi, D. D. Awschalom, and R. K. Kawakami, Appl. Phys. Lett. **97**, 112509 (2010).

[89] K. Y. Ahn and M. W. Shafer, J. Appl. Phys. **41**, 1260 (1970).

[90] S. A. Wolf, D. D. Awschalom, R. A. Buhrman, J. M. Daughton, S. von Molnar, M. L. Roukes, A. Y. Chtchelkanova, and D. M. Treger, Science **294**, 1488 (2001).

[91] M. R. Oliver, J. O. Dimmock, A. L. McWhorter, and T. B. Reed, Phys. Rev. B **5**, 1078 (1972).

[92] Y. Shapira, S. Foner, and T. B. Reed, Phys. Rev. B **8**, 2299 (1973).

[93] A. Schmehl, V. Vaithyanathan, A. Herrnberger, S. Thiel, C. Richter, M. Liberati, T. Heeg, M. Rockerath, L. F. Kourkoutis, S. Muhlbauer, P. Boni, D. A. Muller, Y. Barash, J. Schubert, Y. Idzerda, J. Mannhart, and D. G. Schlom, Nature Materials **6**, 882 (2007).

[94] T. Yamasaki, K. Ueno, A. Tsukazaki, T. Fukumura, and M. Kawasaki, Appl. Phys. Lett. **98**, 082116 (2011).

[95] H. Ott, S. J. Heise, R. Sutarto, Z. Hu, C. F. Chang, H. H. Hsieh, H.-J. Lin, C. T. Chen, and L. H. Tjeng, Phys. Rev. B **73**, 094407 (2006).

[96] R. W. Ulbricht, A. Schmehl, T. Heeg, J. Schubert, and D. G. Schlom, Appl. Phys. Lett. **93**, 102105 (2008).

[97] R. Sutarto, S. G. Altendorf, B. Coloru, M. Moretti Sala, T. Haupricht, C. F. Chang, Z. Hu, C. Schüßler-Langeheine, N. Hollmann, H. Kierspel, H. H. Hsieh, H.-J. Lin, C. T. Chen, and L. H. Tjeng, Phys. Rev. B **79**, 205318 (2009).

[98] X. Jiang, R. Wang, R. M. Shelby, R. M. Macfarlane, S. R. Bank, J. S. Harris, and S. S. P. Parkin, Phys. Rev. Lett. **94**, 056601 (2005).

[99] T. Sasaki, T. Oikawa, T. Suzuki, M. Shiraishi, Y. Suzuki, and K. Tagami, Appl. Phys. Express **2**, 053003 (2009).

[100] Y. Zhou, W. Han, L.-T. Chang, F. Xiu, M. Wang, M. Oehme, I. A. Fischer, J. Schulze, R. K. Kawakami, and K. L. Wang, Phys. Rev. B **84**, 125323 (2011).

[101] W. Han, K. Pi, K. M. McCreary, Y. Li, J. J. I. Wong, A. G. Swartz, and R. K. Kawakami, Phys. Rev. Lett. **105**, 167202 (2010).

[102] R. A. McKee, F. J. Walker, E. D. Specht, G. E. Jellisen, and L. A. Boatner, Phys. Rev. Lett. **72**, 2741 (1994).

[103] D. M. Lind, S. D. Berry, G. Chern, H. Mathias, and L. R. Testardi, Phys. Rev. B **45**, 1838 (1992).

[104] N. Iwata, G. Pindoria, T. Morishita, and K. Kohn, J. Phys. Soc. Jpn. **69**, 230 (2000).

[105] D. F. Forster, J. Klinkhammer, C. Busse, S. G. Altendorf, T. Michely, Z. Hu, Y. Y. Chin, L. H. Tjeng, J. Coraux, and D. Bourgault, Phys. Rev. B **83**, 045424 (2011).

[106] J. J. I. Wong, L. Ramirez, A. G. Swartz, A. Hoff, W. Han, Y. Li, and R. K. Kawakami, Phys. Rev. B **81**, 094406 (2010).

[107] K. Momma and F. Izumi, J. Appl. Crystallogr. **41**, 653 (2008).

[108] R. D. Shannon, Acta Crystallogr., Sect. A: Cryst. Phys. Diff., Theor. Gen. Crystallogr. **32**, 751 (1976).

[109] H. Kawanowa, D. Mori, Y. Gotohand, and R. Souda, Surf. Interface Anal. **36**, 1001 (2004).

[110] R. Rausch and W. Nolting, J. Phys.: Condens. Matter **21**, 376002 (2009).

[111] Z. Q. Qiu, J. Pearson, and S. D. Bader, Phys. Rev. Lett. **70**, 1006 (1993).

[112] M. Stampanoni, A. Vaterlaus, M. Aeschlimann, and F. Meier, Phys. Rev. Lett. **59**, 2483 (1987).

[113] B. Heinrich, K. B. Urquhart, A. S. Arrott, J. F. Cochran, K. Myrtle, and S. T. Purcell, Phys. Rev. Lett. **59**, 1756 (1987).

[114] N. C. Koon, B. T. Jonker, F. A. Volkening, J. J. Krebs, and G. A. Prinz, Phys. Rev. Lett. **59**, 2463 (1987).

[115] K. Momma and F. Izumi, Journal of Applied Crystallography **44**, 1272 (2011).

[116] M. Fonin, R. Pentcheva, Y. Dedkov, M. Sperlich, D. Vyalikh, M. Scheffler, U. Rüdiger, and G. Güntherodt, Physical Review B **72**, 104436 (2005).

[117] J. Sthr and H. C. Siegmann, *Magnetism*, Vol. 152 (Wiley New York, 2006).

[118] J. Wong, A. Swartz, R. Zheng, W. Han, and R. Kawakami, Physical Review B **86**, 060409 (2012).

[119] Y. Ding, D. Haskel, S. G. Ovchinnikov, Y.-C. Tseng, Y. S. Orlov, J. C. Lang, and H.-k. Mao, Phys. Rev. Lett. **100**, 045508 (2008).

[120] J. Garcia, G. Subias, J. Herrero-Martin, J. Blasco, V. Cuartero, M. C. Sanchez, C. Mazzoli, and F. Yakhou, Phys. Rev. Lett. **102**, 176405 (2009).

[121] D. J. Huang, H. J. Lin, J. Okamoto, K. S. Chao, H. T. Jeng, G. Y. Guo, C. H. Hsu, C. M. Huang, D. C. Ling, W. B. Wu, C. S. Yang, and C. T. Chen, Phys. Rev. Lett. **96**, 096401 (2006).

[122] J. E. Lorenzo, C. Mazzoli, N. Jaouen, C. Detlefs, D. Mannix, S. Grenier, Y. Joly, and C. Marin, Phys. Rev. Lett. **101**, 226401 (2008).

[123] G. K. Rozenberg, M. P. Pasternak, W. M. Xu, Y. Amiel, M. Hanfland, M. Amboage, R. D. Taylor, and R. Jeanloz, Phys. Rev. Lett. **96**, 045705 (2006).

[124] M. S. Senn, J. P. Wright, and J. P. Attfield, Nature **481**, 173 (2011).

[125] F. Zhou and C. Gerbrand, Phys. Rev. B **81**, 205113 (2010).

[126] E. J. W. Verwey, Nature **144**, 327 (1939).

[127] E. J. W. Verwey and P. W. Haayman, Physica **8**, 979987 (1941).

[128] V. A. M. Brabers, F. Walz, and H. Kronmuller, Phys. Rev. B **58**, 14163 (1998).

[129] C. H. Ahn, J. M. Triscone, and J. Mannhart, Nature **424**, 1015 (2003).

[130] A. Asamitsu, Y. Tomioka, H. Kuwahara, and Y. Tokura, Nature **388**, 50 (1997).

[131] S. Lee, A. Fursina, J. T. Mayo, C. T. Yavuz, V. L. Colvin, R. G. S. Sofin, I. V. Shvets, and D. Natelson, Nature Mater. **7**, 130 (2008).

[132] T. Lottermoser, T. Lonkai, U. Amann, D. Hohlwein, J. Ihringer, and M. Fiebig, Nature **430**, 541 (2004).

[133] H. Zheng, J. Wang, S. E. Lofland, Z. Ma, L. Mohaddes-Ardabili, T. Zhao, L. Salamanca-Riba, S. R. Shinde, S. B. Ogale, F. Bai, D. Viehland, Y. Jia, D. G. Schlom, M. Wuttig, A. Roytburd, and R Ramesh, Science **303**, 661 (2004).

[134] M. Alexe, M. Ziese, D. Hesse, P. Esquinazi, K. Yamauchi, T. Fukushima, S. Picozzi, and U. Gosele, Adv. Mater. **21**, 4452 (2009).

[135] J. van den Brink and D. I. Khomskii, J. Phys.: Condens. Matter **20**, 434217 (2008).

[136] G. T. Rado and J. M. Ferrari, Phys. Rev. B **15**, 290 (1977).

[137] K. Kato, S. Iida, K. Yanai, and K. Mizushima, J. Magn. Magn. Mater. **31-34**, 783 (1983).

[138] Y. Miyamoto, S. Ishihara, T. Hirano, M. Takada, and N. Suzuki, Solid State Comm. **89**, 51 (1994).

[139] Z. Zhang and S. Satpathy, Phys. Rev. B **44**, 13319 (1991).

[140] P. Seneor, A. Fert, J. L. Maurice, F. Montaigne, F. Petro, and A. Vaures, Appl. Phys. Lett. **74**, 4017 (1999).

[141] Y. Li, W. Han, A. G. Swartz, K. Pi, J. J. I. Wong, S. Mack, D. D. Awschalom, and R. K. Kawakami, Phys. Rev. Lett. **105**, 167203 (2010).

[142] W. Eerenstein, T. T. M. Palstra, T. Hibma, and S. Celotto, Phys. Rev. B. **66**, 201101(R) (2002).

[143] F. Wang, C.-H. Li, T. Zou, L. Yi, and Y. Sun, J. Phys.: Condens. Matter **22**, 496001 (2010).

[144] C. A. F. Vaz, J. Hoffman, Y. Segal, J. W. Reiner, R. D. Grober, Z. Zhang, C. H. Ahn, and F. J. Walker, Phys. Rev. Lett. **104**, 127202 (2010).

[145] J. Ryu, A. V. Carazo, K. Uchino, and H.-E. Kim, Jpn. J. Appl. Phys. **40**, 4948 (2001).

[146] J. Ryu, S. Priya, K. Uchino, and H.-E. Kim, J. Electroceram. **8**, 107 (2002).

[147] L. Yan, Z. Wang, Z. Xing, and J. Li, J. Appl. Phys. **107**, 064106 (2010).

[148] A. Pimenov, S. Tachos, T. Rudolf, A. Loidl, D. Schrupp, M. Sing, R. Claessen, and V. A. M. Brabers, Phys. Rev. B **72**, 035131 (2005).

[149] Y. Nagasawa, M. Kosaka, S. Katano, N. Mori, S. Tado, and Y. Uwatoko, J. Phys. Soc. Jpn. **76**, 110 (2007).

[150] S. Suryanarayana, Bull. Mater. Sci. **17**, 1259 (1994).

[151] N. Hur, S. Park, P. A. Sharma, J. S. Ahn, S. Guha, and S.-W. Cheong, Nature **429**, P392 (2004).

[152] A. Swartz, J. Wong, I. Pinchuk, and R. Kawakami, Journal of Applied Physics **111**, 083912 (2012).

[153] S. Blundell and D. Thouless, *Magnetism in condensed matter*, Vol. 13 (Oxford University Press New York, 2001).

[154] W. Callister and D. Rethwisch, *Materials science and engineering: an introduction*, Vol. 7 (Wiley New York, 2007).